EFFECTS OF BRONSTED AND LEWIS BASES ON FORMIC ACID DEHYDROGENATION SELECTIVITY OF Pd(111) SINGLE CRYSTAL MODEL CATALYST

A THESIS SUBMITTED TO THE GRADUATE SCHOOL OF ENGINEERING AND SCIENCE OF BILKENT UNIVERSITY IN PARTIAL FULFILLMENT OF THE REQUIREMENTS FOR THE DEGREE OF MASTER OF SCIENCE IN CHEMISTRY

By

Bartu Karakurt

June 2020

EFFECTS OF BRØNSTED AND LEWIS BASES ON FORMIC ACID DEHYDROGENATION SELECTIVITY OF Pd(111) SINGLE CRYSTAL MODEL CATALYST

By Bartu Karakurt

June 2020

We have certified that we have read this dissertation and that in our opinion it is fully adequate, in scope and quality, as a dissertation for the degree of Master of Science.

Emrah Özensoy (Advisor)

Şefik Süzer

Mehmet Fatih Danışman

Approved for the Graduate School of Engineering and Science:

Ezhan Karasan

Director of the Graduate School

ABSTRACT

EFFECTS OF BRONSTED AND LEWIS BASES ON FORMIC ACID DEHYDROGENATION SELECTIVITY OF Pd(111) SINGLE CRYSTAL MODEL CATALYST

By Bartu Karakurt

M.Sc. in Chemistry

Advisor: Emrah Özensoy

June 2020

Formic acid (FA) is an environmentally friendly hydrogen-based energy vector that can be obtained from renewable biomass feedstocks. However, catalytic decomposition of FA involves two different competing chemical pathways called dehydration and dehydrogenation. Thus, molecular level studies focusing on the selective catalytic FA dehydrogenation are essential for establishing structure-reactivity relationships which can be used in order to increase the catalytic dehydrogenation selectivity. In the current work, effects of Bronsted and Lewis bases on catalytic FA dehydrogenation selectivity were studied under ultra-high vacuum (UHV) conditions on an atomically well-defined Pd(111) single crystal model catalyst surface by using temperature programmed desorption/temperature programmed reaction spectroscopy (TPD/TPRS), X-Ray photoelectron spectroscopy (XPS) and low energy electron diffraction (LEED) techniques. Doubly-deuterated FA (DCOOD) was used as the FA source, while ammonia and manganese oxide were chosen as the model Bronsted and Lewis bases. Adsorption and subsequent surface decomposition reaction of DCOOD on Pd(111) showed that model catalyst was not totally selective towards dehydrogenation. Functionalizing the Pd(111) surface with ammonia suppressed the FA dehydration and boosted the

dehydrogenation pathway, where positive influence of ammonia on FA dehydrogenation selectivity decayed when ammonia coverage was greater than 1 ML. A boost in hydrogen generation was observed in the catalytic FA dehydrogenation on manganese oxide-deposited Pd(111) surface (at sub-monolayer manganese oxide regime) as compared to that of a clean Pd(111) model catalyst. It was found out that manganese oxide can enhance FA dehydrogenation by acting as a promoter and/or catalytically contributing to the reaction depending on the oxidation state composition.

Keywords: Bronsted base, Lewis base, Formic acid, Dehydrogenation, Pd(111), Model Catalyst

ÖZET

BRONSTED VE LEWIS BAZLARININ Pd(111) TEK KRİSTAL MODEL KATALİZÖRÜNÜN FORMİK ASİT DEHİDREJENASYON SEÇİCİLİĞİNE OLAN ETKİLERİ

Bartu Karakurt

Kimya, Yüksek Lisans

Tez Danışmanı: Emrah Özensoy

Haziran 2020

Formik asit (FA) yenilenebilir biyokütle atıklarından elde edilebilen, çevre dostu bir hidrojen kaynağıdır. FA her ne kadar ümit verici bir alternatif hidrojen kaynağı olsa da; bu molekülün yan reaksiyonlar vermeye yatkın olması formik asitten yüksek verimlilikle hidrojen üretilebilmesi için dehidrejenasyon katalizörleri kullanmayı zorunlu bir hale getirmektedir. Bu bağlamda, katalitik FA parçalanması üzerine yoğunlaşan moleküler düzeydeki çalışmalar kimyasal yapı-reaktivite ilişkilerinin irdelenmesi ve buna paralel olarak, katalizörlerin FA dehidrejenasyon seçiciliklerinin arttırılması adına büyük önem taşımaktadır. Bu çalışmada, Bronsted ve Lewis bazlarının Pd(111) tek kristal model katalizörünün FA dehidrejenasyon seçiciliğine olan etkileri, sıcaklık programlı desorption/sıcaklık programlı reaksiyon spektroskopisi (TPD/TPRS), X-ışını fotoelektron spectroskopisi (XPS) ve düşük enerjili elektron kırınımı (LEED) teknikleri kullanılarak ultra-yüksek vakum (UHV) koşulları altında incelenmiştir. Çalışmalar sırasında, FA kaynağı olarak, her iki hidrojeni de izotopik olarak etiketlenmiş FA (DCOOD) kullanılırken; amonyak ve mangan oksit sırasıyla model Bronsted ve Lewis bazları olarak kullanılmıştır. DCOOD'nin Pd(111) yüzeyine adsorpsiyonu ve takiben yüzeyde verdiği dehidrasyon ve dehidrejenasyon reaksiyonları sonucunda katalizörün FA

dehidrejenasyon seçiciliğinin %100 olmadığı saptanmıştır. Pd(111) yüzeyinin amonyakla işlevselleştirilmesi sonucunda; FA dehidrejenasyon seçiciliğinin arttırdığı ve dehidrasyon reaksiyonunun baskılandığı gözlemlenmiş ve amonyağın dehidrejenasyon seçiciliği üzerindeki pozitif etkisinin yüzeyde 1 ML'den (ML, tek katman) daha fazla amonyak bulunması durumunda azaldığı görülmüştür. Benzer bir şekilde; Pd(111) yüzeyinin 0.25 ML mertebesinde mangan oksitle kaplanması sonucunda, hidrojen üretiminin, temiz Pd(111) yüzeyine kıyasla, önemli şekilde arttığı görülmüştür. Bulgularımız, mangan oksitin oksidasyon duruma bağlı olarak, hidrojen üretimini hem FA'ın katalizör yüzeyiyle daha güçlü etkileşmesini sağlayarak (FA'ın yüzey adsorpsiyonunu ve yüzey yayılımını arttırarak), hem de katalitik olarak arttırabildiğini ortaya koymuştur.

Anahtar Sözcükler: Bronsted bazı, Lewis bazı, Formik asit, Dehidrejenasyon, Pd(111), Model Katalizör

Acknowledgements

Foremost, I would like thank my advisor Dr. Emrah Özensoy for patiently believing in me and guiding me starting from my Freshman years. His vision and immense knowledge taught me the invaluable essence of how to think, evaluate and act like a scientist. He is, and will be, undoubtably the most influential person in my academic career and I will be always grateful to him for giving me a chance to work in my favorite research field.

Besides my advisor, I would like to thank rest of my thesis committee, Prof. Şefik Süzer and Assoc. Prof. Mehmet Fatih Danışman for their invaluable comments and time.

I would like to thank Dr. Yusuf Koçak for standing out for me as a big brother and sharing his vast research and life experience with me during the most challenging times. I will be always grateful for him for the unlimited support and patience that he showed me during my most vulnerable times. I would like to also thank my former lab mate Dr. Mustafa Karatok for always sparing time for me and genuinely supporting me whenever I needed, Ali Vâlâ Koç for trying his best to share his research experience with me despite the hardships that he dealt with and Dr. Igor Lyubinetsky for giving me a chance to work with him and learn from his immense knowledge and research experience.

I would like to thank all of my group members, especially Gökberk Katırcı for his sincere friendship and being there for me to help in any way possible. I would like to also thank Kerem Emre Ercan for initially inspiring me to become a good scientist as a great TA and then leading me at various beamtime shifts as an exceptional colleague.

I would like to thank Mahircan Ganioğlu for teaching me the meaning of true friendship and being the best friend that I have ever had. Without him, I would not be who I am today.

My warmest gratitude goes to the people that I have learned from the most. I would like to thank Xieraili Alimujiang for teaching me the core of mental/physical strength and for all the fun that we had during our billiards matches. Especially, I would like to thank Reyihanguli Alimujiang from the bottom of my heart for teaching me how to love myself, how to love others and live as a courageous and independent man.

Finally, my most sincere gratitude goes to my parents, who are the two most important people in my life. I would like to thank them for all the effort that they showed in order to raise me and for their unconditional love.

Table of Contents

1. Introduction 1

1.1 Future and Sustainability of the Global Energy Demand and Environment 1

1.2 Hydrogen as an Alternative Fuel Source 1

1.3 Formic Acid as a Potential Hydrogen Source 2

1.4 A Literature Review on Formic Acid Dehydrogenation Catalysts 3

1.5 Key Aspect of Formic Acid Decomposition on Heterogeneous catalysts 4

1.5.1 Effects of Coordination Number of Catalyst Surface and Adsorption Geometry of Formic Acid on Dehydrogenation Selectivity 4

1.5.2 Relationship Between Catalyst Life Span and Dehydrogenation Selectivity 7

1.6 Effects of Brønsted and Lewis Bases on Formic Acid dehydrogenation selectivity of Heterogenous Catalysts 7

1.7 Motivation of the Current Study 9

2. Experimental 12

2.1 Experimental Setup 12

2.2 Surface Characterization Techniques Utilized in This Study 13

2.3 Low Energy Electron Diffraction (LEED) 14

2.4 X-Ray Photoelectron Spectroscopy (XPS) 17

2.5 Temperature Programmed Desorption/Reaction Spectroscopy (TPD/TPRS) 19

2.6 Experimental Procedures 24

2.6.1 Cleaning of Pd(111) Single Crystal Model Catalyst 24

2.6.2 Doubly-Deuterated Formic Acid Residual Gas analysis (RGA) 25

2.6.3 Protecting Deuterium Labelling of Doubly-Deuterated Formic Acid 26

2.6.4 Characterization of Pd(111) Single Crystal Model Catalyst 27

2.6.5 Deposition of Manganese (Mn) on Pd(111) 28

3. Effects of Brønsted Bases on Formic Acid Dehydrogenation Selectivity of Pd(111) Single Crystal Model Catalyst 31

3.1 Ammonia (NH_3) Adsorption on Pd(111) 32

3.2 DCOOD Adsorption on Pd(111) 35

3.3 DCOOD Adsorption on NH_3 functionalized Pd(111) 39
3.3.1 Behaviour of NH_3 in the presence of DCOOD 39
3.3.2 Effects of NH_3 on Water (D_2O, DHO and H_2O) Production 42
3.3.3 Effects of NH_3 on CO_2 Production 43
3.3.4 Effects of NH_3 on D_2 Production 47
3.3.5 Effects of NH_3 on DH and H_2 Production 51
3.3.6 Effects of NH_3 on CO Production 51

4. Effects of MnO_x Model Lewis Base on Formic Acid Dehydrogenation Selectivity of Pd(111) Single Crystal Model Catalyst 55

4.1 Determination of Mn Coverage on Pd(111) Surface 56
4.2 Adsorption of DCOOD on Pd(111) 56
4.3 Effects of MnO_x on D_2 formation 58
4.4 Effects of MnO_x deposition on Formic Acid Decomposition 66
4.5 Effects of MnO_x Coverage on D_2 formation 68

5. Conclusion 71

A. Alternative Interpretation of Mn $2p_{3/2}$ XPS spectra given in Figures 4.5 and 4.9 82
B. Difference (Δ) XPS spectra of Mn $2p_{3/2}$ XPS spectra represented in Figures 4.5 and 4.9 84
C. List of Publications 85

List of Figures

1.1 Possible absorption geometries formed by carboxylic acids on transition metal surfaces. Adapted from Ref. [54] 5
1.2 Various oligomers/polymers generated upon formic acid adsorption on Ag(111) single crystal surface. Adapted from Ref. [43] 6

1.3 Different adsorption geometries of CO on Pd(111) surface. Adapted from Ref. [59] 7

1.4 Schematic representation of formic acid adsorption on MnO_x surface 9

1.5 TEM image of Rh/CeO_2. Adapted from Ref. [68] 10

2.1 Photographs of the experimental setup 13

2.2 Plot of electron inelastic mean free path (IMFP) values of various materials as a function of electron kinetic energy. (The "universal curve") Adapted from Ref. [70] 14

2.3 Schematic representation of a LEED experiment. (a_1,a_2) are unit cell vectors and (a_1^*,a_2^*) are the corresponding momentum space vectors. Adapted from Ref. [71] 15

2.4 (a) Sample LEED diffraction pattern obtained on a phosphorescence screen. (b) Schematic of a LEED setup. Adapted from Ref. [72] 16

2.5 (a) Schematic of the dual anode X-Ray source used in this work. Adapted from Ref [74]. (b) Schematic of the double-pass cylindrical mirror energy analyzer used in this work. Adapted from Ref [75]. (c) Schematic of a hemispherical energy analyzer Adapted from Ref [76] 18

2.6 Sample TPD spectra obtained for (a) zeroth order (b) first order (c) second order desorption kinetics as a function of increasing adsorbate coverage. Adapted from Ref. [69] 21

2.7 Schematic of a TPD/TPRS module that is used for UHV surface science applications. Adapted from Ref. [70] 23

2.8 (a) XPS Survey Spectrum obtained from clean Pd(111). (b) *m/z* = 28 (CO) TPD profile obtained from blank TPD obtained from clean Pd(111) 25

2.9 (a) DCOOD RGA obtained at 298K and P_{DCOOD}= 5.5x10^{-8} Torr. (b) Background RGA spectrum of the UHV chamber obtained at 298K 26

2.10 (a) Pd*3d* XPS spectrum of clean Pd(111)..... 27

2.11 (a) LEED pattern of unclean Pd(111) surface (b) LEED pattern of clean Pd(111) surface..... 28

2.12 (a) Top-view of custom-made evaporators. It should be noted that different Mn-evaporators are labelled as 1, 2, and 3; (b) Side-view of the custom-made Mn evaporators. (c) Thin film doser compartment of the UHV setup..... 29

3.1 Schematic illustration of the enhancement in FA dehydrogenation over Pd(111) single crystal model catalyst surface upon NH_3 functionalization..... 31

3.2 *m/z* = 2 (H_2) and *m/z* = 28 (N_2) TPD profiles that were obtained after NH_3 adsorption on clean Pd(111) at 90 K as a function of increasing NH_3 coverage..... 32

3.3 TPD profiles (*m/z* = 17) obtained after adsorption of NH_3 at 90 K on clean Pd(111) as a function of increasing ammonia coverage 33

3.4 (a) TPD profiles of DCOOD adsorption on clean Pd (111) with a DCOOD exposure of $\varepsilon_{(DCOOD)} = 2\times10^{-2}$ L at 123 K. Note that some of the TPD signals are multiplied with the given factors for clarity. (b) *m/z* = 2 desorption channel from a blank (control) TPD experiment on a freshly cleaned Pd(111) surface in the absence of any intentionally added adsorbates 36

3.5 Schematic representation of formation and decarboxylation of bidentate formate species on Pd(111). Note that this illustration does not account for the actual stoichiometry of formate formation from FA 38

3.6 TPRS profiles for DCOOD adsorption ($\varepsilon_{(DCOOD)}$ = 2×10^{-2} L at 90 K) on Pd (111) which was initially exposed to (a) 0.1, (b) 0.4, (c) 0.8, (d), 1.0, (e) 1.4 MLE of NH_3 41

3.7 TPRS profiles for DCOOD ($\varepsilon_{(DCOOD)}$ = 2×10^{-2} L at 90 K) adsorption on Pd (111) which was initially exposed to various coverages of NH_3: *m/z* = (a) 20, (b) 19, (c) 18 desorption channels. (d) Corresponding integrated TPRS signal intensities for *m/z* = 20 (D_2O) channel 42

3.8 (a) TPRS profiles for CO_2 (*m/z* = 44) production upon DCOOD adsorption ($\varepsilon_{(DCOOD)}$ = 2×10^{-2} L at 90 K) on Pd (111) which was initially exposed to various coverages of NH_3. (b) Corresponding integrated TPRS signal intensities for *m/z* = 44 channel 44

3.9 Schematic representation of $[NH_4]^+$-$[HCOO]^-$ formation and decarboxylation on ammonium formate on NH_3 functionalized Pd(111) surface. Note that this illustration does not account for the actual reaction stoichiometry 45

3.10 TPRS profiles of *m/z* = 46 (DCOO/HCOOH) channel for DCOOD adsorption ($\varepsilon_{(DCOOD)}$ = 2×10^{-2} L at 90 K) on Pd(111) which was initially exposed to (green) 0.8, (navy) 1, and (pink) 1.4 MLE of NH_3. The orange curve represents the TPD profile obtained from the DCOOD adsorption ($\varepsilon_{(DCOOD)}$ = 2×10^{-2} L at 123 K) on clean Pd(111) 46

3.11 TPRS profiles for DCOOD adsorption ($\varepsilon_{(DCOOD)}$ = 2×10^{-2} L at 90 K) on Pd (111) which was initially exposed to various coverages of NH_3: *m/z* = (a) 4 (D_2), (b) 3 (DH), (c) 2 (H_2) desorption channels 48

3.12 Integrated *m/z* = (a) 4 (D_2), (b) 3 (DH), (c) 2 (H_2) TPRS desorption signals for DCOOD adsorption ($\varepsilon_{(DCOOD)}$ = 2×10^{-2} L at 90 K) on Pd (111) which was initially exposed to various coverages of NH_3 at 90 K 49

3.13 Schematic representation of FA dehydrogenation on NH_3 functionalized Pd(111) surface. Note that this reaction does not account for actual reaction stoichiometry 50

3.14 Integrated *m/z* = 28 (CO) TPRS desorption signals for DCOOD adsorption ($\varepsilon_{(DCOOD)} = 2\times10^{-2}$ L at 90 K) on Pd (111) which was initially exposed to various coverages of NH_3 at 90 K 52

3.15 (a) DCOOD adsorption ($\varepsilon_{(DCOOD)} = 2\times10^{-2}$ L at 90 K) on Pd (111) which was initially exposed to 1.4 MLE of NH_3: *m/z* = 28, 16, 43, 45 desorption channels. (b) Comparison of *m/z* = 45 TPD desorption channels of HCOOH/Pd(111) with the m/z = 45 desorption channel of DCOOD/Pd(111) TPRS in the absence of 1.4 MLE NH_3 53

4.1 Schematic representation of the enhancement of FA dehydrogenation on various MnO_x/Pd(111) model catalyst surfaces. Note that this illustration does not account for the actual reaction stoichiometry 55

4.2 Mn $2p_{3/2}$ / Pd*3d* intensity ratio as a function of Mn deposition time 56

4.3 TPD profiles of DCOOD adsorption on clean Pd(111). some of the TPD signals are multiplied by the given factors for clarity 57

4.4 TPD profiles obtained upon $\varepsilon_{DCOOD} = 4\times10^{-3}$ L DCOOD exposure on clean Pd(111) at 123 K. It should be noted that *m/z* = 4 (D_2) desorption signal is not clearly discernible in this low coverage regime 58

4.5 (a) Evolution of *m/z* = 4 (D_2) TPD profiles on MnO_x/Pd(111) as a function of reaction runs. Before each run, a fresh DCOOD was introduced at 123 K with a constant exposure of ε (DCOOD) = 8×10^{-3} L. Mn $2p_{3/2}$ XPS spectra obtained (b) before run 1, (c) after run 1, and (d) after run 2 60

4.6 Change of *m/z* = 4 (D_2) channel as a function of reaction runs 61

4.7 Change of m/z = 4 (D_2) desorption signals as a function of reaction runs at various MnO_x coverages 63

4.8 (a) Change of m/z = 4 (D_2) desorption signals as a function of reaction runs on pre-annealed MnO_x. Note that red curve belongs to the reference D_2 signal (b) Integrated QMS Intensities of m/z =4 (D_2) signals given in a. (c) Mn $2p_{3/2}$ XPS spectrum of MnO_x after annealing 64

4.9 (a) Change of *m/z* = 4 (D_2) TPD profiles on pre-oxidized MnO_x/Pd(111) as a function of reaction runs. At each run a fresh DCOOD was adsorbed at 123K with a constant exposure of ε (DCOOD) = 8×10^{-3} L. Some TPRS signals are multiplied with the given factors for clarity. Mn $2p_{3/2}$ XPS spectrum obtained (b) before run 1, (c) after run 1, and (d) after run 2 65

4.10 TPD Profiles obtained on multilayer MnO_x deposited Pd(111) 65

4.11 TPD profiles obtained upon a DCOOD exposure of 8 x 10^{-3} L at 123 K on (a) MnO_x (0.25 ML)/Pd(111) after three reaction runs, (b) pre-oxidized MnO_x(0.25 ML)/Pd(111). Some of the desorption signals are multiplied with the given factors for better visualization of the data 66

4.12 Integrated TPD intensities of various QMS channels as a function of manganese coverage 69

4.13 TPD profiles that are given in their integrated form in Figure 4 69

4.14 Change of *m/z* = 4 (D_2) channel as a function reaction runs on pre-oxidized MnO_x /Pd(111) 70

E.1 Alternative interpretation of Mn $2p_{3/2}$ spectra given in Figure 4.5 82

E.2 Alternative interpretation of Mn $2p_{3/2}$ spectra given in Figure 4.9 83

E.3 (a) Difference (Δ) XPS intensity spectra of Mn $2p_{3/2}$ XPS spectra represented in Figure 4.5. (b) Difference (Δ) XPS intensity spectra of Mn $2p_{3/2}$ XPS spectra represented in Figure 4.9 84

List of Tables

1.1 Specific energies and energy densities of various commercially available fuels. Adapted from Ref. [6] 2

3.1 Integration temperature intervals for TPD/TPRS histograms given in Figure 3.7d, 3.8a, 3.12, 3.14 52

4.1 Integration Temperature Intervals of TPD Profiles that are given in Figure 4.12..... 79

CHAPTER 1

Introduction

1.1 Future and Sustainability of the Global Energy Demand and Environment

80% of the global energy demand is supplied by fossil fuels such as coal, natural gas and petroleum [1]. Therefore, the nature of the global energy supply chain leads to consumption of large amount of fossil fuels, which in return causes many environmental problems such as increased CO_2 emissions and acid rains [2, 3]. However, this alarmingly large fossil fuel consumption might even double in the future, as the global energy demand is forecasted to more than double by 2050 as a consequence of the rapid growth in world population and global economy [4, 5]. Consequently, utilization of alternative fuel sources is a compulsory task for the sustainability of the energy demand, economy and ultimately the environment.

1.2 Hydrogen as an Alternative Fuel Source

Hydrogen is one of the most promising alternative energy sources since it has a very high specific energy (33.3 KWh/Kg) compared to many other fuel sources (See Table 1.1) [6]. Besides, hydrogen can be used in fuel cell applications which are eco-friendly and efficient [7]. However, one of the major drawbacks of the current hydrogen-based energy applications is the fuel storage. Since gaseous hydrogen has a very low mass density (0.089 kg/m^3 at STP), storing hydrogen in gaseous form creates numerous ergonomic challenges and safety risks [8]. A variety of hydrogen storage and delivery materials were proposed in order to tackle these problems but most of them failed due to their low hydrogen generation capacity and hindered hydrogen generation kinetics [9].

Fuel	Specific Energy (KWh/Kg)	Energy Density (KWh/m^3)
Liquid Hydrogen	33.3	2.37
H_2 (g) (200 bar)	33.3	0.53
Liquid Natural Gas	13.9	5.6
Natural Gas (200 bar)	13.9	2.3
Petroleum	12.8	9.5
Diesel	12.6	10.6
Coal	8.2	7.6
NH_3BH_3	6.5	5.5
Methanol	5.5	4.4
Wood	4.2	3.0

Table 1.1 Specific energies and energy densities of various commercially available fuels. Adapted from Ref. [6].

1.3 Formic Acid as a Potential Hydrogen Source

Formic acid (FA) is one of the highly investigated hydrogen carriers since *i)* it has a relatively high hydrogen density (4% w/w), *ii)* it is in liquid form under ambient conditions (which makes it easy to store), and *iii)* it has low toxicity and flammability [10, 11]. Another advantage of FA is that it can be obtained from various naturally abundant resources, such as CO_2 [12, 13] and biomass feedstocks [14]. These properties of FA make it an auspicious energy carrier for hydrogen-based energy applications.

Catalytic decomposition of FA yields two competing pathways named as dehydrogenation *(1)* and dehydration *(2)*. The dehydrogenation pathway *(1)* allows hydrogen generation since it decomposes FA into H_2 and CO_2; whereas dehydration *(2)* decomposes FA into H_2O and CO. Since dehydration *(2)* does not yield any hydrogen, catalytic selectivity towards dehydrogenation is determined by the prevalence of dehydrogenation pathway over dehydration. Besides, CO formed by dehydration of FA binds to catalytically active sites of precious metals (*e.g.* Pd, Pt *etc.*) in a robust and an irreversible manner under ambient conditions [15-18] causing catalytic poisoning *via* permanent site-blocking [8]. Therefore, presence of two competing catalytic decomposition pathways *(1,2)* makes hydrogen generation from FA a challenging task in spite of its desirable properties.

Pathway *(1):* $HCOOH \rightarrow H_2 + CO_2$, $\Delta G^{\circ}_{298K} = -33.0\ kJ.mol^{-1}$ (*1*)

Pathway *(2):* $HCOOH \rightarrow CO + H_2O$, $\Delta G^{\circ}_{298K} = -13.0\ kJ.mol^{-1}$ (*2*)

1.4 A Literature Review on Formic Acid Dehydrogenation Catalysts

In the literature, it has been shown that it is possible to obtain high FA dehydrogenation selectivity by using homogeneous catalysts such as $[RuH_2(PPh_3)_3CO]$ [19], $Fe(BF_4)_2[P(CH_2CH_2PPh_2)_3]$ [20] and $[Ru_2H(\mu\text{-}H)(\mu\text{-}CO)(CO)_2(\mu\text{-}dppm)_2]$ [21, 22]. However, these homogenous catalyst systems suffer from tedious catalyst synthesis procedures as well as necessity of utilization of a liquid (solvent) reaction medium [23, 24], which creates additional environmental, ergonomic and cost efficiency problems.

On the other hand, FA decomposition has also been extensively studied on several heterogeneous catalytic systems containing group-VIII transition metal surfaces including Pd [8, 25-29], Rh [30-32], Ru [33, 34], Pt [35-37], Cu [38-40], Co[41], Ag[42, 43] as well as Pd-Ag[44] Pd-Au[45] bimetallic systems under ultra-high vacuum (UHV) conditions. These studies reported that coordinatively unsaturated group-VIII transition metal single crystal

surfaces, such as (100) and (110) surfaces of metals that adopt face-centered-cubic (FCC) crystal structure and have planar density *ca.* 10^{13}-10^{14} atoms/cm^2, cannot carry out the FA dehydrogenation selectively. For instance, it was reported that Pd(100) unselectively decomposed FA, where decomposition products were CO and H_2 [26, 27, 29]. In addition, Barteau *et al.* reported that clean Ag(110) surface did not even react with FA [42]. In agreement with these observations, various other experimental studies reported that many coordinatively saturated late transition metal surfaces (*e.g.* (111) surface of FCC metals which has a planar density of ~2x10^{15} atoms/cm^2) were able to carry out FA dehydrogenation effectively [25, 32, 35]. Moreover, these findings were also theoretically verified by Jin *et al.*, where they compared FA dehydrogenation reactivities of Pd(111) *vs.* Pd(100) and reported Pd(111) as the better FA dehydrogenation model catalyst [46]. Besides UHV and DFT studies focusing on two dimensional planar model catalyst surfaces, numerous high surface area mesoporous powder catalysts such as PdNiAg/C [47], Ag/N-rGO, PdAg/N-rGO[48] , Pd-Au/C, Pd-Ag/C [49], graphene supported AuAgPd [50] and as well as Ag-Pd [51-53] Pd-Au [24] core/shell catalysts containing various transition metal active sites have also been explored and demonstrated high activity and selectivity towards FA dehydrogenation.

1.5 Key Aspects of Formic Acid Decomposition on Heterogeneous Catalysts

1.5.1 Effects of Coordination Number of the Catalyst Surface and Adsorption Geometry of Formic acid on Dehydrogenation Selectivity

Figure 1.1 shows the possible adsorption geometries of various carboxylic acids on transition metal surfaces. In particular, two main adsorption geometries were reported for FA. Various experimental [25, 32, 33, 35] and theoretical studies [54-56] revealed that formic acid prefers to attain bidentate configuration (C_{2v} symmetry) on coordinatively saturated group-VIII transition metal surfaces. Contrary to this observation, it has been shown that FA adopts a

monodentate configuration (C_1 symmetry) on coordinatively unsaturated Pd(100) surface [26, 27, 29]. These results revealed the importance of adsorption geometry of the decomposition intermediate as well.

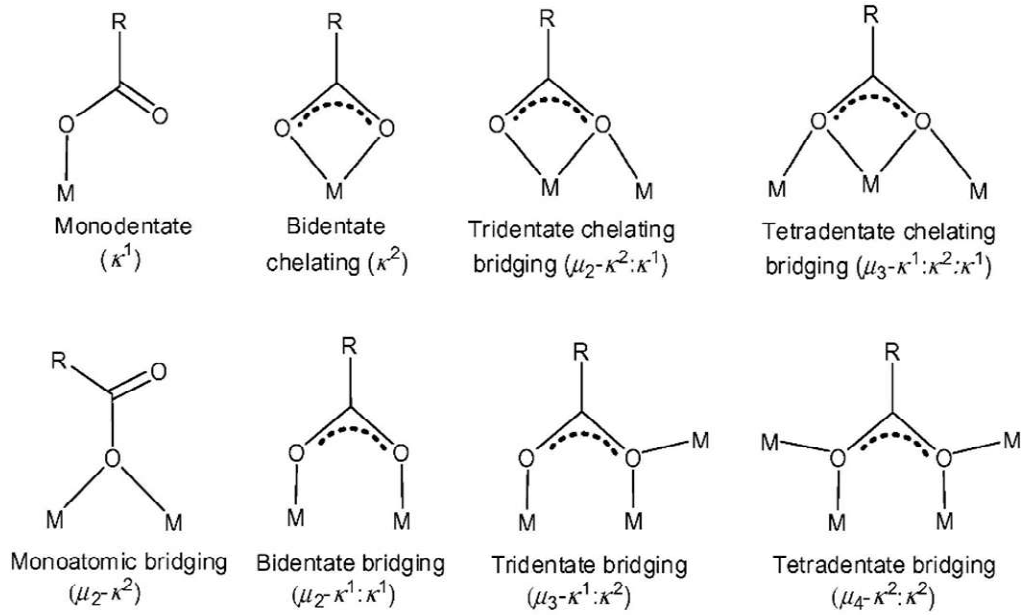

Figure 1.1. Possible absorption geometries formed by carboxylic acids on transition metal surfaces. Adapted from Ref. [57].

For instance, the same studies showed that transition metal surfaces that allow formation of bidentate formate [25, 32, 33, 35] reveal a higher selectivity towards dehydrogenation compared to the metal surfaces that are mainly capable of hosting monodentate formate species [26, 27, 29]. As a result, these studies indicate that;

i) Adsorption geometry of FA and its catalytic decomposition intermediates significantly affect the dehydrogenation selectivity.

ii) Coordination number of the catalyst surface strongly affects the adsorption geometry of FA and its catalytic decomposition intermediates.

iii) Coordinatively saturated transition metal catalyst surfaces are superior in terms of hosting/stabilizing the FA decomposition intermediate (*i.e.* formate) and thus have a higher selectivity towards FA dehydrogenation.

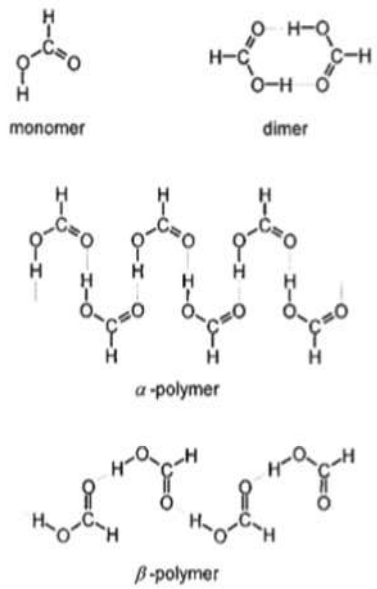

Figure 1.2. Various oligomers/polymers generated upon formic acid adsorption on Ag(111) single crystal surface. Adapted from Ref. [43].

Formic acid is also known to polymerize upon its adsorption on transition metal surfaces. For instance, it has been shown that formic acid forms catemeric structures, *i.e.* oligomeric/polymeric FA units with β-polymer structure (see Figure 1.2), on Pd(111) [25] and Rh(111) [32] surfaces. It has been also reported that FA can polymerize in four different ways on Ag(111) surface [43] , as can be seen from Figure 1.2. However, it should be emphasized that the effects of polymerization of FA units on FA dehydrogenation selectivity did not attract too much attention in the literature.

1.5.2 Relationship between Catalyst Life Span and Dehydrogenation Selectivity

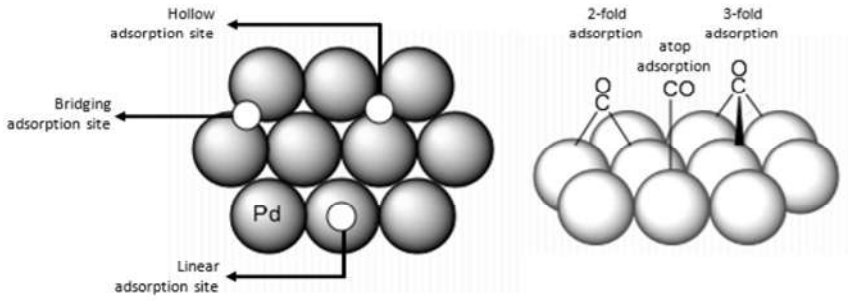

Figure 1.3. Different adsorption geometries of CO on Pd(111) surface. Adapted from Ref. [58].

As mentioned previously, FA dehydration causes formation of significant amounts of carbon monoxide. CO formation is particularly important for the catalyst life span since carbon monoxide irreversibly binds to the active sites of various transition metal surfaces under ambient conditions [15-18]. Transition metal surfaces can host stable CO species on their surfaces as a result of the strong synergy between CO and the surface metal atoms. Three of the most commonly observed CO adsorption geometries on transition metal surfaces are given in Figure 1.3. First of these stable species is called 'atop/ontop/linear CO', where a CO molecule is bound to a single metal atom. Second species is called 'bridging CO', where a CO molecule is coordinated to two adjacent metal atoms. Lastly, a CO molecule that is coordinated to three different metal atoms is called '3 fold-adsorbed CO'. Presence of different stable CO adsorption geometries suggests that a single CO can block/poison up to 3 surface atoms and significantly limit both the catalyst life-time and performance.

1.6 Effects of Brønsted and Lewis Bases on Formic Acid Dehydrogenation Selectivity of Heterogeneous Catalysts

Pd is among the most active catalytic metals which is capable of generating ultra-high purity H_2 from biomass side-products such as formic acid [53, 59, 60]. These heterogeneous catalytic systems are frequently coupled with additional bases which can act as catalytic promoters and facilitate the catalytic FA decomposition [8, 61]. Similarly, catalytic sites/promoters/support surfaces are also usually functionalized with bases in order to achieve a higher catalytic H_2 production selectivity.

In the literature, it has been shown that Lewis bases, *i.e.* substances that can donate a pair of non-bonding electrons, can significantly enhance the performance of FA dehydrogenation catalysts. For instance, it has been reported that creating Lewis basic oxygen species on coordinatively saturated group-VIII transition metal surfaces;

i) hinders FA polymerization on the surface

ii) enhances FA dehydrogenation selectivity by increasing the formate stability

under UHV conditions [25, 32, 35]. In accordance with these observations, it has been also reported that high surface area Pd-Ag [59] and Pd-Au [62] bimetallic nanoparticles (NP) which are promoted with MnO_x (*i.e.* a reducible oxide which contains Lewis basic sites) yielded an extremely high FA dehydrogenation activity, where MnO_x domains reported to *i*) increase FA adsorption on the catalyst surface through the formation of new FA adsorption sites, *ii*) facilitating FA deprotonation, *iii*) stabilize the formate species on the catalyst surface, and *iv*) capture/store the catalytically generated CO(g) side product in the form of carbonates and prevent CO-poisoning of the Pd active sites on which formate species are converted into the ultimately desired catalytic product, H_2. On the other hand, it was also reported that Brønsted bases, *i.e.* substances that are proton (H^+) acceptors, can also notably enhance the FA dehydrogenation selectivity. For example, it has been shown that amine functionalization (Brønsted base) caused an extra boost in $H_2 + CO_2$ production of Pd-Ag/MnO_x catalyst [59]. Similar to this observation, Mori and his co-workers also showed that Pd-Ag catalyst embedded

inside a -N(CH_3)$_2$ (Brønsted base) functionalized polymer matrix had a significantly higher H_2 conversion compared to other Pd-Ag NP embedded in matrices with different functional groups, where -N(CH3)$_2$ is reported to enhance hydrogen formation *via* facilitating FA deprotonation [63]. It should be emphasized that positive effect of Brønsted bases on FA dehydrogenation is not unique for only Pd based catalysts. For example, Yadav *et al.* showed that presence of amine (-NH_2) groups grafted on the support material can turn Au NPs, which are relatively inactive in FA dehydrogenation, into significantly active FA dehydrogenation catalysts *via* enhancing the FA adsorption through a process called "Strong Metal-Molecular Support Interaction" (SMMSI) [64]. These studies clearly indicate that Brønsted and Lewis acid/base chemistry can be successfully used in order to improve hydrogen production from FA.

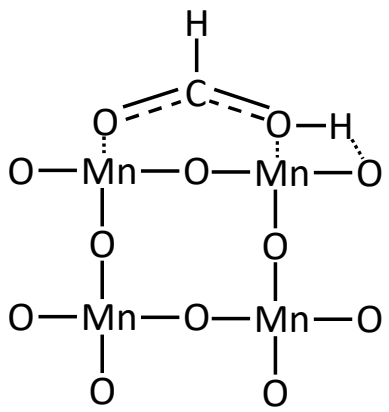

Figure 1.4. Schematic representation of formic acid adsorption on MnO_x surface. Note that this illustration does not account for any of the actual MnO_x lattice structures.

1.7 Motivation of the Current Study

Most of the commercially available heterogeneous catalysts consists of metallic NPs along with the support material. Usually the main goal behind coupling the catalytically active metal(s) with a support material is to have robust mechanical properties allowing catalyst to be

used in successive reaction cycles. Moreover, support materials can also significantly improve the catalytic activity since they can enhance the dispersion of catalytically active metals on the surface and form metal-support interface with unique electronic properties. For instance, it has been shown that TiO_2 support material significantly enhances Au NPs CO oxidation activity by increasing Au NPs CO adsorption properties *via* donating electrons to Au NPs from their oxygen vacancies at the metal-support interface [65, 66]. On the other hand, presence of catalyst support makes the catalyst structure very complex and thus creates significant problems in terms of achieving molecular-level fundamental information regarding structure-catalytic reactivity relationships.

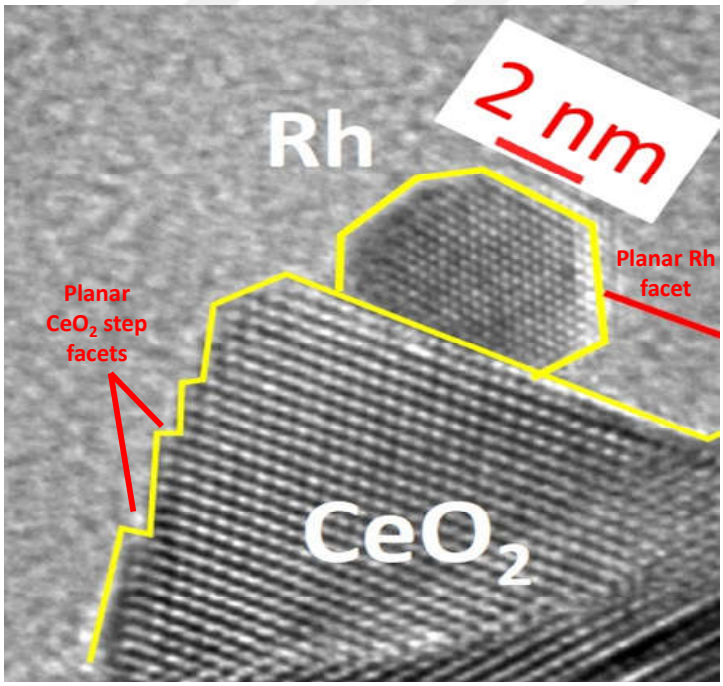

Figure 1.5. TEM image of Rh/CeO_2. Adapted from Ref. [67].

Figure 1.5 represents a high-resolution TEM image of a dry glycerol reforming Rh/CeO_2 NP catalyst [67]. This image clearly shows that both Rh active site and CeO_2 support material expose ordered surfaces, *i.e.* planar Rh facets and planar CeO_2 step facets, where surface parameters of this facets are governed by the surface energy of the NPs. Therefore, this

particular example demonstrates that complex chemical structures of NP catalysts can be broken down into 2D-facets with known surface parameters. In this aspect, atomically well-defined 2D-model catalysts are very useful tools for obtaining information about structure-catalytic reactivity relationships since they can be used to model catalytic properties of certain facets of real NP catalysts. However, well-defined single crystal planar model catalysts can only be used in ultra-high vacuum (UHV) conditions since surface structures of these well-defined catalysts often deteriorate/reconstruct upon adsorption of gases at elevated pressures close to atmospheric pressures [68].

Currently, literature lacks detailed molecular-level understanding in terms of effects of Brønsted and Lewis bases on the FA dehydrogenation ability of atomically well-defined transition metal single crystal surfaces. Therefore, this presented dissertation work focuses on the effects of NH_3 (a Brønsted base) and MnO_x (a reducible metal oxide possessing Lewis basic oxide/O^{2-} ions) on FA dehydrogenation ability of Pd(111) single crystal model catalyst under UHV conditions in order to probe explicit structure-reactivity relationships. In this work, Pd(111) was chosen as the model catalyst since *i)* Pd metal is one of the most active FA dehydrogenation catalysts [53, 59, 60] and *ii)* Pd (111) is the most active facet of Pd for FA dehydrogenation [25, 46, 55]. Moreover, NH_3 and MnO_x were chosen as model Brønsted and Lewis bases respectively due to their exceptionally positive influence on FA dehydrogenation [59, 62-64]. Results represented in this dissertation reveal valuable molecular level information about the influence of Brønsted and Lewis bases on catalytic FA dehydrogenation reactions.

CHAPTER 2

Experimental

2.1 Experimental Setup

Figure 2.1 represents the photograph of the experimental setup that was used to conduct this study. This setup has a base pressure of 1×10^{-10} Torr and this ultra-high vacuum environment is obtained *via* a turbomolecular pump (Varian, TV 551 Navigator, with a pumping speed of 550 L/s) that is coupled to an oil-free scroll pump (Agilent Varian SH-110). Besides, the UHV chamber is equipped with an X-ray Photoemission Spectroscopy (XPS) setup, a custom-made Low Energy Electron Diffraction (LEED) setup, a custom-made Infrared Reflection Absorption Spectroscopy setup (IRAS), temperature programed desorption (TPD) and temperature programmed reaction spectroscopy (TPRS) modules, custom-made manganese (Mn) thin film evaporators and an Ar^+ sputtering ion gun (LK Technologies, NGI3000) which is used for surface cleaning purposes. Moreover, chamber also contains three separate gas dosing lines equipped with separate high precision leak valves, where each of these lines were allocated for a specific adsorbate. Besides, the setup contains a titanium sublimation pump (TSP) (Varian, Model 916-0017) which facilitates the removal of sticky gases (*e.g.* H_2O) or gases with low compression factor (*e.g.* H_2) from the UHV chamber. Currently used Pd(111) single crystal sample (10 mm-diameter × 1 mm-thickness disc, polished on both side, purity > 99.999%, MaTeck GmbH) was affixed on Ta wires which allowed cooling of the sample with liquid nitrogen to 90 K and heating it up to 1073 K *via* resistive heating. The temperature of the sample was measured by using a K-type thermocouple (thickness: 0.005 in., Omega Inc.) which is spot-welded on the upper side of the Pd(111) disc.

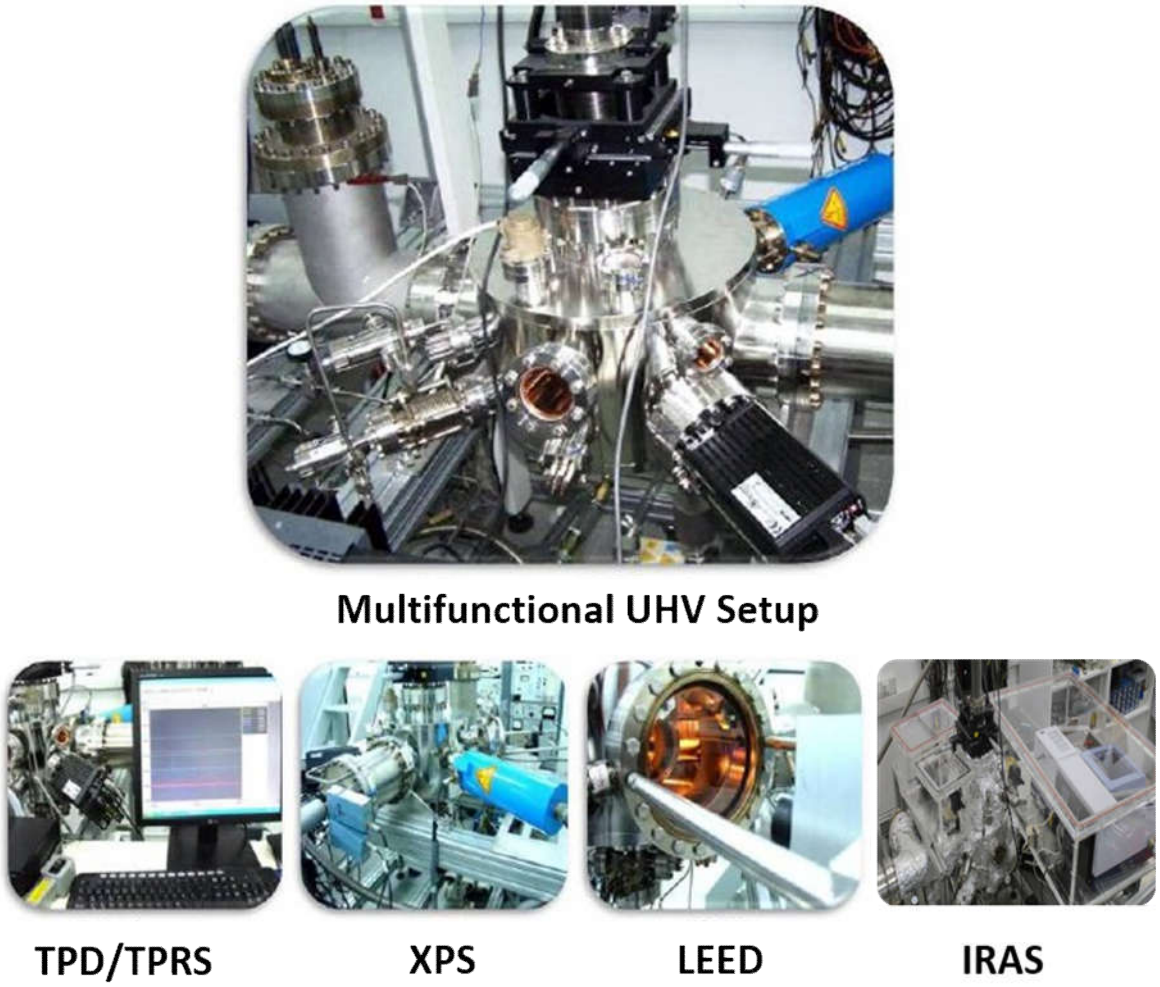

Figure 2.1. Photographs of the UHV experimental setup.

2.2 Surface Characterization Techniques

The work presented in this thesis was performed by using multiple surface characterization techniques. In this study, LEED was used to obtain surface-sensitive crystallographic information about the single crystal model catalyst. In addition, XPS was used in order to make surface-sensitive elemental/oxidation state analysis and quantifiy the coverage of MnO_x thin films on Pd(111) prepared *via* thermal evaporation method. TPD/TPRS techniques were used in order to quantify the adsorbate coverages and determine reaction products, providing mechanistic information about the FA dehydrogenation reactions. Some of

the fundamental aspects of the currenlty utilized experimental techniques are given in the following sections.

2.3 Low Energy Electron Diffraction (LEED)

Low energy electron diffraction (LEED) is a unique technique that is used for determining the surface structures of single crystals and well-defined adsorbate overlayers [69]. LEED makes use of low energy electrons (25-200 eV range) since outermost layer of a metal, *i.e* the surface, can only be *selectively* probed by using electrons with low kinetic energies, as can be seen from Figure 2.2.

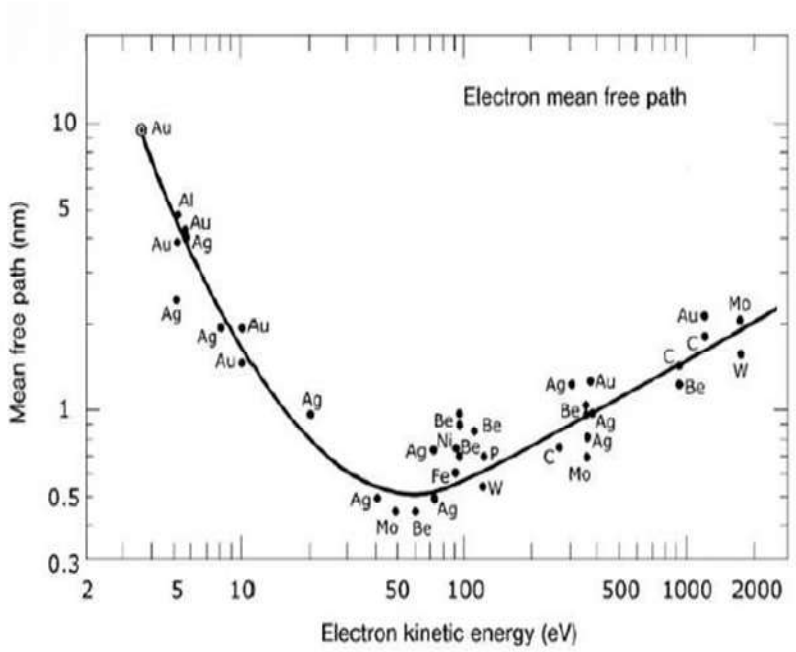

Figure 2.2. Plot of electron inelastic mean free path (IMFP) values of various materials as a function of electron kinetic energy. (The "universal curve") Adapted from Ref. [69].

In this technique, the sample of interest is bombarded by low energy electrons and this bombardment causes electrons to elestically scatter from the surface. Then these elastically scattered electrons are accelarated towards a phosphoresence screen. During the this scattering

process, crystallinity/order of the surface allows elastically scattered electrons to have constructive intereference. The constructive interference process is governed by 2D-Bragg conditon given below, where n corresponds to the diffraction order, λ corresponds to the wavelenght of the electrons, d is the surface lattice parameter and θ is the angle of diffraction of electrons with respect to the surface normal.

$$n\lambda = d\sin(\theta) \tag{2.1}$$

The constructive interference of elastically scattered electrons is observed as a diffraction pattern on the phophoresence screen (See Figure 2.4a) and this pattern gives information about the surface crystal structure. It should be noted that LEED diffraction patterns reveal information in the momentum space (*k*-space/reciprocal space) of the elastically scattered electrons. Therefore, obtained diffraction patterns does not directly correspond to the real space positions of the atoms on the surface. On the other hand, the Pontryagin duality [70] between the *k*-space and the real space allows translation of reciprocal space information into real space information by relatively simple linear algebraic vectoral operations. A simple representation of the relationship between the momentum and the real vector spaces can be found in Figure 2.3 [71].

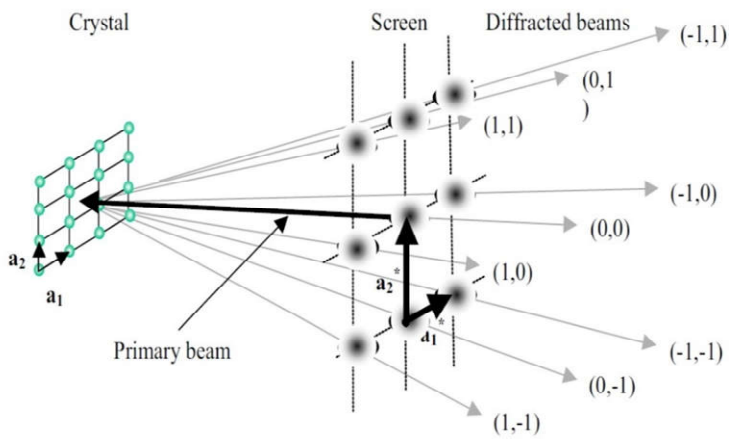

Figure 2.3 Schematic representation of a LEED experiment. (a_1, a_2) are unit cell vectors and (a_1^*, a_2^*) are the corresponding momentum space vectors. Adapted from Ref. [71].

As can be seen from Figure 2.4b, a LEED setup has three main components. The electron gun generates electrons *via* thermionic emission and generated electrons are accelerated towards the sample. In general, a negative potential is applied on the retarding grids shown in Figure 2.4b since they are used for filtering out the inelastically scattered electrons from the surface in order to achieve more clear diffraction patterns and eliminate background illumination in the LEED images. Lastly, a positively biased luminescent screen (5.14 kV in the current work) collects the remaining elastically scattered electrons from the surface and generates spots on the screen that corresponds to the diffraction pattern obtained from the surface.

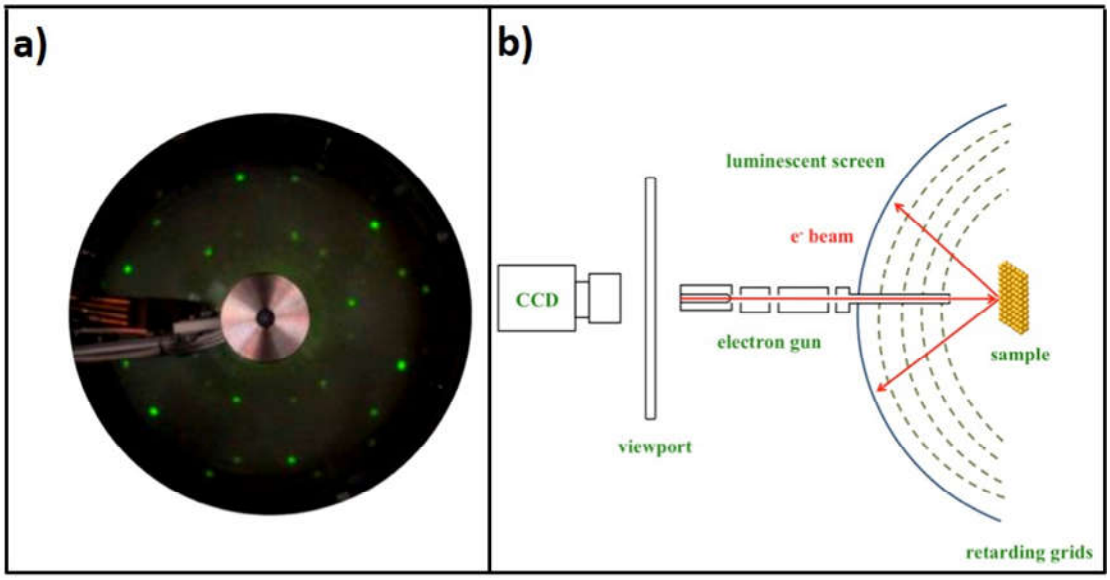

Figure 2.4. (a) Sample LEED diffraction pattern obtained on a phosphorescence screen. (b) Schematic of a LEED setup. Adapted from Ref. [72].

In the current work, LEED measuremets were done by using electrons with ~70 eV energy since these electrons can selectively probe the sample surface and wavelength of these electrons (*ca.* 15 nm) are also sufficient enough to resolve the lattice parameter of Pd surface atoms and give information about the surface crystal structure.

2.4 X-Ray Photoelectron Spectroscopy (XPS)

X-Ray Photoelectron Spectroscopy (XPS) is technique that is used for elemental and oxidation state analysis. The basis of this technique is the photoelectric effect, where core level electrons are ejected from a solid material as a result of the X-Ray irradiation [69]. In summary, in an XPS measurement, X-Ray photons with energy hv is absorbed by a core electron with a certain binding energy (BE). Thus, kinetic energy (KE) of an ejected electron can be calculated from Equation 2.2, where the work function of the spectrometer is denoted with ϕ.

$$KE = hv - BE - \phi \tag{2.2}$$

The electrons that are emitted from the sample surface as a result of this process is called as 'photoelectrons' and the kinetic energy of these electrons typically range within 0-1.1 keV [73]. Consequently, the kinetic energy range of photoelectrons makes XPS a surface sensitive technique since IMFP of electrons is less than 2 nm between 100 eV - 1.1 keV energy range, as can be seen in Figure 2.2.

XPS signals are labelled based on the total angular momentum quantum number (j) of the ejected photoelectrons that is given in Equation 2.3.

$$j = l + s,\ j \geq 0 \tag{2.3}$$

As can be seen from Equation 2.3, total angular momentum quantum number is the summation of the angular momentum quantum number (l) and spin quantum (s) of an electron. Since s can only be either 1/2 or –1/2, a single photoelectron will generate two different signals at every energy level when $l > 1$. For instance, photoelectrons ejected from Pd*3d* level will have two different signals labelled as Pd $3d_{5/2}$ and $Pd_{3/2}$ (see Figure 2.10), this is also referred as spin-orbit coupling [69].

As can be seen from Figure 2.5, a basic XPS setup consists of two main components, namely the X-Ray source and the photoelectron energy analyzer. In the current work, the used

X-Ray source had a dual anode configuration (Riber Model CX 700, see Figure 2.5a) which consisted of Mg (*hv* = 1253.6 eV, full width half maximum, (FHWM) = 0.70 eV) and Al (*hv* = 1486.6 eV, FHWM = 0.85) anodes. In this anode configuration, anode materials were coated on a cupper surface since the high thermal conductivity of cupper allows anodes to be cooled *via* water cooling. Besides, the X-Ray source contained two tungsten filaments that are in close proximity with Mg and Al anodes and these filaments provided the electrons for X-Ray generation *via* thermionic emission. During all XPS measurements, X-Rays were generated by applying 250 W power on the Mg anode (Anode voltage = 10 kV, Filament emission current = 25 mA).

Two different types of energy analyzers used in XPS spectrometers are given in Figures 2.5b and 2.5c.

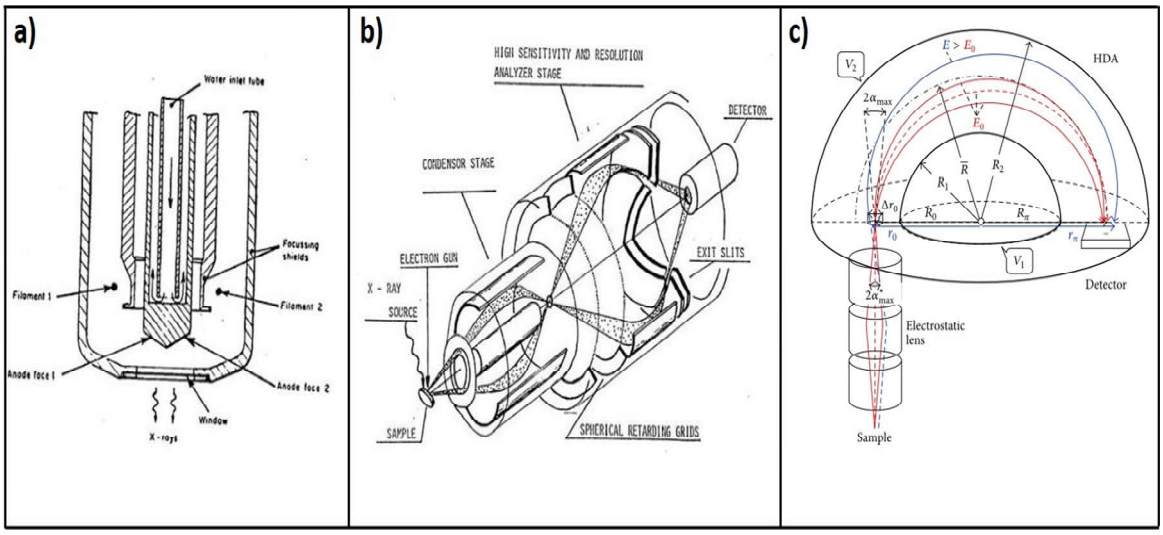

Figure 2.5. (a) Schematic of the dual anode X-Ray source used in this work. Adapted from Ref [74]. (b) Schematic of the double-pass cylindrical mirror energy analyzer used in this work. Adapted from Ref. [75]. (c) Schematic of a hemispherical energy analyzer Adapted from Ref. [76].

The energy analyzer that is given in Figure 2.5b is called as double-pass cylindrical mirror energy analyzer (CMA) and this type of energy analyzer (Riber EA 150) is present in our current XPS configuration. CMA has two stages as can be seen from Figure 2.5b. In the

first stage, photoelectrons are focused to the entrance slit of the analyzer, where this process provides some tolerance for the sample alignment (~3 mm). At the second stage, previously focused photoelectrons are slowed down by the negatively biased spherical retarding grids. As a result of this retardation, electrons that are only in a certain energy range can pass-through the second stage and reach the electron multiplier. Therefore, the energy resolution depends on the potential difference between the initial stage and the spherical retarding grids (F_1). Consequently, CMA acts as a band pass filter. In the current work, F_1 is optimized as 27 V for a survey scan and 7 V for a region scan. On the other hand, the voltage that is used for focusing the photoelectrons towards the electron multiplier (F_2) is optimized as 50 V for survey scan and 25 V for region scan.

The hemispherical energy analyzer given in Figure 2.5c (HMA) is commonly used in modern XPS devices. It works by applying a potential difference on the photoelectrons coming from the surface and bending their trajectories. Since photoelectrons with higher kinetic energies will have a longer flight time compared to the lower energy photoelectrons, they will hit a further point on the detector plane. As a result, HMA resolves photoelectron kinetic energies by making the use of different trajectories followed by the photoelectrons. Consequently, HMA has a better energy resolution compared to CMA.

2.5 Temperature Programmed Desorption/Reaction Spectroscopy (TPD/TPRS)

Temperature programmed desorption (TPD) is a charcterization technique that is used for obtaining information about the desorption processes occuring on particular adsorbent/substrate systems. In cases where more than one adsorbate are present on the substrate surface or in the existence of a thermally induced chemical reaction, TPD technique is also refered as temperature programmed reaction spectroscopy (TPRS). In these techniques,

at first, gas phase atoms/molecules are adsorbed on a substrace surface at a specific adsorption temperature. Then, substrate is heated *via* a linear temperature ramp while the desorbed species are simultatenously monitored by a mass spectrometer. In an environemnt where pumping speed is sufficient, shapes of the partial pressure curves that are obtained from the TPD experiments give information about the kinetic and thermodynamics of adsorption [77].

In a TPD experiment, the rate of desorption can be mathematically expressed by using the Polanyi-Wigner equation given in Equation 2.6 [78].

$$r = -\frac{d\theta}{dT} = k_{des}\theta^m \tag{2.4}$$

$$T = T_o + \beta t,\ \beta = \frac{dT}{dt} \tag{2.5}$$

$$r = -\frac{d\theta}{dT} = \frac{k_{des}}{\beta}\theta^m = -\frac{d\theta}{dt} = k_{des}\theta^m = A\,\theta^m e^{(\frac{E_{des}}{RT})} \tag{2.6}$$

Where r is the desorption rate, θ is the adsorbate coverage, m is the order of desorption, t is the time, k_{des} is the rate constant of desorption, A is the pre-exponential factor, E_{des} is the desorption energy, R is the universal gas constant, T is the temperature, T_o is the initial adsorption temperature and β is the linear heating rate. Equation 2.6 predicts that desorption process occurs only at particular temperatures since the magnitude of temperature should be high enough to overcome E_{des} so that the desorption process can take place. Besides, Polanyi-Wigner equation also indicates that adsorbates with different desorption orders will yield desorption curves with different shapes. The three most commonly observed desorption orders and their corresponding desorption curves are given in Figure 2.6. A zeroth order desorption (m = 0) means that desorption rate is independent of adsorbate coverage. Consequently, the zeroth order desorption is obtained in a regime where there is an excess supply of adsorbates on the substrace surface. Figure 2.6a shows how increasing the coverage affects the zeroth order desorption process. As can be seen from Figure 2.6a, increasing the coverage does not alter the leading edge profiles of the TPD spectra. However, it shifts the desorption maxima of

the TPD spectra towards higher temperatures, where the increase in the desorption maxima is mainly due to the longer duration of time required to complete the desorption with increasing number of adsorbates on the surface.

First order desorption kinetics (m = 1) indicates that desorption rate is linearly proportional to the adsorbate coverage. This type of desorption kinetics is observed when the adsorbates can reversibly and non-dissociatively/molecularly adsorb and desorb from the surface. As can be seen from Figure 2.6b, first order desorption peaks have a certain asymmetry and increasing the coverage does not change the desorption temperature of the first order desorption peaks.

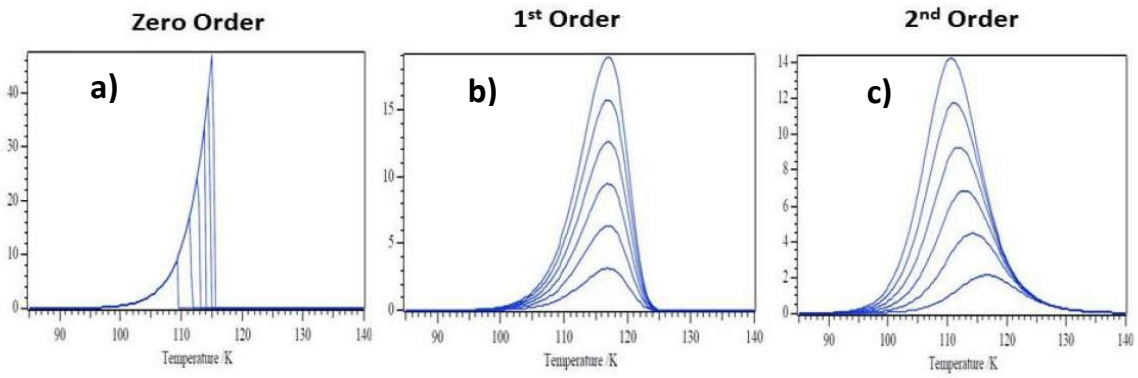

Figure 2.6. Sample TPD spectra obtained for (a) zeroth order (b) first order (c) second order desorption kinetics as a function of increasing adsorbate coverage. Adapted from Ref. [68].

Moreover, for adsorbates that show both first order desorption kinetics and layer-by-layer growth on the substrate surface, TPD intensities corresponding to sub-monolayer coverages eventually reach a saturation when the substrate surface is totally occupied by the adsorbates (see Figure 3.2.). As a result, this specific saturation point can be used as a reference for 1 monolayer (ML) and can be utilized to quantify the adsorbate coverage of the remaining TPD profiles [71]. On the other hand, second order desorption (m = 2) kinetics means that desorption rate is directly proportional to the square of the adsorbate coverage. This type of

desorption kinetics is obtained upon recombinative desorption of species that are originally dissociatively adsorbed on the surface [78]. It should be noted that an increase in adsorbate coverage increases the collision probability of the dissociated species on the surface. Consequently, as can be seen from Figure 2.6c, desorption maxima of second order TPD profiles shifts to a lower temperature with increasing adsorbate coverage.

As mentioned earlier, TPD profiles can be also used extract information about kinetics and thermodynamics of desorption. For instance, Redhead Analysis can be used in order to calculate the desorption energy of an adsorbate following first order desorption kinetics [79]. Equation 2.7 represents the Redhead Equation that is used for determining the adsorption energies of adsorbates with 1st order desorption kinetics, where kinetic parameters are assumed to be independent of adsorbate coverage [69]. It should be noted that T_m corresponds to the desorption maxima of the TPD peak in Equation 2.7.

$$E_{des} = RT_m \left(ln\frac{AT_m}{\beta} - 3.46\right) \tag{2.7}$$

In Equation 2.7, A/β ratio gives information about the statistical density of microstates. It should be noted that desorption processes become more facile with increasing number of available microstates at the transition state. Consequently, A/β ratio is usually set between 10^8 – 10^{13} K^{-1} since desorption transition state is assumed to be neither tight nor loose, revealing a moderate magnitude of statistical density of microstates.

Another method that can be used for obtaining information about desorption kinetics/thermodynamics is the leading-edge analysis. In this technique, a linear portion of the TPD curve that is located around the peak take-off region is used in order to calculate the desorption energy of an adsorbate [80]. By using the data points that corresponds to the linear portion of the TPD curve, a ln(r) vs 1/T curve is constructed and desorption energy is calculated from the slope of this curve. While the leading-edge analysis requires a smaller number of

assumptions/approximations compared to the Redhead Analysis, the former approach is often less frequently used as it requires TPD profiles with very high S/N ratio for achieving precise numerical results [69].

Figure 2.7 represents the schematic of a TPD/TPRS module that is used in UHV surface science applications. In the current work, PID-controlled linear sample heater (Heatwave, Model 101303) and a quadrupole mass spectrometer (QMS) (Ametek Dycor Dymaxion DM200) were used for the TPD/TPRS experiments. All of the TPD/TPRS measurements were performed with a heating rate of 1 K/s, 70 eV QMS beam energy and 30 ms dwell time for each desorption channel. Temperature logging rate was 5 s^{-1} (corresponding to a temperature recording step size of 0.2 K) while QMS had a unit resolution that allowed us to distinguish *m/z* peaks separated by 1 unit (*e.g m/z* = 46 from *m/z* = 47).

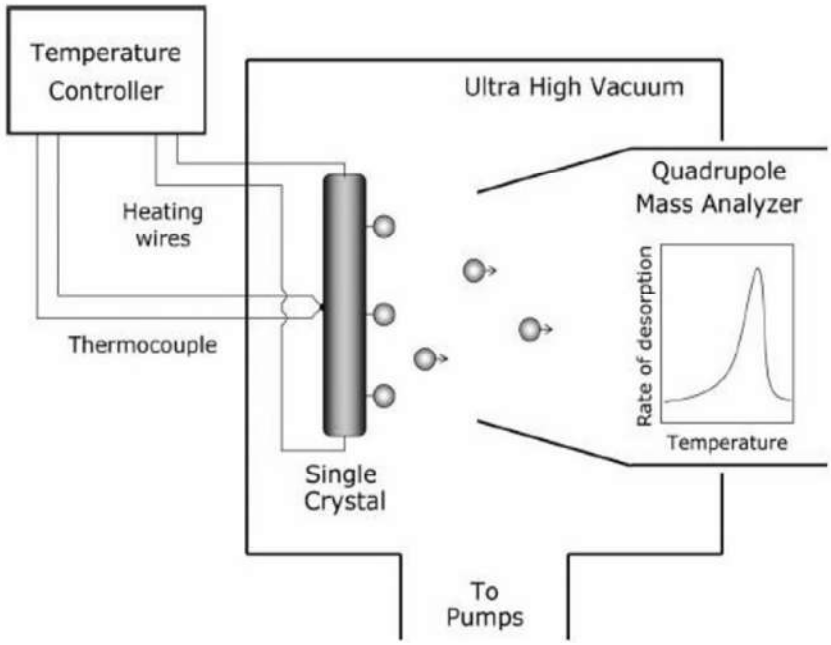

Figure 2.7. Schematic of a TPD/TPRS module that is used for UHV surface science applications. Adapted from Ref. [69].

2.6 Experimental Procedures

2.6.1 Cleaning of Pd(111) Single Crystal Model Catalyst

At the beginning of every experiment, Pd(111) sample surface was cleaned by using three different procedures depending on the amount of the contaminations present on the Pd(111) surface. The first procedure involved multiple cleaning cycles with O_2(g), where Pd(111) was exposed to oxygen (Linde AG, purity ≥ 99.999%)) by using a high precision leak valve allocated for oxygen dosage (P_{O2} = 1.0 × 10^{-8} Torr, 5 min at 600 K) and then consecutively annealed at 1000 K for 5-10 min in UHV. In the second method, after exposing the Pd(111) sample to the conditions given above, sample was flash-heated to 1000 K and then etched by Ar^+ (Ar(g), Linde AG, purity ≥ 99.999%) at room temperature (RT), followed by successive annealing at 1000 K in UHV for 5-10 min. The last procedure included Ar^+ sputtering at RT and subsequent annealing of Pd(111) at 1000 K in vacuum for 5-10 min. After conducting one of these cleaning procedures, cleanliness of the Pd(111) model catalyst was verified by performing XPS measurements and blank TPD experiments.

Figure 2.8 represents XPS survey spectrum and a blank TPD profile for *m/z* = 28 (CO) obtained from a clean Pd(111) surface. Since the major contamination on the clean Pd(111) surface was mostly due to the adsorption of background CO, we rutinely performed *m/z* = 28 (CO) TPD and XPS analyses after the cleaning protocols. As can be seen from Figure 2.8a, within the detection limit of the XPS spectrometer, Pd(111) surface does not contain any considerable contaminations after cleaning the surface with Ar^+ sputtering. *m/z* = 28 (CO) TPD profile given in Figure 2.8b is also in accordance with this observation, since Pd(111) surface practically does not yield any strongly-bound CO species on the surface after cleaning. It should also be pointed out that the survey spectrum contains 'ghost' peaks, *i.e.* the XPS signals which are observed due to the simultaneous irradiation of the sample with unwanted X-Ray emission coming from Al portion of the Mg/Al dual anode.

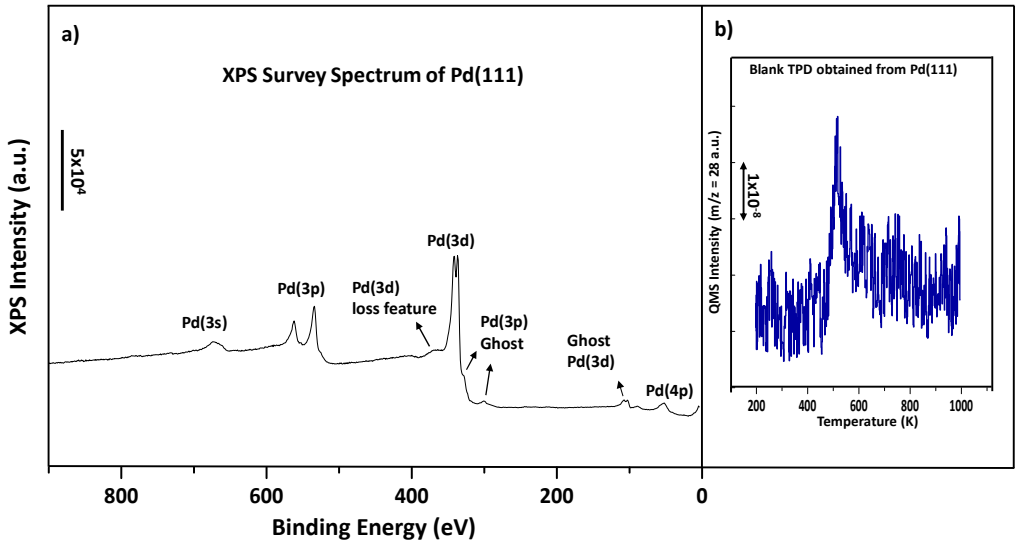

Figure 2.8. (a) XPS Survey Spectrum obtained from clean Pd(111). (b) *m/z* = 28 (CO) TPD profile obtained from blank TPD obtained from clean Pd(111).

2.6.2 Doubly-Deuterated Formic Acid Residual Gas analysis (RGA)

Doubly-deuterated formic acid residual gas analysis (RGA) was done in order to verify the deuterium labelling of DCOOD. It should be noted that our QMS was able to perform RGA analysis within a 40 amu range. Consequently, RGA data was collected between *m/z* = 10 and *m/z* = 40 range in order to be able to detect the signals that can conclusively identify the presence of DCOOD. Figure 2.9a represents the DCOOD RGA that is obtained at 298 K (RT) when chamber was filled with 5.5×10^{-8} Torr of DCOOD while Figure 2.9b represents the background RGA of the chamber that is obtained prior to DCOOD exposure at the same temperature. As can be seen from Figure 2.9b, background RGA spectrum does not contain any *m/z* = 30 (DCO) and *m/z* = 46 (DCOO) signals, which are two conclusive signals that belong to the fragmentation of DCOOD. On the other hand, Figure 2.9a reveals that DCOOD exposure causes formation of relatively weak *m/z* = 30 (DCO) and *m/z* = 46 (DCOO) signals. Consequently, presence of *m/z* = 30 (DCO) and *m/z* = 46 (DCOO) fragments in Figure 2.9a verified the presence of the doubly-deuterated formic acid.

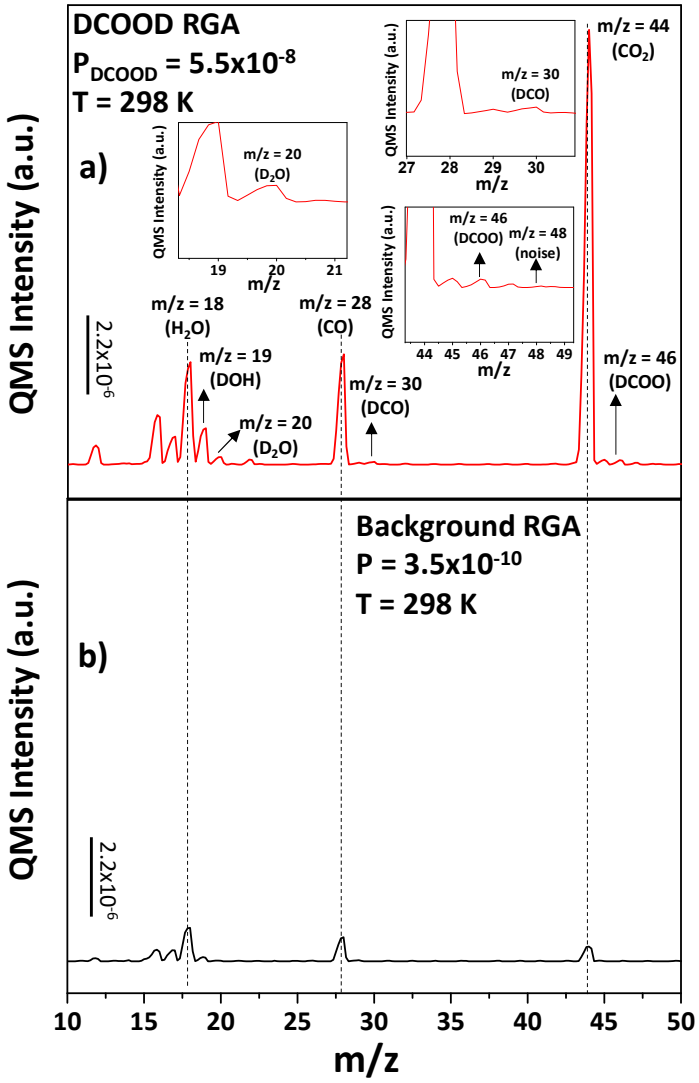

Figure 2.9. (a) DCOOD RGA obtained at 298K and P_{DCOOD}= 5.5x10^{-8} Torr. (b) Background RGA spectrum of the UHV chamber obtained at 298K.

2.6.3 Protecting Deuterium Labelling of Doubly-Deuterated Formic Acid

In the current work, we used doubly-deuterated formic acid (DCOOD) (Cambridge Isotopes Laboratories Inc., Formic Acid-D2, D > 98 %, D_2O < 5 %) as the FA source, since deuterium labelling allowed us to distinguish the specific contributions of FA, NH_3 and MnO_x to the dehydrogenation process (see Chapters 3 and 4). Consequently, some precautions were taken in order to prevent contamination of DCOOD with H-containing species. First, DCOOD

(l) was transferred into a UHV-compatible glass bulb attached to a VCR Swagelok nupro UHV valve in a glove box in order minimize H-D exchange events that can occur between the atmospheric H_2O and DCOOD. Then, this DCOOD (l) containing bulb was connected to the gas manifold of the UHV chamber dosing lines. The container bulb was also covered with a thick layer of aluminum foil to avoid photochemical reactions. Lastly, before each FA experiment, a fresh dose of DCOOD(g) (25 Torr) was transferred into the manifold (after 1-2 freeze-thaw cycles) and to the dedicated DCOOD dosing line since FA is known to decompose upon its long-term interaction with stainless steel [25].

2.6.4 Characterization of Pd(111) Single Crystal Model Catalyst

XPS and LEED was used in order to characterize oxidation state and surface crystal structure of the clean Pd(111) surface. Figure 2.10 represents the Pd*3d* spectrum that is obtained from clean Pd(111). As can be seen from Figure 2.10, Pd $3d_{5/2}$ signal is located around 335.1 eV, which indicates that clean Pd is in metallic form [81].

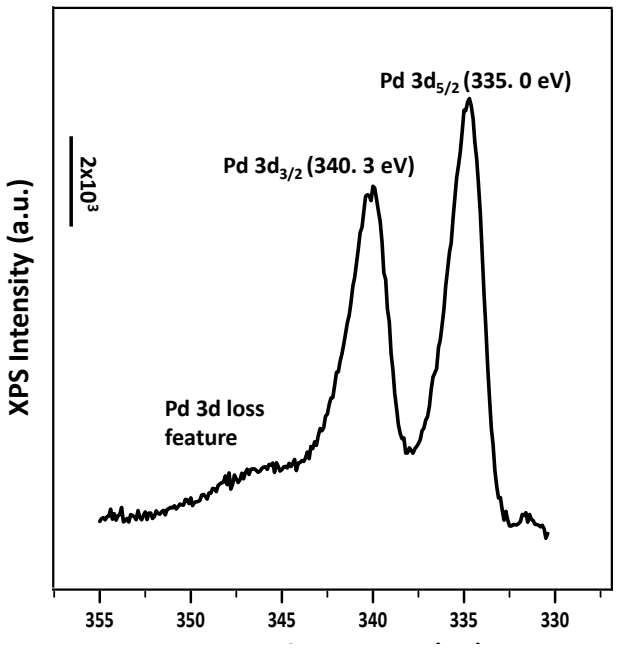

Figure 2.10. Pd*3d* XPS spectrum of clean Pd(111)

Figure 2.11a represents the LEED pattern of an unclean sample while Figure 2.11b represents the LEED pattern of a clean Pd(111) surface. Note that clean Pd(111) surface yields much brighter and sharper spots on the phosphorescence LEED screen since more low energy electrons can reach to the surface and scatter from Pd atoms in the absence of contaminations. Besides, hexagonal c(1x1) LEED patterns observed in both figures verified the (111) crystal structure of the clean Pd single crystal surface as well as showing that contaminations generally do not disrupt the (111) surface crystal structure of the model catalyst.

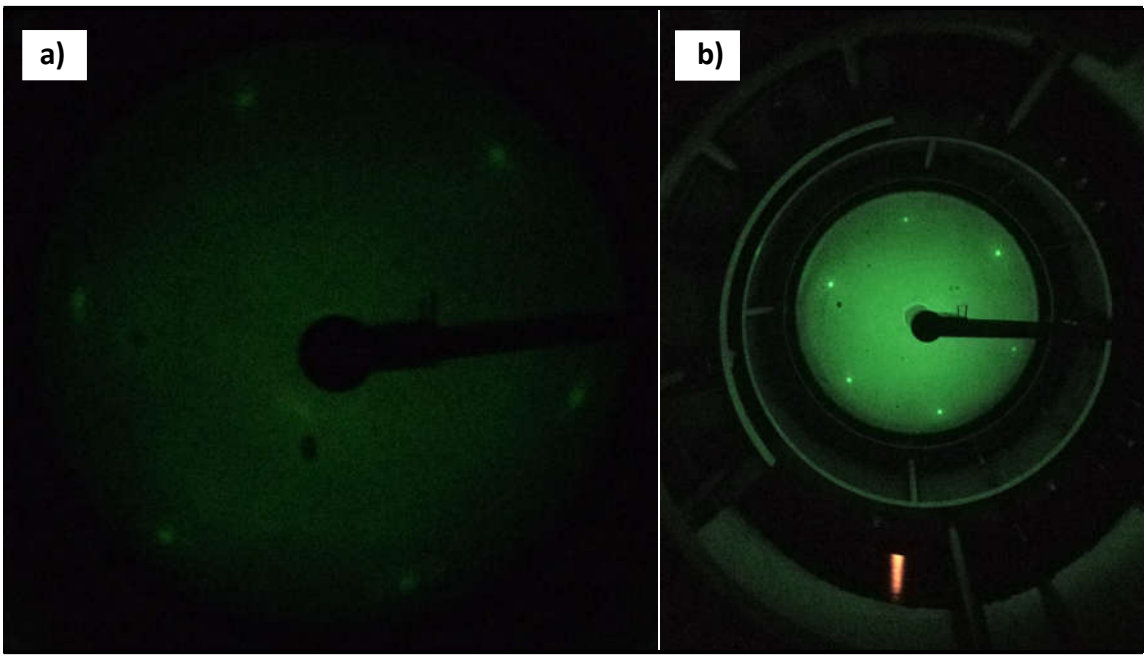

Figure 2.11. (a) LEED pattern of unclean Pd(111) surface (b) LEED pattern of clean Pd(111) surface

2.6.5 Deposition of Manganese (Mn) on Pd(111)

Mn(s) was deposited on the Pd(111) surface *via* a thermal evaporation process. In this method, high purity Mn metal (MaTek Manganese foil casted, purity: 99.9%) was evaporated in vacuum and then the source vapor was condensed on the surface of specific substrate [82]. Figure 2.12a shows the three custom-made Mn-evaporators that are designed for the thermal

evaporation process, where these designs are labelled as 1, 2 and 3 respectively. In design 1, a rectangular Mn piece (1cm x 1cm x 2cm) was sandwiched between two tantalum (Ta) foils and these foils were spot welded from their sides in order to achieve mechanical stability. In design 2, a Mn piece with identical dimensions was placed inside a tungsten (W) coil. Similarly, in design 3, another identical Mn piece was placed between two claws which are made from Ta foil. It should be noted that in all of the designs, two tungsten (W) wires were spot welded to the both sides of each Mn-evaporator (See Figure 2.12b) in order to overcome the depth of the evaporator line and place the Mn-evaporators in inner side of the thin film compartment given in Figure 2.12c.

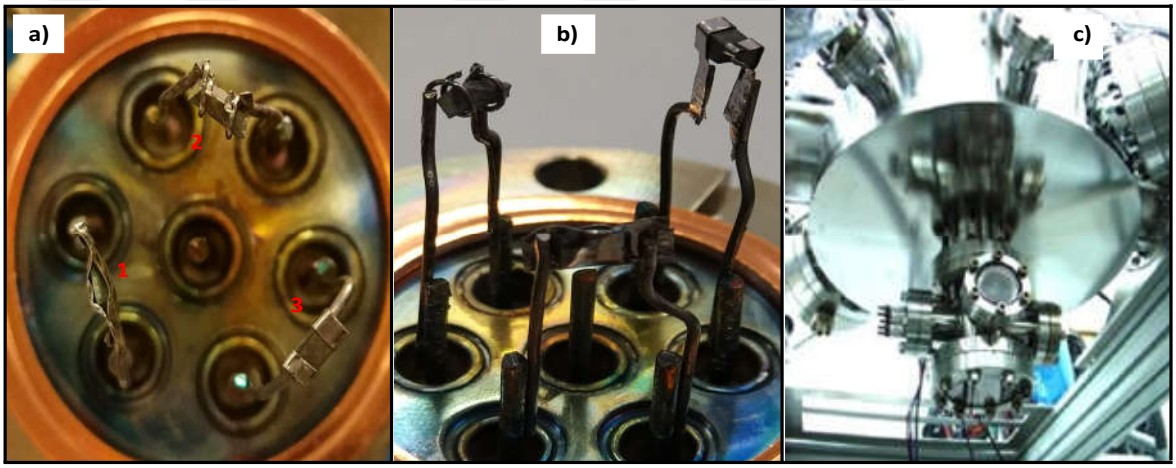

Figure 2.12 (a) Top-view of custom-made evaporators. It should be noted that different Mn-evaporators are labelled as 1, 2, and 3; (b) Side-view of the custom-made Mn evaporators. (c) Thin film doser compartment of the UHV setup.

In the current work (Chapter 4), evaporator 1 was used since other designs suffered from unstable Mn deposition rates. Mn-evaporator 1 was heated by a DC power supply (Maksimel Elektronik, 30 W DC Power Supply) by applying a power of 18 W to the evaporator A (V = 1.5 V, I = 12 A). Since Mn evaporator was not equipped with a shutter, Pd(111) sample was transferred to the thin film doser compartment after evaporator 1 was heated for 12-15 mins at 12 A in order to warm the Mn source up.

The XPS analysis discussed in Section 4.1 revealed that, when evaporator 1 is warmed up, it had a deposition rate of 1.5 ML/min if the dosing parameters that are described above are used. In other words, this custom-made evaporator is roughly capable of forming 2-3 nanometers (nm) thick Mn thin films on Pd(111) surface per minute (after evaporator is warmed up for 12-15 mins) in vacuum at RT when 18 W power is applied.

CHAPTER 3

Effects of Brønsted Bases on Formic Acid Dehydrogenation Selectivity of Pd(111) Single Crystal Model Catalyst

This Chapter is reprinted (adapted) with permission from (Karakurt, B., Koçak, Y. and Ozensoy, E. Enhancement of Formic Acid Dehydrogenation Selectivity of Pd(111) Single Crystal Model Catalyst Surface via Brønsted Bases. The Journal of Physical Chemistry C, 2019, 123,47, pp 228777 - 22788). Copyright (2019) American Chemical Society.

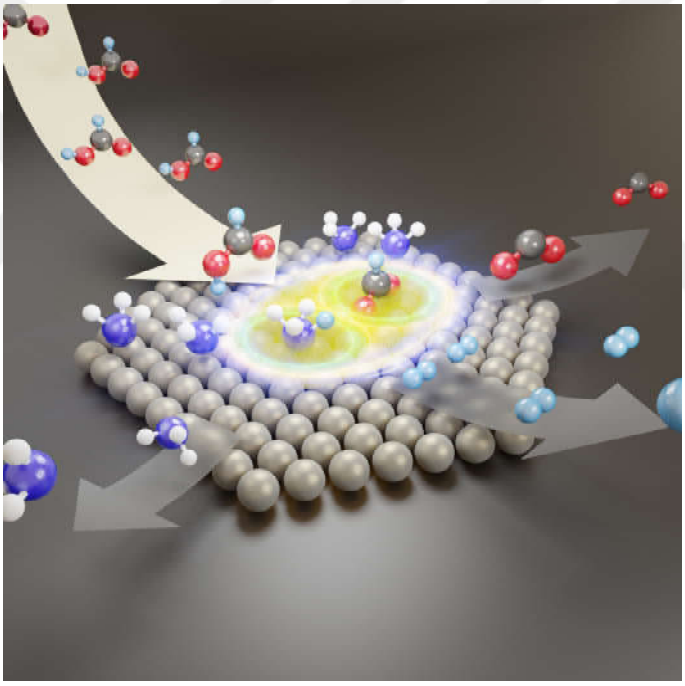

Figure 3.1. Schematic illustration of the enhancement in FA dehydrogenation over Pd(111) single crystal model catalyst surface upon NH_3 functionalization [8].

3.1 Ammonia (NH_3) Adsorption on Pd(111)

Ammonia TPD profiles were obtained by dosing different exposures of NH_3 (g) (Linde AG, purity ≥ 99.995%) onto the clean Pd(111) surface at 90 K (see Figure 3.3). It should be noted that, during NH_3-TPD, some of the other possible decomposition products such as *m/z* = 2 (H_2) and *m/z* = 28 (N_2) were also recorded along with *m/z* = 17 (NH_3) desorption channel and these desorption channels are represented in Figure 3.2.

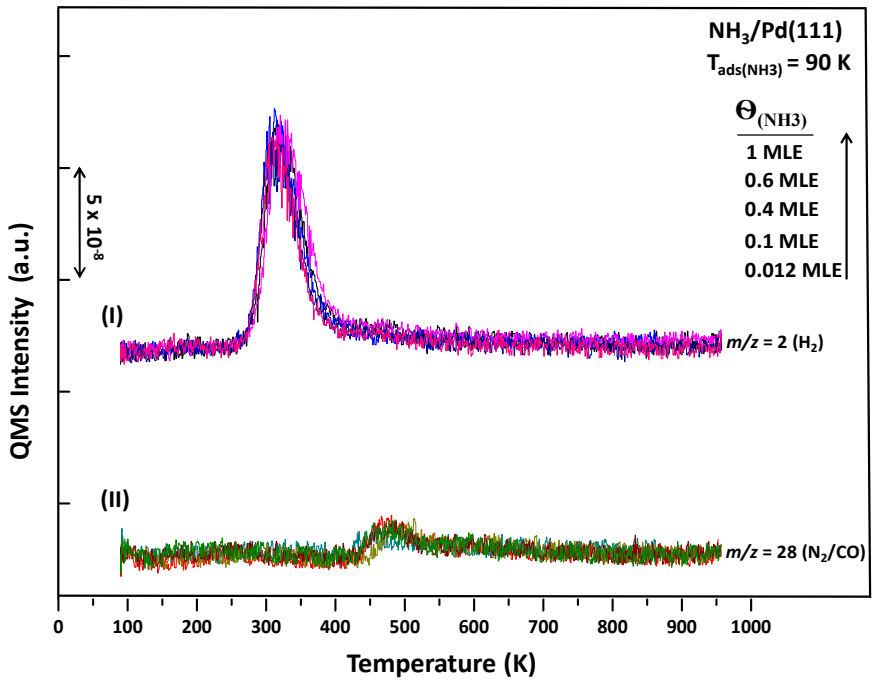

Figure 3.2. *m/z* = 2 (H_2) and *m/z* = 28 (N_2) TPD profiles that were obtained after NH_3 adsorption on clean Pd(111) at 90 K as a function of increasing NH_3 coverage.

In Figure 3.2, the set of TPD profiles grouped as *(I)* consists of five *m/z* = 2 (H_2) TPD profiles and each of these profiles were obtained at different NH_3 coverages. On the other hand, the set of TPD profiles grouped as *(II)* contains five different *m/z* = 28 (N_2/CO) TPD profiles that were simultaneously obtained with *m/z* = 2 (H_2) TPD profiles given in Graph *(I)*. As can be seen from Figure 3.2, peak positions and peak intensities of both *m/z* = 28 (N_2/CO) and *m/z*

= 2 (H_2) TPD profiles stayed constant as a function of increasing NH_3 coverage. Moreover, it should also be pointed that the peak positions and intensities of TPD profiles present in *(II)* are quite similar to the *m/z* = 28 (CO) TPD profile obtained from the clean Pd(111) surface (Figure 2.8b). Therefore, *m/z* = 28 TPD profile that is shown in Figure 3.2 was attributed to the background carbon monoxide instead of N_2. As a result, it was concluded that, within the detection limits of the used QMS, NH_3 adsorbed and desorbed from the clean Pd(111) surface in a molecular fashion reversibly without dissociating.

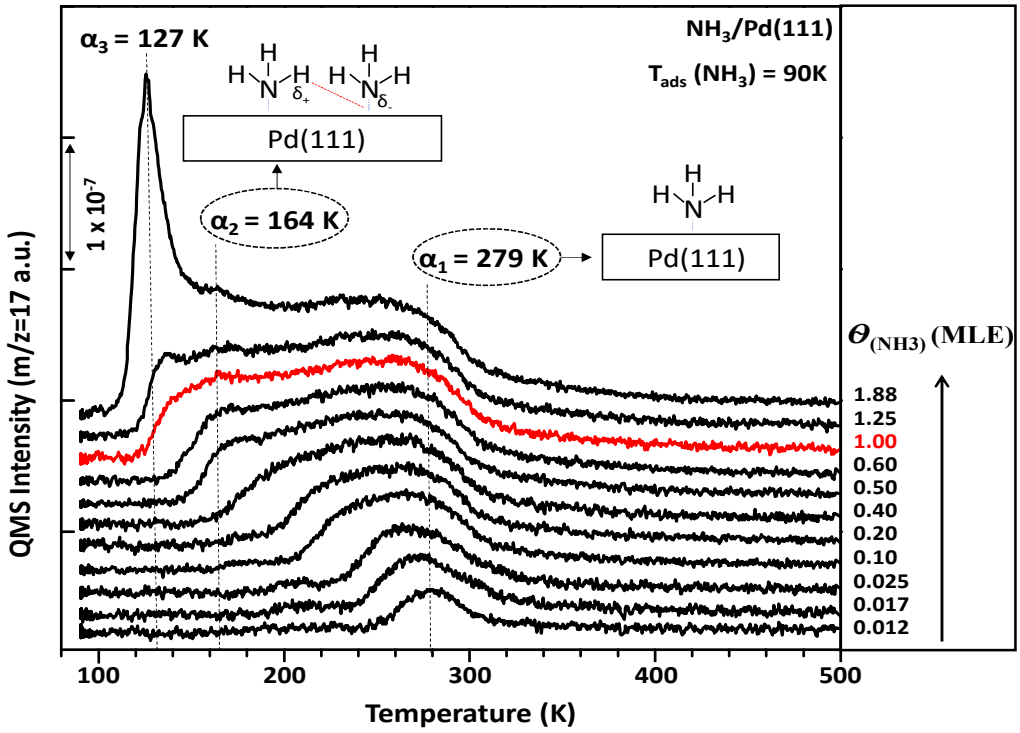

Figure 3.3. TPD profiles (*m/z* = 17) obtained after adsorption of NH_3 at 90 K on clean Pd(111) as a function of increasing ammonia coverage.

NH_3-TPD profiles given in Figure 3.3 suggest that NH_3 yields three main desorption states on the clean Pd(111) single crystal surface. The first state is the low-coverage α_1 state and this state has a desorption maximum located at 279 K. As can be seen from Figure 3.3, with increasing NH_3 coverage, α_1 state starts to broaden towards lower temperatures. As a result

of this broadening, the second sub-monolayer desorption state which is denoted as α_2 starts to form *ca.* 0.6 MLE and this state reaches its desorption maximum around 164 K. A further increase in θ_{NH3}, leads to the formation of the α_3 desorption state at 127 K. In general, the features of the NH_3-TPD profiles obtained from the clean Pd(111) surface given in Figure 3.3 are in accordance with the TPD data obtained from other face centered cubic (FCC) single crystal metal surfaces such as Rh(111) [83], Au(111) [84], Pt(111) [85], Ag(111) [86], Ni(111) [87], and Ru (0001) [88]. The broadening of the NH_3-TPD signals in Figure 3.3 towards low temperatures can be attributed to the repulsive interactions between the NH_3 adsorbates and as well as existence of dissimilar adsorption sites and adsorption states. These observations are in accordance with the DFT study of Salli *et al.* which proposes the presence of multiple ammonia adsorption states on the FCC (111) transition metal surfaces and predicts the presence of repulsive intermolecular interactions between NH_3 molecules during the monolayer formation [89]. In Figure 3.3, α_1 desorption state can be associated with the chemisorbed NH_3 species on the Pd(111) surface, since it has been reported that, at low coverages, NH_3 coordinates strongly to the metal surfaces predominantly from its nitrogen lone pair electrons [83-86]. The second sub-monolayer desorption state (α_2) that is observed at relatively higher coverage values in Figure 3.3 was also reported by Fisher *et al.* on the Pt(111) surface [85] and was associated with hydrogen-bonded chemisorbed NH_3 species, which were less tightly bound to the Pt(111) surface. Consequently, the lower-temperature α_2 desorption state on Pd(111) was assigned to ammonia species that are more weakly interacting with the Pd(111) surface as a result of the H-bonding between the chemisorbed NH_3 species. Lastly, α_3 desorption state can be attributed to the presence of multilayer-ammonia species which are a part of a stronger H-bonding network within the ammonia overlayer and interact much weaker with the Pd(111) surface due to the presence of the underlying NH_3 monolayer. TPD profiles given in Figure 3.3 can also be used to quantify the ammonia coverages on the Pd(111) surface. In the literature, the saturation of the α_2 desorption state was considered as a sign of saturation of first adsorption overlayer

[83, 85]. Therefore, in the current work, the integrated desorption signal of the red curve present in Figure 3.3 was assigned to 1 monolayer equivalent (MLE) coverage, since this curve contains saturated α_1 and α_2 states without a significant contribution from the α_3 multilayer desorption state.

3.2 DCOOD Adsorption on Pd(111)

TPD profiles given in Figure 3.4 were obtained by dosing DCOOD with an exposure (ε) of 2×10^{-2} L (1 Langmuir = 10^{-6} Torr.s^{-1}) on clean Pd(111) surface at 123 K. DCOOD exposure was intentionally kept at a relatively low value in order to minimalize the potential interference from water species (which are present as an impurity in the FA source) on FA decomposition selectivity, since it has been reported that water can react with adsorbed CO species and regenerate Pd active sites blocked by CO [90].

Figure 3.4 contains *m/z* = 4 (D_2), 30 (DCO) and 48 (DCOOD) desorption signals which are in line with the adsorption of DCOOD species, while the presence of *m/z* = 2 (H_2) and 3 (DH) signals indicates the existence of singly-deuterated (DCOOH, HCOOD) or non-deuterated FA (HCOOH) impurities in the DCOOD feedstock and/or H-exchange of DCOOD with the background H_2/H_2O species present on the Pd(111) surface. Moreover, the inset given in Figure 3.4b underlines the desorption of a minor amount of H_2 (*m/z* = 2) in the blank TPD of a clean Pd(111) surface, revealing the existence of a small but detectable amount of background hydrogen adsorption. It should be emphasized that *m/z* = 46 signal cannot be solely associated with DCOO- species since it might have contributions from the molecular HCOOH desorption as well.

The desorption signals observed in Figure 3.4 can be grouped to four major thermal windows centered around 165, 190, 325 and 485 K. The simultaneous desorption observed in the monitored QMS channels at 165 K can be mostly attributed to DCOOD catemers, *i.e.* oligomeric/polymeric FA units with β-polymer structure, formed on the Pd(111) surface [25]

since observed mass spectroscopic fragmentation features of these signals are similar to the analogous catemeric species observed for formic acid on Rh(111) [32] and Pd(100) [27]. On the other hand, *m/z* = 20 (D_2O) desorption signal desorbing around 170 K can also have contributions from sub-monolayer desorption of the D_2O impurity coming from the FA feedstock. This argument is in accordance with the typical desorption temperatures (*ca.* 170 K) of sub-monolayer molecular water on Pd(111) [91].

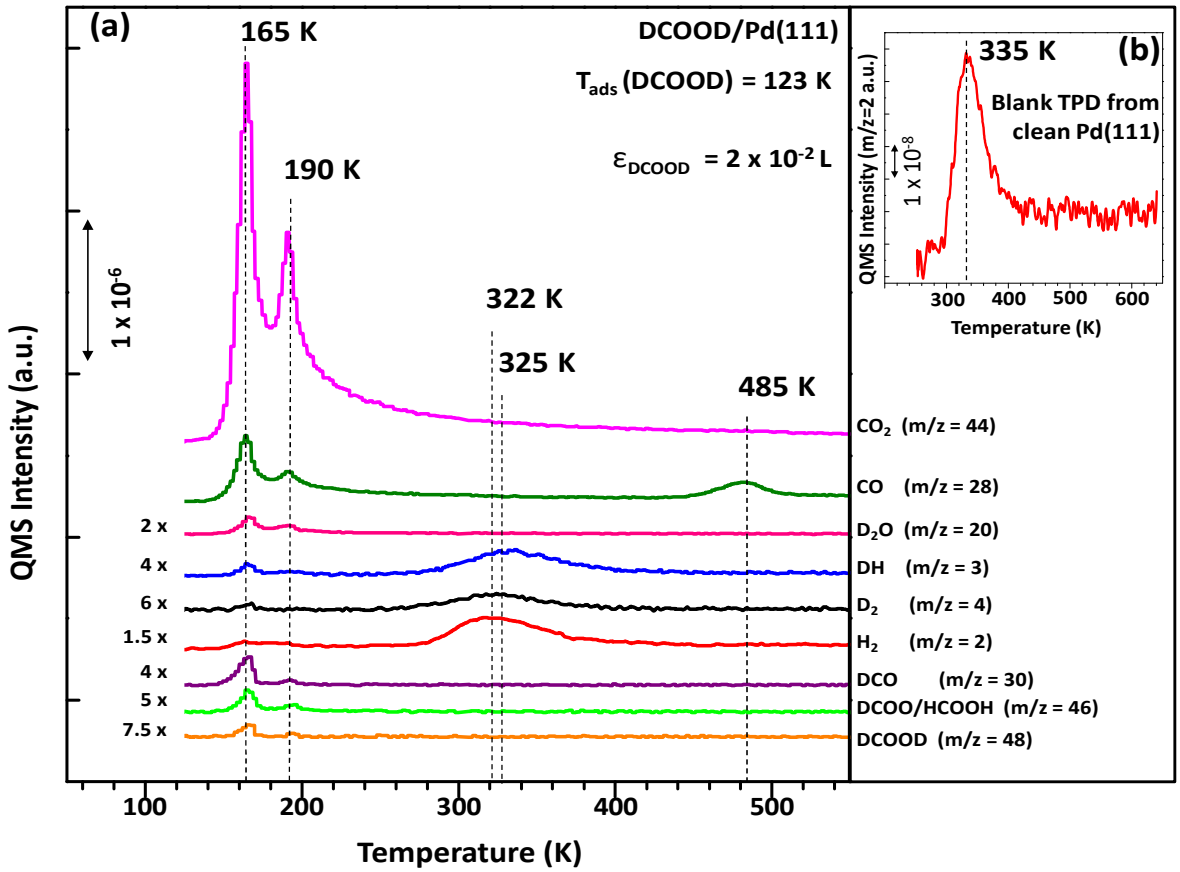

Figure 3.4. (a) TPD profiles of DCOOD adsorption on clean Pd (111) with a DCOOD exposure of $\varepsilon_{(DCOOD)} = 2\times10^{-2}$ L at 123 K. Note that some of the TPD signals are multiplied with the given factors for clarity. (b) *m/z* = 2 desorption channel from a blank (control) TPD experiment on a freshly cleaned Pd(111) surface in the absence of any intentionally added adsorbates.

Overall, desorption features observed at *ca.* 160 K are mainly not due to catalytic FA dehydration/dehydrogenation/decomposition but instead due to mass spectroscopic fragmentation of catameric and/or monomeric FA species.

The second desorption window in Figure 3.4a appears at *ca.* 190 K. Compared to the *m/z* = 30 (DCO), 46 (HCOOH/DCOO) and 48 (DCOOD) signals desorbing in the first window, intensities of these channels at 190 K are considerably lower, indicating a limited extent of FA desorption at 190 K. Besides, absence of any molecular FA desorption features and the presence of intense CO, D_2 and DH desorption signals at temperatures greater than 190 K suggests that FA species are catalytically decomposed into smaller products on the Pd(111) surface at T ≥ 190 K. It should be noted that the catalytic DCOOD decomposition features appearing at 190 K in Figure 3.4a show differences compared to the desorption signals observed for the HCOOH/Pd(111) system studied by Davis *et al.*[25]. The reason for the observation of different HCOOH and DCOOD decomposition temperatures can be linked with the different FA adsorption temperatures (*i.e.* 123 K in the current work *vs.* 170 K in Ref. [25]) and the differences in the linear heating rates. (*i.e.* 1 $K.s^{-1}$ in the current work *vs.* 10 $K.s^{-1}$ in Ref. [25]).

Experimental [25, 32, 33, 35] and theoretical [54-56] studies report that FA forms bidentate bridging formate species on coordinatively saturated late transition metal surfaces, including Pd(111). Therefore, the presence of *m/z* = 44 (CO_2) signal at 190 K may suggest that Pd(111) surface can decarboxylate the formate intermediate and it is capable of dehydrogenating the FA (see Figure 3.5.). As will be discussed in detail in the forthcoming sections, CO_2 desorption at 190 K is also accompanied by *m/z* = 4 (D_2), 3 (DH), and 2 (H_2) desorption, which are the signals belonging to remaining products of dehydrogenation [25]. However, *m/z* = 20 (D_2O) signal present at around 190 K in Figure 3.4a can be linked to dehydration accompanying the dehydrogenation process. Presence of this signal suggests that

Pd(111) is not totally selective towards dehydrogenation. Accordingly, it should be noted that the *m/z* = 28 (CO) signal at ≤ 190 K can be attributed to the mass spectroscopic fragmentation of CO_2 (inside the QMS) instead of CO(g) that is formed as a result of dehydration since, *i)* line shapes of the corresponding *m/z* = 44 and 28 signals show close resemblance, *ii)* desorption of CO from Pd(111) surface at sub-monolayer coverages occurs at significantly higher temperatures (*ca.* 470 - 500 K) due to the strong synergistic effect between CO and Pd(111) surface [15-18].

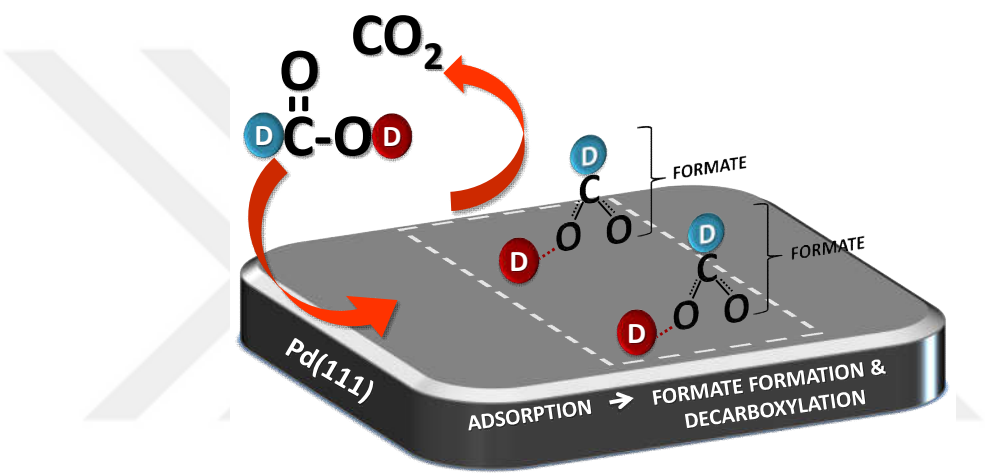

Figure 3.5. Schematic representation of formation and decarboxylation of bidentate formate species on Pd(111) surface. Note that this illustration does not account for the actual stoichiometry of formate formation from FA.

The third thermal window in Figure 3.4a is located at *ca.* 325 K. In order to investigate the origin of the *m/z* = 2 (H_2) signal desorbing at 322 K in Figure 3.4a, hydrogen desorption signal obtained from the clean Pd(111) surface (given in Figure 3.4b) was used as a control experiment. The inset given in Figure 3.4b shows that background H_2 adsorption on clean Pd(111) leads to a H_2 desorption signal at 335 K with a distinct high-temperature desorption tail elongating towards higher temperatures (most likely due to recombinative desorption of

subsurface-H species). Differences in H_2 desorption temperatures and the lack of the high-temperature desorption tail in the *m/z* = 2 (H_2) signal given in Figure 3.4a indicates that origin of this signal is most likely not the background hydrogen adsorption. Moreover, considering the difference in the scale bars of the TPD plots given Figure 3.4a and 3.4b, it is clear that magnitude of H_2 desorption in the DCOOD/Pd(111) TPD data is greater than that of the clean Pd(111) surface. As a result, *m/z* = 2 (H_2) signal in Figure 3.4a located in the close proximity of the *m/z* = 3 (DH) and 4 (D_2) signals was also classified as a FA dehydrogenation product, along with DH and D_2 species.

The fourth and last temperature window in Figure 3.4a is positioned at *ca.* 485 K and it consists of a strong *m/z* = 28 (CO) desorption signal whose desorption maximum is consonant with the literature [25]. Absence of any *m/z* = 44 (CO_2) desorption signal at this temperature window suggests that the origin of this desorption signal is molecular CO, which is formed as a result of catalytic FA dehydration.

3.3. DCOOD adsorption on NH_3-functionalized Pd(111)

3.3.1 Behavior of NH_3 in the presence of DCOOD

Figure 3.6 represents how desorption features of ammonia is changing in the co-presence of FA as well as the overall influence of θ_{NH3} on DCOOD decomposition on Pd(111) surface. It should be noted that the experiments that are given in Figures 3.6a, 3.6c and 3.6e were repeated three times and reproducible results were obtained.

Analysis of *m/z* = 17 (NH_3) desorption signals given in Figure 3.6 reveals that, in the co-presence of DCOOD, there are two main ammonia desorption states located at around 160 K and at 232-274 K. The first NH_3 desorption state observed at 160 K in Figures 3.6a-3.6e can be readily attributed to the α_2 state observed in Figure 3.3, which is due to molecular

adsorption/desorption of H-bonded NH_3 species that are weakly bound to the Pd(111) surface. Presence of H-bonding NH_3 species even at these low NH_3 coverages might indicate the disruption of H-bonding network of catemeric DCOOD species by ammonia, similar to reported disruption of H-bonding network of FA catemers by the Lewis basic functional groups generated on Pd(111) surface [25]. Besides, the 5 K negative temperature shift of catemeric FA desorption features (165 K in Figure 3.4a to 160 K in Figure 3.6) observed upon ammonia functionalization also supports the suggested weakening of the H-bonds between the DCOOD catemers and presence of H-bonding interactions between ammonia and DCOOD species. As a result, 160 K *m/z* = 17 signal can be assigned to NH_3 species that are directly interacting with the DCOOD catemers *via* H-bonding. (along with a minor contribution from the background water/OH species present on the Pd(111) surface).

Furthermore, Figure 3.6a reveals that the second *m/z* = 17 desorption feature desorbs at 274 K at θ_{NH3} = 0.1 MLE ammonia coverage and this desorption maximum is in accordance with the desorption temperature of α_1 state observed in Figure 3.3 for strongly-bound chemisorbed NH_3 on Pd(111). It should be emphasized that the intensity of this higher temperature *m/z* = 17 desorption feature significantly increases as a function of increasing NH_3 coverage, meanwhile its desorption maxima shifts from 274 K to 232 K. This observed behavior also shows a significant resemblance to the desorption behavior of sub-monolayer chemisorbed NH_3 species (*i.e.* α_1 state) present in Figure 3.3. As a result, the second *m/z* = 17 feature desorbing at 274K is attributed to the sub-monolayer NH_3 species that are chemisorbed to the Pd(111) surface from their lone pair electrons.

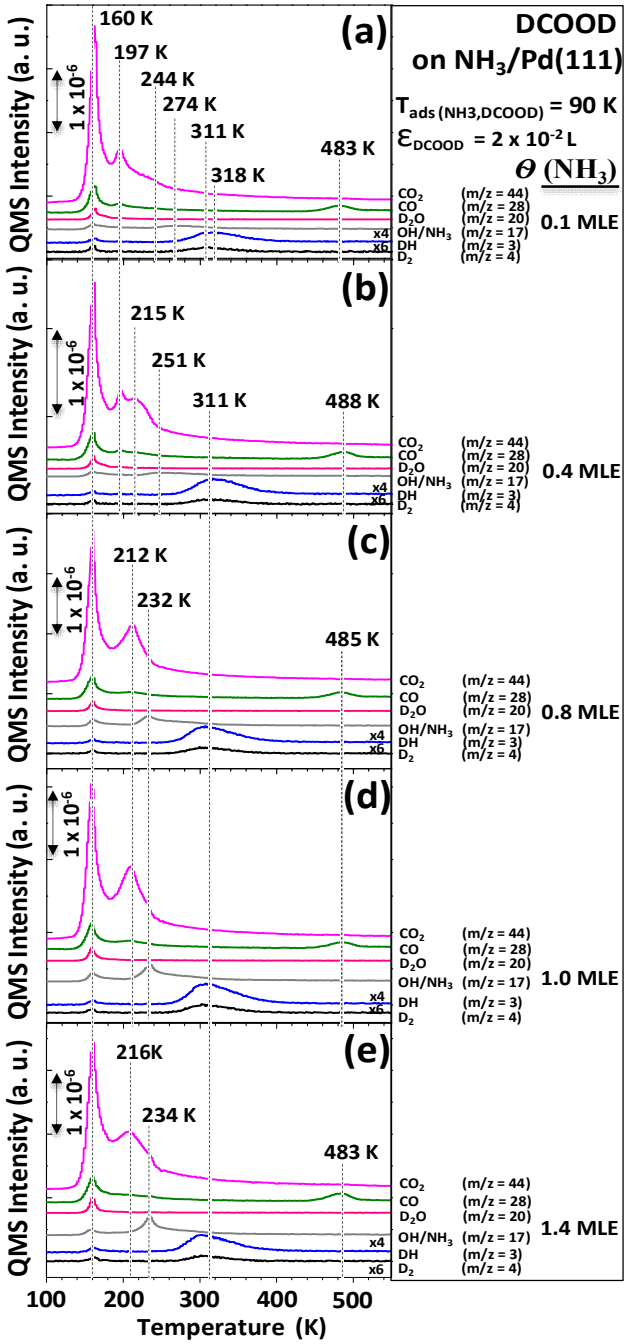

Figure 3.6. TPRS profiles for DCOOD adsorption ($\varepsilon_{(DCOOD)} = 2\times10^{-2}$ L at 90 K) on Pd (111) which was initially exposed to (a) 0.1, (b) 0.4, (c) 0.8, (d), 1.0, (e) 1.4 MLE of NH_3. Note that some signals are multiplied with the given factors for clarity.

3.3.2 Effects of NH_3 on Water (D_2O, DHO and H_2O) Production

As can be seen from Figure 3.7a, TPRS data for θ_{NH3} = 0.1 MLE yields a noticeably smaller *m/z* = 20 (D_2O) signal at 190 K compared to the DCOOD/Pd(111) data given in Figure 3.4a (see black dashed circle and dark red arrow present on Figure 3.7a). This comparison indicates that functionalizing the Pd(111) surface with θ_{NH3} = 0.1 MLE NH_3 suppresses the D_2O formation, *i.e.* hinders the dehydration.

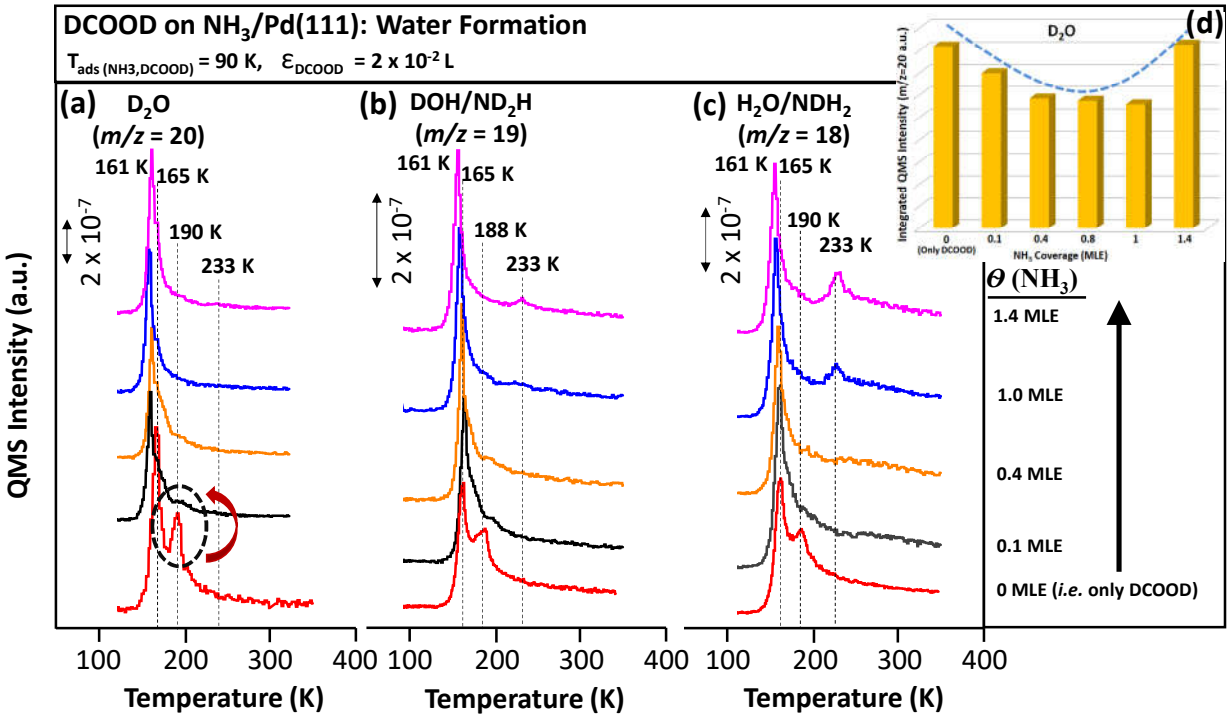

Figure 3.7. TPRS profiles for DCOOD ($\varepsilon_{(DCOOD)} = 2\times10^{-2}$ L at 90 K) adsorption on Pd (111) which was initially exposed to various coverages of NH_3: *m/z* = (a) 20, (b) 19, (c) 18 desorption channels. (d) Corresponding integrated TPRS signal intensities for *m/z* = 20 (D_2O) channel.

The overall influence of ammonia coverage on the suppression of water formation can be seen more clearly in Figures 3.7a-3.7d. It should be noted that Figure 3.7d also reveals the

same trend by making use of the integrated *m/z* = 20 (D_2O) desorption signal intensities corresponding to the given θ_{NH3} values. (See Table 3.1 for a list of the particular integration temperature intervals used in the construction of all of the histograms given in this section). As can be seen from in Figures 3.7b and 3.7c, a quite similar trend is also visible for the desorption behavior of the remaining water species (*i.e.* DOH and H_2O).

Once 1 ML threshold is passed, new *m/z* = 20, 19, 18 desorption features start to become discernible at 233 K for θ_{NH3} = 1.0-1.4 MLE (Figures 3.7a-3.7c). Since the desorption maxima of these features perfectly overlap with the NH_3 desorption maxima observed in Figures 3.6d-3.6e**,** we believe that these new *m/z* = 20, 19, 18 desorption features in Figures 3.7a-3.7c can be associated with ND_3, ND_2H, and NDH_2 species, respectively; as well as other species containing amine functionalities as will be discussed in section 3.3.6.

3.3.3 Effects of NH_3 on CO_2 Production

On the Pd(111) surface, influence of NH_3 on CO_2 formation from FA reveals an opposite behavior compared to the formation of water species. As can be seen from Figures 3.6 and 3.8a, *m/z* = 44 (CO_2) TPRS signals located at *ca.* 190 K (which are due to FA decomposition and catalytic dehydrogenation) become wider and more intense with increasing ammonia coverage, implying a boost in catalytic CO_2 production. Since the production trends of CO_2 (Figure 3.8b) and D_2O (Figure 3.7d) as a function of increasing NH_3 coverage exhibit opposite and complementary behaviors, it can be claimed that NH_3 facilitates FA dehydrogenation and augments hydrogen formation selectivity, while supressing FA dehydration.

As can be seen from Figure 3.8a, even presence of a very low coverage of ammonia (*i.e.* 0.1 MLE) leads to a positive shift (from 190 K to 197 K) in CO_2 desorption temperatures which might be associated with the stabilization of the FA decomposition intermediates by

surface NH_3 species. At higher NH_3 coverages (*i.e.* 0.4 MLE), a new high-temperature CO_2 desorption signal appears *ca.* 216 K, revealing the presence of a different strongly-bound decomposition intermediate (possibly a formate species stabilized by NH_3 species) which is not present in the case of the DCOOD/Pd(111) system (Figure 3.4a). Further analysis of TPRS data given in Figures 3.6a-3.6e also shows that during NH_3-facilitated DCOOD dehydrogenation on Pd(111), various desorbing species (along with their isotopically labeled derivatives) leave the surface in the following order: *i)* water species at around 190 K, *ii)* CO_2 at 197-216 K, *iii)* ammonia species at 232-274 K, *iv)* hydrogen species at 305-360 K, and *v)* CO species at > 485 K.

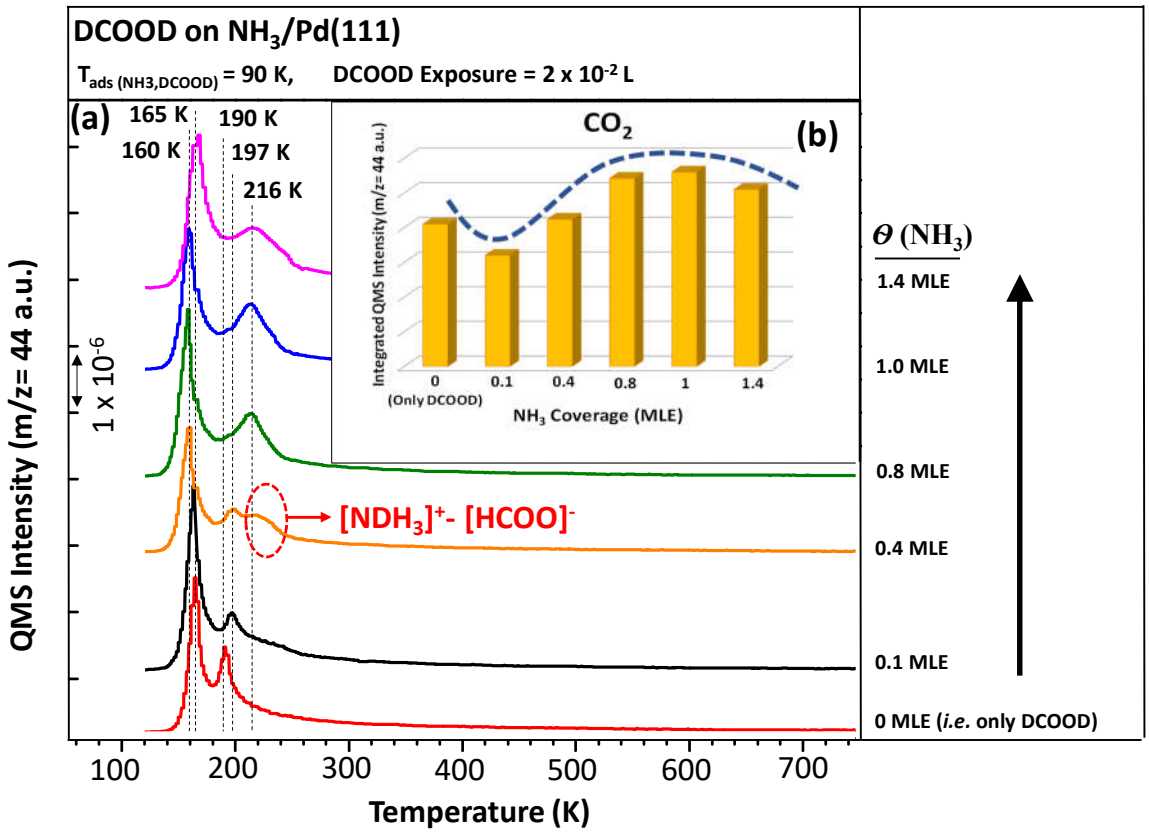

Figure 3.8. (a) TPRS profiles for CO_2 (m/z = 44) production upon DCOOD adsorption ($\varepsilon_{(DCOOD)}$ = 2×10^{-2} L at 90 K) on Pd (111) which was initially exposed to various coverages of NH_3. (b) Corresponding integrated TPRS signal intensities for m/z = 44 channel.

Presence of deuterated analogs of ammonia (indicated by Figure 3.7a-3.7c) along with the broadening of the T ≥ 194 K *m/z* = 46 (DCOO) desorption signal as a function of increasing NH_3 coverage (Figure 3.10) can be considered as a sign for NH_3-assisted DCOOD deprotonation on the Pd(111) surface, since it has been reported that Lewis/Bronsted basic functional groups are capable of deprotonating acidic proton of FA [25, 63]. Consequently, it can be argued that some of the adsorbed NH_3 species on Pd(111) may also exist in a protonated form, such as ammonium cations, during the FA deprotonation process. Therefore, stabilization of the FA decomposition intermediate could be linked to the ammonium formation since ammonium cation can act as a counter ion to stabilize the negatively-charged formate species. As a result, the origin of the CO_2 desorption signal appearing at 197-215 K in Figures 3.6 and 8a can be tentatively attributed to the decomposition of an ammonium-formate ion pair (*i.e.* $[NDH_3]^+$ - $[DCOO]^-$ on Pd(111)).

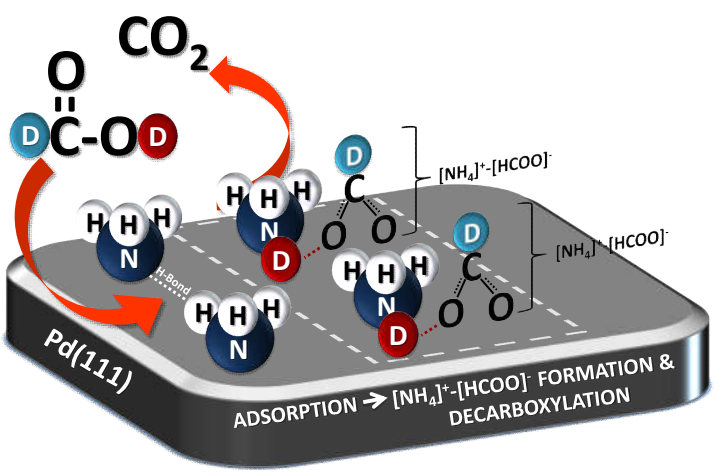

Figure 3.9. Schematic representation of $[NH_4]^+$-$[HCOO]^-$ formation and decarboxylation of ammonium formate on NH_3 functionalized Pd(111) surface. Note that this illustration does not account for the actual reaction stoichiometry.

Former DFT studies reveal the importance of having the right reaction intermediate in order to prompt FA decomposition towards dehydrogenation. Some of these studies predicted that, while the formation of carboxyl (-COOH) intermediate is less favorable compared to the formation of a formate ($HCOO^-$) intermediate on the Pd(111) surface, -COOH also forms on the Pd(111) surface along with formate [55, 92]. Furthermore, it has been shown that -COOH can either undergo dehydration or dehydrogenation, while $HCOO^-$ intermediate predominantly undergoes dehydrogenation on Pd(111) [55]. These computational findings, along with the former UHV studies [25], suggest that D_2O formation is suppressed during the catalytic decomposition of FA on NH_3 functionalized Pd(111) surface because of the stabilization of the formate intermediate.

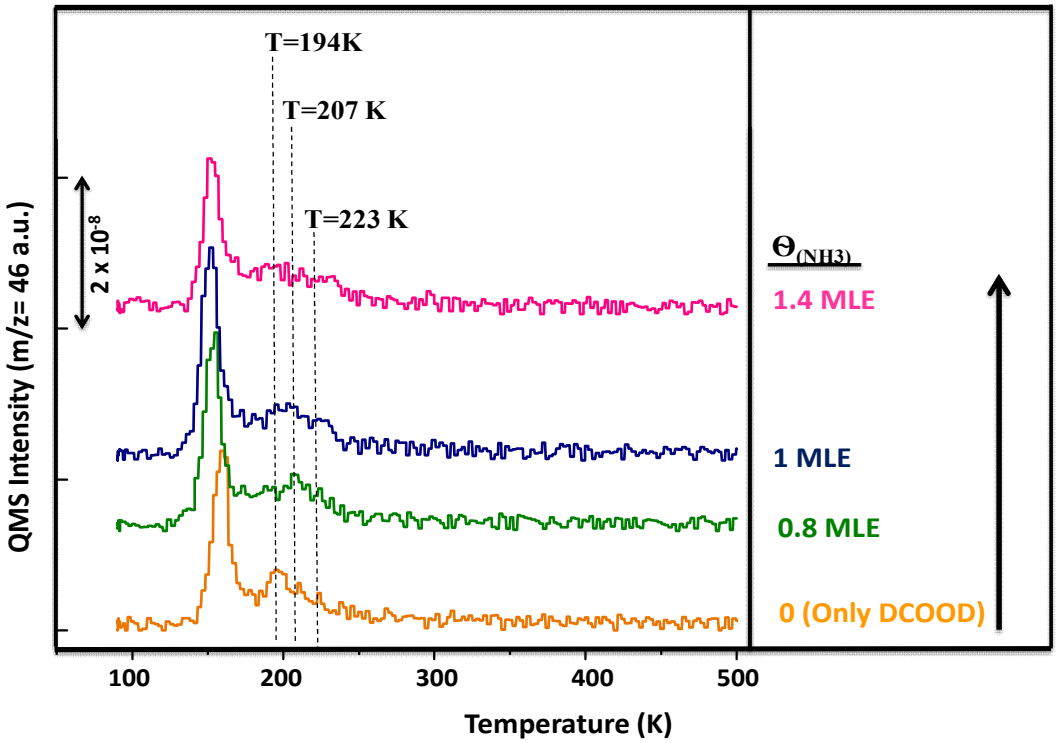

Figure 3.10. TPRS profiles of *m/z* = 46 (DCOO/HCOOH) channel for DCOOD adsorption ($\varepsilon_{(DCOOD)} = 2\times10^{-2}$ L at 90 K) on Pd(111) which was initially exposed to (green) 0.8, (navy) 1, and (pink) 1.4 MLE of NH_3. The orange curve represents the TPD profile obtained from the DCOOD adsorption ($\varepsilon_{(DCOOD)} = 2\times10^{-2}$ L at 123 K) on clean Pd(111).

Figures 3.6-3.8 and 3.11-3.12 show that the increase in FA dehydrogenation selectivity of Pd(111) model catalyst is directly proportional to the NH_3 coverage within 0.1-1.0 MLE range, where exceeding the θ_{NH3} = 1.0 MLE threshold results in weakening of this effect. Most probably, at extremely high NH_3 coverages, NH_3 starts to block active sites on the Pd(111) surface and leads to poisoning.

3.3.4 Effects of NH_3 on D_2 Production

Figures 3.11a and 3.12a reveals that *m/z* = 4 (D_2) desorption signals obtained during FA decomposition on Pd(111) in the presence of NH_3 show a matching pattern with that of the *m/z* =44 (CO_2) desorption channel (Figures 3.8a and 3.8b). In other words, ammonia also enhances D_2 formation up to 1.0 MLE and thus enhances the dehydrogenation and suppresses dehydration. Contrary to the desorption temperature increase observed for CO_2 desorption signals, presence of NH_3 on the Pd(111) surface shifts the D_2 desorption maximum towards lower temperatures (Figure 3.11a). The decrease of D_2 desorption temperature that is observed upon NH_3 functionalization is quite important, since this observation indicates that ammonia both increases hydrogen production selectivity and decreases the activation energy for molecular hydrogen desorption from FA. It should be emphasized that such a favorable case is not generally observed for the interaction of FA with various functionalized Pd surfaces. For instance, similar to NH_3, other co-adsorbates such as Na, K and O are also capable of enhancing the hydrogen formation [25, 27, 28]. However, in these cases, the improvement in the hydrogen formation is obtained in the expense of an increased activation energy of molecular hydrogen desorption.

The effects of θ_{NH3} = 0.1 MLE ammonia functionalization to the D_2 formation reaction rate constant can be crudely estimated by using the basic TPD models that were discussed in section 2.4. Hence, the desorption rate of D_2 from clean Pd(111) surface (3.1) and the

desorption rate of D_2 from θ_{NH3} = 0.1 MLE ammonia functionalized Pd(111) surface (3.2) can be written as:

$$\frac{-\Delta\theta_1}{\Delta T_1} = \frac{k_1}{\beta}\ \theta_1{}^{m_1} \tag{3.1}$$

$$\frac{-\Delta\theta_2}{\Delta T_2} = \frac{k_2}{\beta}\ \theta_2{}^{m_2} \tag{3.2}$$

Where k_1 and k_2 are the rate constants corresponding to D_2 formation conditions defined above. For both cases, it can readily be assumed that the D_2 formation/desorption is recombinative and it is governed by the second order desorption kinetics, *i.e.* $m_1 = m_2 = 2$. It should be kept in mind that Equations 3.1 and 3.2 cannot provide direct information about the rate constants k_1 and k_2 since absolute D_2 coverages are not known for any of these cases. However, dividing Equation 3.1 by Equation 3.2 eliminates the requirement of having a knowledge about the absolute D_2 coverages.

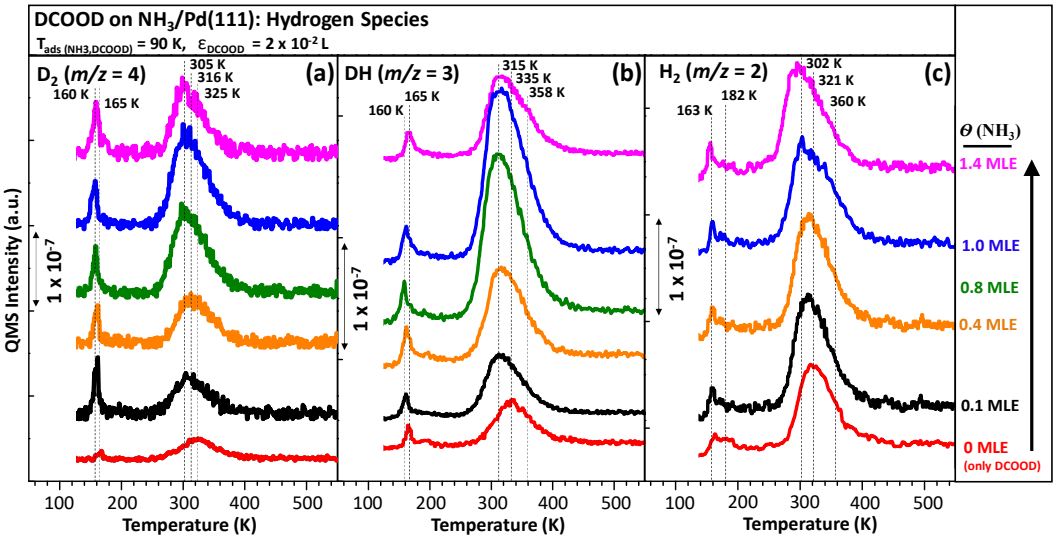

Figure 3.11. TPRS profiles for DCOOD adsorption ($\varepsilon_{(DCOOD)} = 2\times10^{-2}$ L at 90 K) on Pd (111) which was initially exposed to various coverages of NH_3: *m/z* = (a) 4 (D_2), (b) 3 (DH), (c) 2 (H_2) desorption channels.

Consequently, this dividing process allows direct utilization of ratio of the integrated m/z = 4 (D_2) TPRS signals instead of the corresponding ratio of absolute coverages. Besides, it should be kept in mind that in Equations 3.1 and 3.2, $\Delta\theta = \theta$, since initial D_2 coverage is zero in all cases. After these modifications, ratio of rate constants for D_2 desorption on DCOOD/Pd(111) (k_1) and D_2 desorption on NH_3-functionalized DCOOD/Pd(111) (k_2) can be written as the following:

$$\frac{k_1}{k_2} = \frac{\Delta T_2 \theta_2}{\Delta T_1 \theta_1} \tag{3.3}$$

where, ΔT_1 and ΔT_2 are the corresponding temperature differences between the beginning and ending temperatures of the relevant D_2 desorption peaks present in the TPRS data. For example, on the clean Pd(111) surface, D_2 desorption due to DCOOD adsorption takes place between 234 - 532 K, whereas on θ_{NH3} = 0.1 MLE ammonia-functionalized Pd(111) surface, D_2 desorption takes place between 243 - 446 K. Once the required parameters are plugged into equation (3.3), the relative ratio of the rate constants can be calculated as $k_1/k_2 \approx 0.7$. This rough estimation predicts that presence of θ_{NH3} = 0.1 MLE ammonia on Pd(111) surface augments the catalytic D_2 formation rate from DCOOD by 43%.

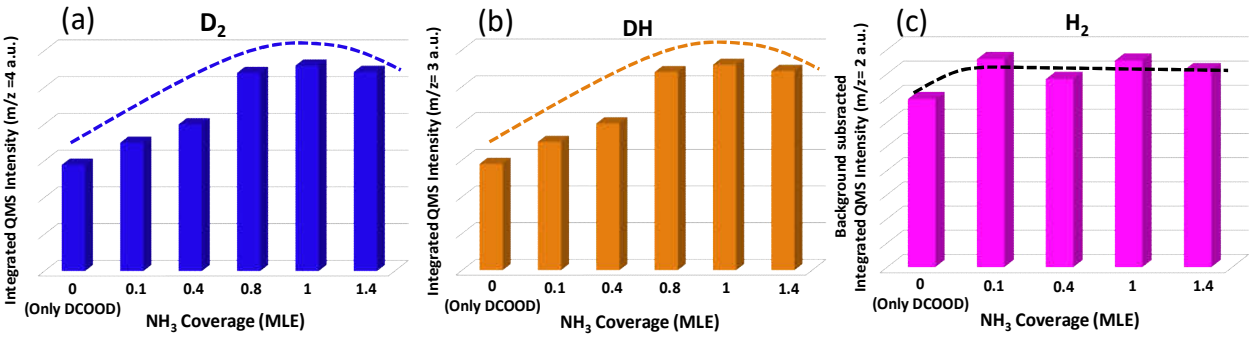

Figure 3.12 Integrated m/z = (a) 4 (D_2), (b) 3 (DH), (c) 2 (H_2) TPRS desorption signals for DCOOD adsorption ($\varepsilon_{(DCOOD)} = 2\times10^{-2}$ L at 90 K) on Pd (111) which was initially exposed to various coverages of NH_3 at 90 K.

In addition, it has been reported that the magnitude of the diffusion barrier of the atomic or molecular species on transition metal single crystal surfaces can be roughly approximated to 12% of the corresponding adsorption energies of such species on the same surface [93]. As can be clearly seen from Figure 3.11a, functionalizing the Pd(111) surface with θ_{NH3} = 0.1 MLE of NH_3 shifts the D_2 desorption maximum from 325 to 311 K, which also corresponds to a decrease in the adsorption energy of D_2 on Pd(111) upon ammonia functionalization; associated with an increase in the surface diffusion rate of atomic D species on Pd(111) surface in the presence of ammonia. As result, it can be also argued that NH_3 also contributes to the FA dehydrogenation by decreasing in D_2 desorption temperature *via* increasing the D atom mobility on the Pd(111) surface along with stabilization of the formate intermediate, where this increase in the mobility can be associated with the facilitated hopping of D atoms *via* hydrogen-bonding network created by the surface NH_3 species or decreased adsorption energy of D atoms on Pd active-sites. Overall effect of ammonia on FA dehydrogenation pathway can be seen at Figure 3.13.

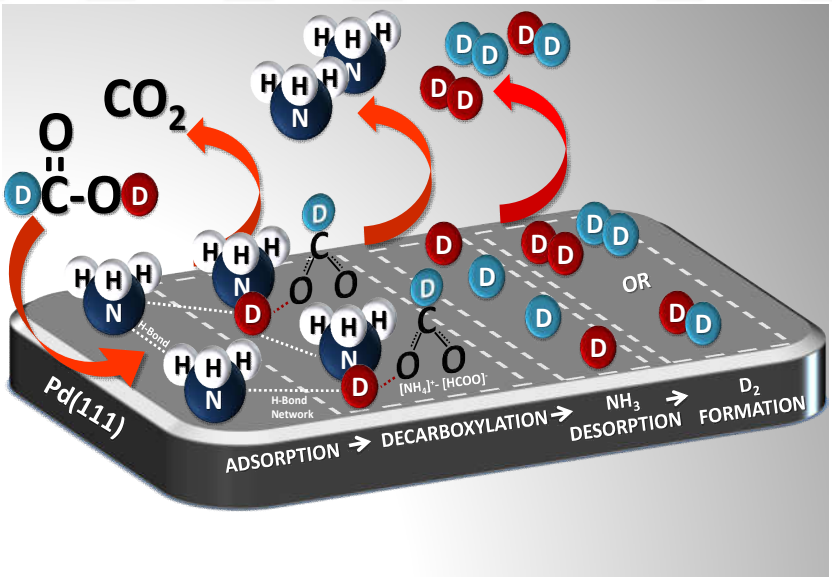

Figure 3.13. Schematic representation of FA dehydrogenation on NH_3 functionalized Pd(111) surface. Note that this illustration does not account for the actual reaction stoichiometry.

3.3.5 Effects of NH_3 on DH and H_2 Production

As can be seen from Figure 3.12b, DH formation follows the same trend with D_2 and CO_2 formation as a function of increasing θ_{NH3} on Pd(111) surface, while integrated TPRS intensities of *m/z* = 2 (H_2) signal represented in Figure 3.12c revels a somewhat dissimilar trend (most likely because of the contributions from background H_2 in the UHV chamber). On clean Pd(111), as a result of FA dehydrogenation, DH desorbs at 335 K, while H_2 desorbs at 322 K (Figure 3.4a). On the other hand, on ammonia-functionalized Pd(111) surface, both DH and H_2 desorb around 315 K (Figure 3.11b,c). The decrease in the desorption maxima of these hydrogen species upon NH_3 functionalization demonstrates the overall favorable effect of ammonia. In accordance with the D_2 formation (Figure 3.11a), desorption temperatures of DH (Figure 3.11b) and H_2 (Figure 3.11c) stays unchanged within 0.1-1.0 MLE range, which suggest that formation of all hydrogen species share similar decomposition intermediates and mechanistic pathways.

3.3.6 Effect of NH_3 on CO Production

Figure 3.14 presents the integrated *m/z*=28 (CO) TPRS signals that are obtained upon decomposition of FA on various NH_3-functionalized Pd(111) surfaces. Since ammonia is shown to suppress the FA dehydration (Figures 3.7a-3.7d), CO formation is expected to be hindered as well. However, as can be seen from the Figure 3.14, formation of CO is not suppressed as a function of increasing ammonia coverage.

In order to explain this unexpected CO formation pattern, data given in Figure 3.15 can be considered. Figure 3.15a shows that adsorption of DCOOD on θ_{NH3} =1.4 MLE functionalized Pd(111) causes formation of additional *m/z* = 16 ($-NH_2$) and *m/z* = 28 (CO) TPRS signals at 205 K along with the desorption of molecular species which are due to non-

catalytic processes occurring *ca*. 160 K. Since sub-monolayer molecular CO desorbs at much higher temperatures from Pd(111) surface, the CO desorption observed at 205 K along with *m/z* = 16 (-NH_2), 43 (-NCO) and 45 (NCH_2O/HCOO) signals desorbing at 205 K can be attributed to presence of adsorbates which contain both amine and carbonyl functional groups. We provisionally assign this species to formamide (*i.e.* NH_2CHO and/or its deuterated analogs). It should be noted that *m/z* = 16 desorption signal cannot be due to methane (CH_4) since it is not an expected product of catalytic FA decomposition that takes place on Pd(111) [25]. As a result, the intense *m/z* = 16 (-NH_2) peak desorbing at 234 K in Figure 3.15a can readily be associated with the desorption of chemisorbed ammonia from the Pd(111) surface.

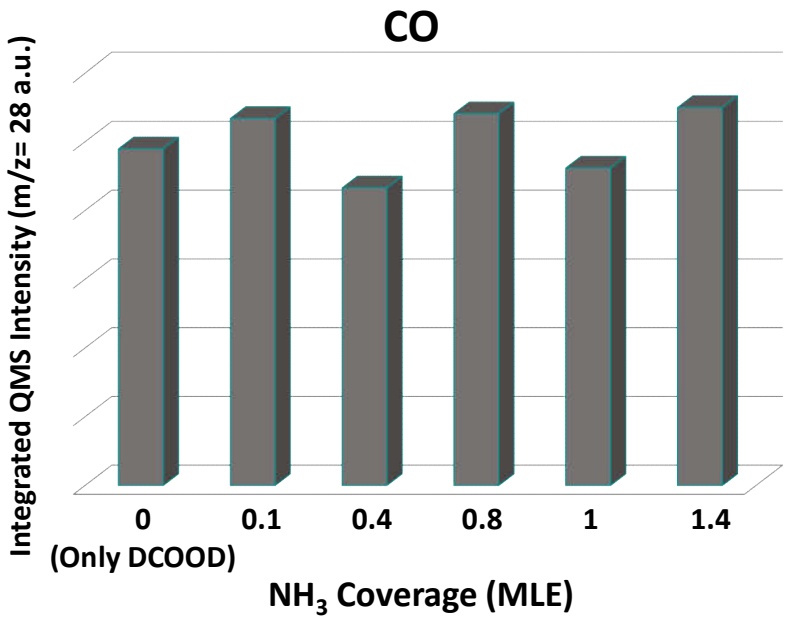

Figure 3.14. Integrated *m/z* = 28 (CO) TPRS desorption signals for DCOOD adsorption ($\varepsilon_{(DCOOD)}$ = 2×10^{-2} L at 90 K) on Pd (111) which was initially exposed to various coverages of NH_3 at 90 K.

Besides, the control experiments given in Figure 3.15b reveal that the *m/z* = 45 signal observed in Figure 3.15a cannot be assigned to deprotonated HCOOH (formyl/formate). As can be seen in the lower *m/z* = 45 desorption profile (*i.e.* red spectrum) in Figure 3.15b, which

was obtained upon adsorption of HCOOH on clean Pd(111) surface, this TPD profile has a totally different desorption maximum (190 *vs.* 205 K), different line shape and dissimilar signal width with respect the corresponding signal that is obtained upon functionalization of Pd(111) surface with 1.4 MLE ammonia (upper spectrum in Figure 3.15b).

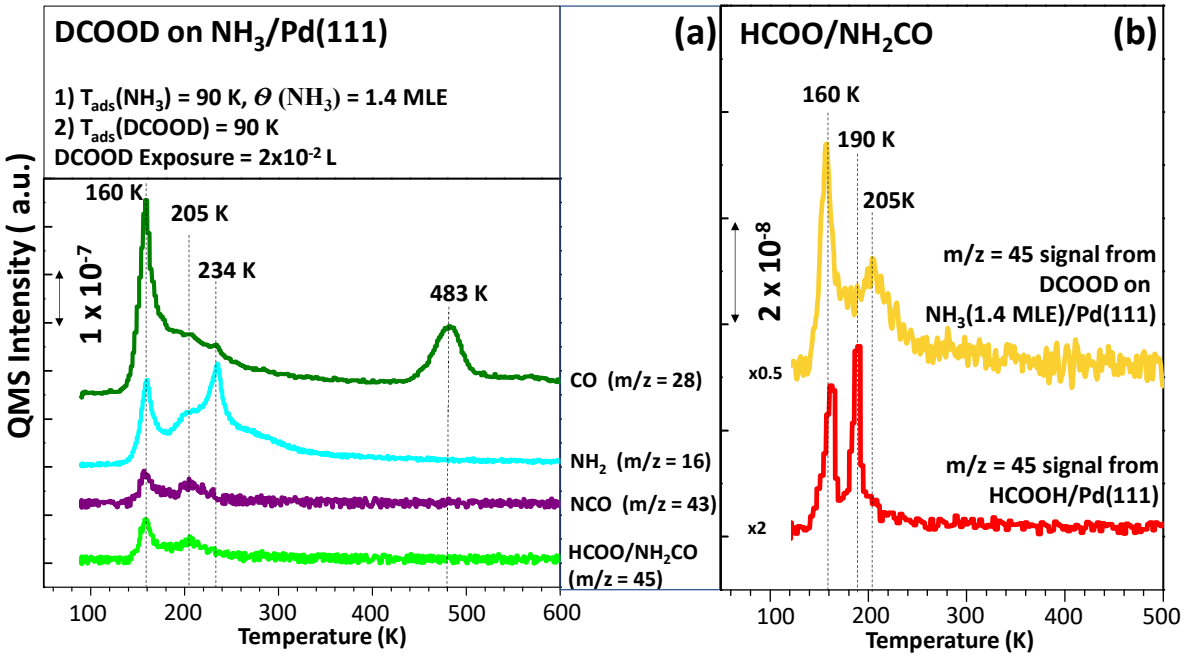

Figure 3.15. (a) DCOOD adsorption ($\varepsilon_{(DCOOD)}$ = 2×10^{-2} L at 90 K) on Pd (111) which was initially exposed to 1.4 MLE of NH_3: *m/z* = 28, 16, 43, 45 desorption channels. (b) Comparison of *m/z* = 45 TPD desorption channels of HCOOH/Pd(111) with the m/z = 45 desorption channel of DCOOD/Pd(111) TPRS in the absence of 1.4 MLE NH_3.

Formation of amide species can also rationalize the unexpected CO production trend observed in Figure 3.14, since amidation products are shown to suppress CO formation [94]. In addition, amidation products could also be held responsible for the initial decrease in CO_2 formation when Pd(111) surface was functionalized with θ_{NH3} = 0.1 MLE (see Figure 3.8b.) Hence, it can be argued that NH_3 functionalization can also prevent CO poisoning of the Pd(111) active sites by inhibiting the CO formation *via* amidation reactions.

		Integration Temperature Intervals of TPD/TPRS Signals					
	TPD/TPRS Signal / Figure Number	m/z = 20 (D_2O) 3.7d	m/z = 44 (CO_2) 3.8b	m/z = 4 (D_2) 3.12a	m/z = 3 (DH) 3.12b	m/z = 2 (H_2) 3.12c	m/z = 28 (CO) 3.4a 3.6a,b,c,d,e
$\Theta_{(NH3)}$	0 - Only DCOOD	142 K – 239 K	182 K – 228 K	234 K – 532 K	253 K – 459 K	236 K – 456 K	436 K – 526 K
	0.1 MLE	141 K – 220 K	186 K – 223 K	243 K – 446 K	248 K – 450 K	230 K – 465 K	440 K – 518 K
	0.4 MLE	139 K – 219 K	185 K – 247 K	243 K – 433 K	240 K – 446 K	229 K – 467 K	444 K – 525 K
	0.8 MLE	-	185 K – 253 K	241 K – 427 K	244 K – 461 K	222 K – 451 K	438 K – 523 K
	1 MLE	138 K – 215 K	190 K – 255 K	237 K – 438 K	241 K – 464 K	206 K – 443 K	435 K – 522 K
	1.4 MLE	135 K – 219 K	196 K – 259 K	238 K- 419 K	236 K – 445 K	209 K – 440 K	434 K – 527 K

Table 3.1 Integration temperature intervals of all integrated TPD/TPRS histograms given in Figures 3.7d, 3.8b, 3.12, 3.14.

CHAPTER 4

Effects of MnO_x Model Lewis Base on Formic Acid Dehydrogenation Selectivity of Pd(111) Single Crystal Model Catalyst

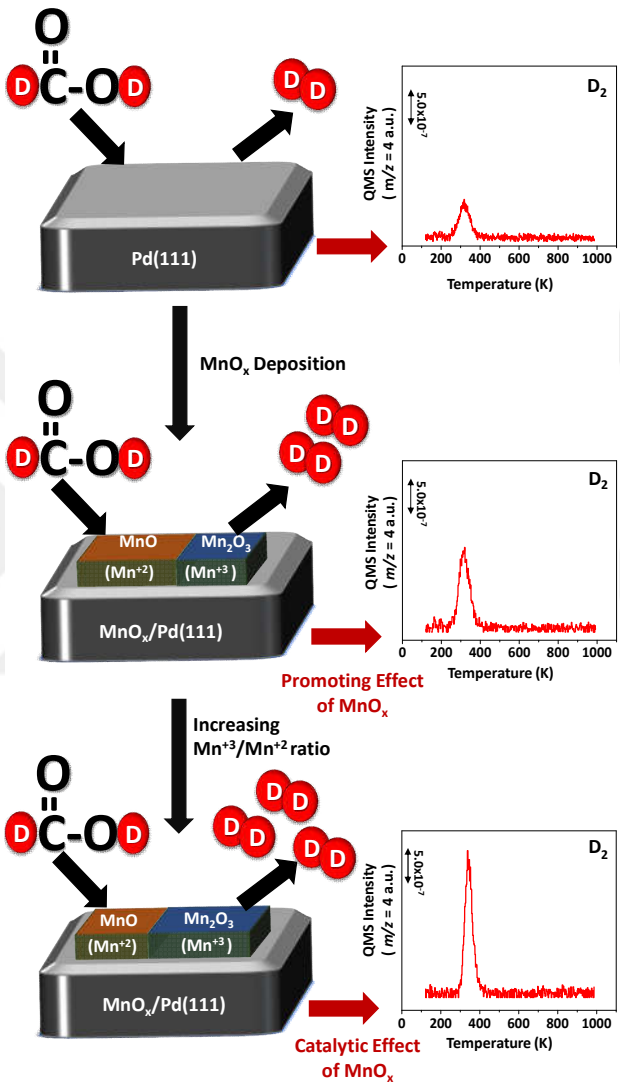

Figure 4.1 Schematic representation of the enhancement of FA dehydrogenation on various MnO_x/Pd(111) model catalyst surfaces. Note that this illustration does not account for the actual reaction stoichiometry.

4.1 Determination of Mn Coverage on Pd(111) Surface

The plot given in Figure 4.2 is used to quantify the amount of Mn that is deposited on the surface in terms of an effective coverage. (Mn $2p_{3/2}$ XPS intensity is normalized with the Pd*3d* XPS signal of the substrate in order to remove the effects of measured XPS intensity fluctuations). This plot indicates that the overlayer grows *via* a basic Stranski-Krastanov growth mode since the apparent initial linear increase is followed by a break to a much less rapid progression [95, 96]. Initially, there is a uniform formation of the first monolayer that is followed by the growth of clusters, with a break point corresponding to the 1 ML of the effective Mn coverage.

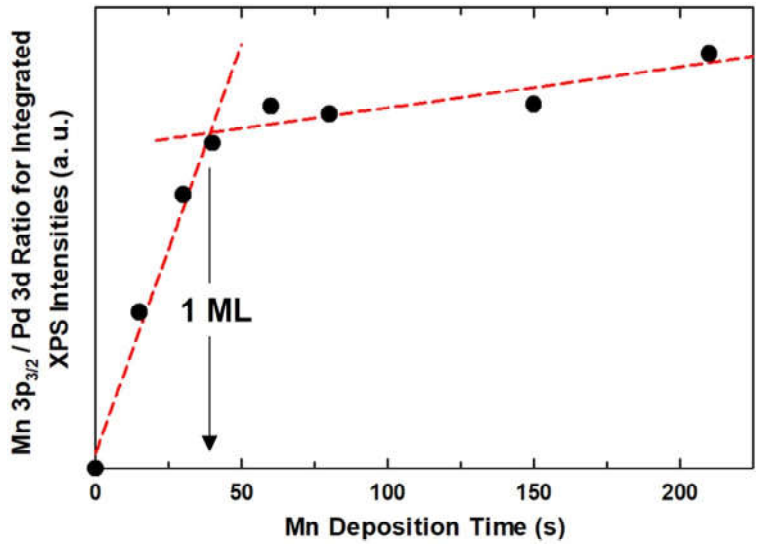

Figure 4.2. Mn $2p_{3/2}$ / Pd*3d* intensity ratio as a function of Mn deposition time.

4.2 Adsorption of DCOOD on Pd(111)

TPD profiles presented in Figure 4.3 were obtained by adsorbing DCOOD with an exposure of $\varepsilon_{DCOOD} = 8\times10^{-3}$ L on clean Pd(111) surface at 123 K. It should be noted that Figure

4.3 is the average of three DCOOD TPDs that are performed under the same conditions indicated above. Based on Figure 3.4, magnitude of FA exposure was optimized in a such way that it allowed us to monitor all desorption features/products clearly (see Figure 4.4) while minimizing the effects of water impurities in the FA feedstock on catalytic decomposition of FA, since water can react with CO to replenish the poisoned Pd active sites [90].

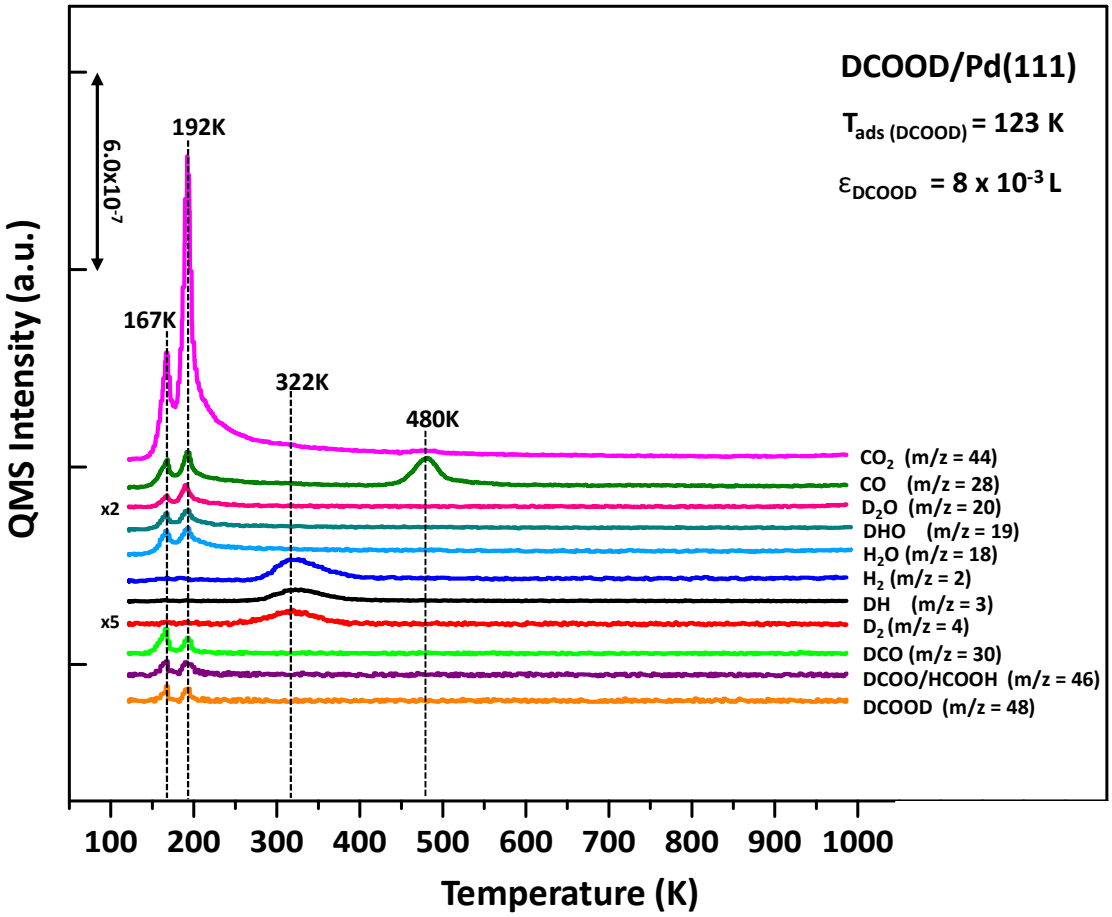

Figure 4.3. TPD profiles of DCOOD adsorption on clean Pd(111). some of the TPD signals are multiplied by the given factors for clarity.

As can be seen from Figure 4.3, peak shapes and desorption maxima of the TPD profiles that are obtained upon adsorption of ε_{DCOOD} = 8×10^{-3} L DCOOD on clean Pd(111) are quite similar to the TPD profiles given in Figure 3.4, where FA exposure was 2×10^{-2} L . The only

difference is observed for catemeric desorption species desorbing at *ca*. 165 K. In Figure 4.3, intensities of all catemeric desorption signals are lower with respect to the catemeric desorption signals observed in Figure 3.4. As a result of these observations, it can be concluded that decreasing DCOOD exposure decreased the catemeric FA formation on Pd(111) surface without affecting the chemistry of catalytic FA decomposition

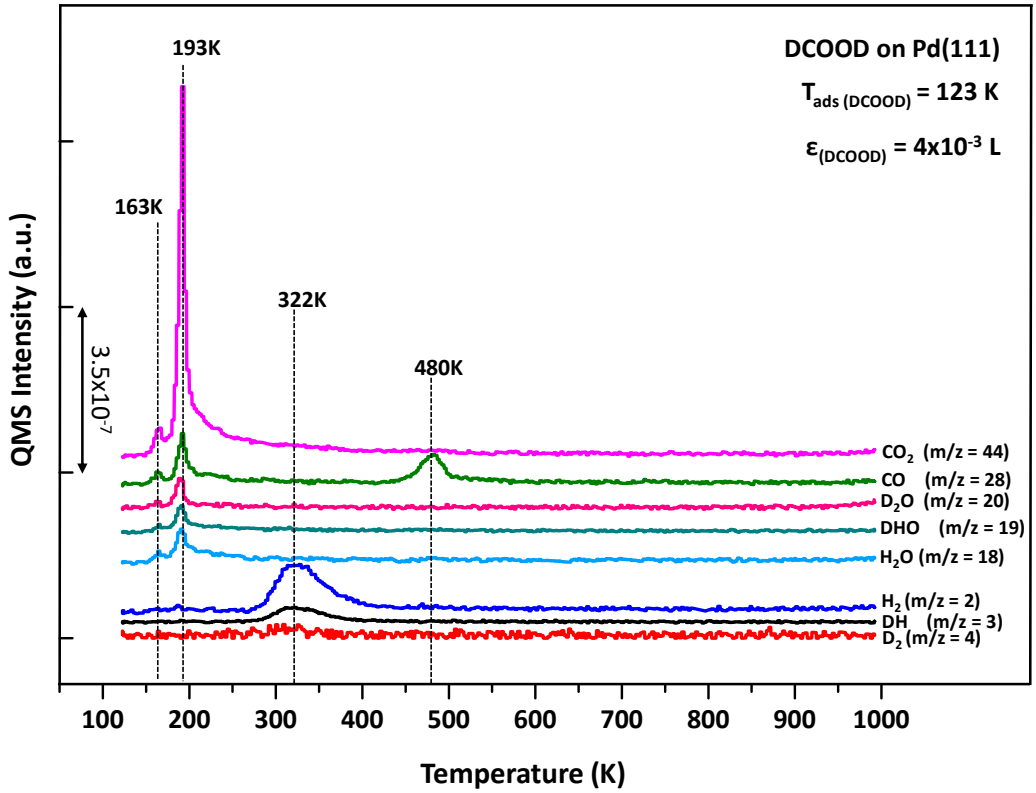

Figure 4.4. TPD profiles obtained upon ε_{DCOOD} = 4×10^{-3} L DCOOD exposure on clean Pd(111) at 123 K. It should be noted that *m/z* = 4 (D_2) desorption signal is not clearly discernible in this low coverage regime.

4.3 Effects of MnO_x on D_2 formation

In order to investigate how MnO_x/Pd(111) surface differs in terms of D_2 generation ability with respect to the clean Pd(111) surface and how D_2 generation evolves after consecutive reaction runs (Figure 4.5a), Mn was deposited on clean Pd(111) prior to FA

exposure. Figure 4.5b gives the Mn $2p_{3/2}$ XPS spectrum that is obtained just after Mn deposition. It should be underlined that MnO_x is a reducible metal oxide that contains both Lewis acidic Mn cations and Lewis basic oxide/O^{-2} ions. However, since Pd $3p_{3/2}$ region (*ca.* 532 eV [97]) overlaps with the O*1s* region of various manganese oxide species (529.5 - 532 eV [81]), Mn $2p_{3/2}$ region was analyzed instead of O*1s* region in order to achieve information about the electronic state of oxide/ O^{-2} ions. In the literature, it is well-known that $2p_{3/2}$ spectrum of manganese metal has a single peak *ca.* 638.8 eV [98-100]. However, in the case of ultra-thin (~1 ML) Mn films grown on d-metal surfaces (including Pd [101]) Mn $2p_{3/2}$ main peak centers around 640 eV and exhibits an intense satellite peak that is separated by ~5 eV, where this satellite peak is observed as a result of delocalization of Mn*3d* electrons over d-metal surfaces [102-104]. Therefore, the peak located at 640.3 eV, along with the intense satellite feature at 645.3 eV, is attributed to Mn^0. Moreover, earlier studies have also showed that main Mn $2p_{3/2}$ XPS peak of ultra-thin Mn films grown on Pd(100) [101] and Ni(110) [102] exhibits an additional 'shoulder' feature located below 640 eV (where this 'shoulder' feature is much more intense in the XPS spectrum given in Figure 4.8 which is obtained from annealed MnO_x). Consequently, the lowest binding energy peak detected at 638.5 eV is also associated with Mn^0. On the other hand, it has been reported that XPS spectrum of manganese oxide ultra-thin films grown on Pd(100) surface show a close resemblance to bulk manganese oxides [101, 105]. Therefore, the peak located at 641.1 eV, along with the intense 'shake-up' peak separated by ~6 eV are assigned to the Mn^{+2} species [106-108], whereas the peak located at 641.9 eV is attributed to the presence of Mn^{+3} species on the surface [109-111]. In summary, the spectrum in Figure 4.5b reveals that deposited Mn has a relatively high metallic character, yet it is already partially oxidized on the surface, where the presence of higher oxidation states are tentatively attributed to the oxidation of Mn by water/hydroxide species adsorbed on the surface upon background pressure spike that occurred during Mn deposition. Consequently, the $m/z = 4$ (D_2) TPD profile corresponding to *Run 1* given in Figure 4.5a was obtained by reacting FA

immediately after Mn deposition without any further treatments. As can be seen from Figure 4.5a, initially, MnO_x/Pd(111) surface yields significantly less D_2 compared to the clean Pd(111) surface. Moreover, *m/z* = 4 (D_2) desorption peaks shift to a slightly higher temperature, whereas this positive temperature shift could be attributed to the hindrance of hydrogen atom mobility due to a presence of MnO_x [8, 93].

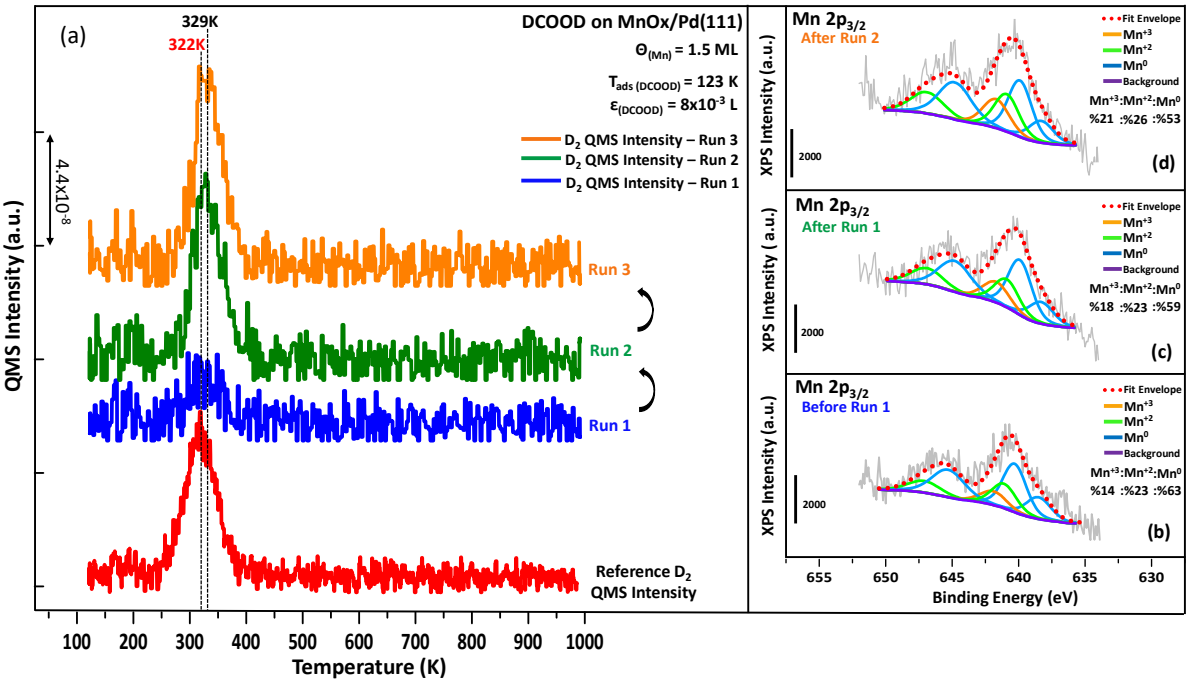

Figure 4.5 (a) Evolution of *m/z* = 4 (D_2) TPD profiles on MnO_x/Pd(111) as a function of reaction runs. Before each run, a fresh DCOOD was introduced at 123 K with a constant exposure of ε (DCOOD) = 8×10^{-3} L. Mn $2p_{3/2}$ XPS spectra obtained (b) before run 1, (c) after run 1, and (d) after run 2.

Importantly and contrary to the first observation, rerunning the reaction under same conditions (*i.e. Run 2*) causes an increase in the D_2 formation and this rise apparently saturates at *Run 3*. This observation, *i.e.* requirement for an induction period for MnO_x to establish its positive influence, is not specific to a particular FA exposure value (which can be seen from comparison of Figures 4.6 and 4.7b). Furthermore, this behavior is also independent of MnO_x

coverage, whereas the difference in the MnO_x coverage only affects the magnitude of D_2 increase, as well as the number of runs it takes for D_2 signal to saturate (see Figure 4.7).

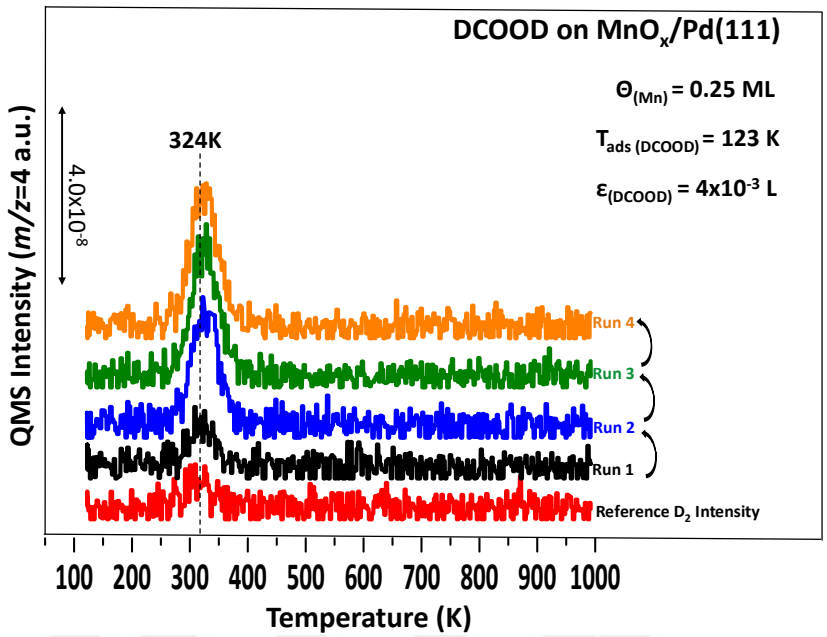

Figure 4.6. Change of *m/z* = 4 (D_2) channel as a function of reaction runs.

Control experiments have also revealed that this phenomenon cannot be solely attributed to the morphology change of MnO_x that might occur during the temperature ramp, since running the same reaction on pre-annealed MnO_x/Pd(111) surface generated a smaller amount of D_2 with respect to clean Pd(111) (see Figure 4.8). Lastly, it should be emphasized that deposition of relatively thick (~15 ML) MnO_x overlayer, entirely covering the Pd(111) surface, completely suppressed D_2 and DH formation while substantially boosting the CO formation (see Figure 4.10). This final observation strongly suggests that MnO_x is not capable of enhancing D_2 formation by its own and Pd sites are also required in order to promote hydrogenation generation from FA. Apparently, this requirement could be satisfied only at near monolayer coverages of MnO_x.

In order to comprehend the observed D_2 generation pattern, we have used the Mn $2p_{3/2}$ XPS spectrum given in Figure 4.5b as a reference and focused on the changes that occurred in

Mn $2p_{3/2}$ XPS spectra after *Run 1* (Figure 4.5c) and *Run 2* (Figure 4.5d) respectively. Figure 4.5c shows that after *Run 1*, MnO_x becomes more oxidized compared to Figure 4.5b. This is somewhat surprising since FA is not a well-known oxidizing agent. Furthermore, oxidation of MnO_x is also accompanied by an increase in overall Mn $2p_{3/2}$ XPS intensity, which could be attributed to the increased wetting of MnO_x upon temperature ramp to 1000 K. Similarly, the XPS spectrum that is obtained after *Run 2*, shown in Figure 4.5d**,** indicates that consecutive reaction with FA leads to further decrease of the metallic character of MnO_x. All of these findings suggest that Pd-MnO_x Lewis acid/base interface does not enhance D_2 formation unless MnO_x has a strong oxidic character. This observation is also in accordance with the hydrogen generation behavior observed for PdAg/MnO_x [59] and PdAu/MnO_x [62] high surface area NP catalysts.

Since findings discussed above indicate that increase of the oxidic character of MnO_x promotes D_2 formation, an additional set of similar experiments were carried out on the MnO_x/Pd(111) surface, which has been further oxidized *via* O_2 exposure at elevated temperatures prior to FA dosing (see Figure 4.9). During pre-oxidation process, firstly, Mn was deposited on Pd(111) in vacuum at RT and then the sample was flash-heated to 1000 K in order to mimic the morphology changes that might occur during the FA-MnO_x/Pd(111) reaction. Then, MnO_x/Pd(111) system was exposed to 4.8×10^{-8} Torr O_2 at 623 K for 20 min (ε_{O2} = 4.8×10^{-5} L) in front of the dedicated O_2 leak vale. The oxidation parameters are optimized according to literature [112-114] in order to prevent formation of Lewis basic chemisorbed oxygen species on Pd(111).

The Mn $2p_{3/2}$ XPS spectrum given in Figure 4.9b suggests that pre-oxidized MnO_x has the lowest metallic character among all studied cases. Furthermore, TPD profiles shown in Figure 4.9a clearly show that further oxidation of MnO_x prior to reaction caused an immediate boost in the D_2 formation. These observations are consonant with the observations discussed

above. It should also be noted that pre-oxidation process shifted the D_2 desorption maxima to higher temperatures (by ~ 20 K). This greater shift is attributed both to the hindrance of hydrogen atom mobility and stronger stabilization of the formate intermediate by pre-oxidized MnO_x. Later in particular can be inferred from the a nearly 100 K positive shift observed for the decarboxylation temperature of FA species once Figure 4.3 and Figure 4.11b are compared.

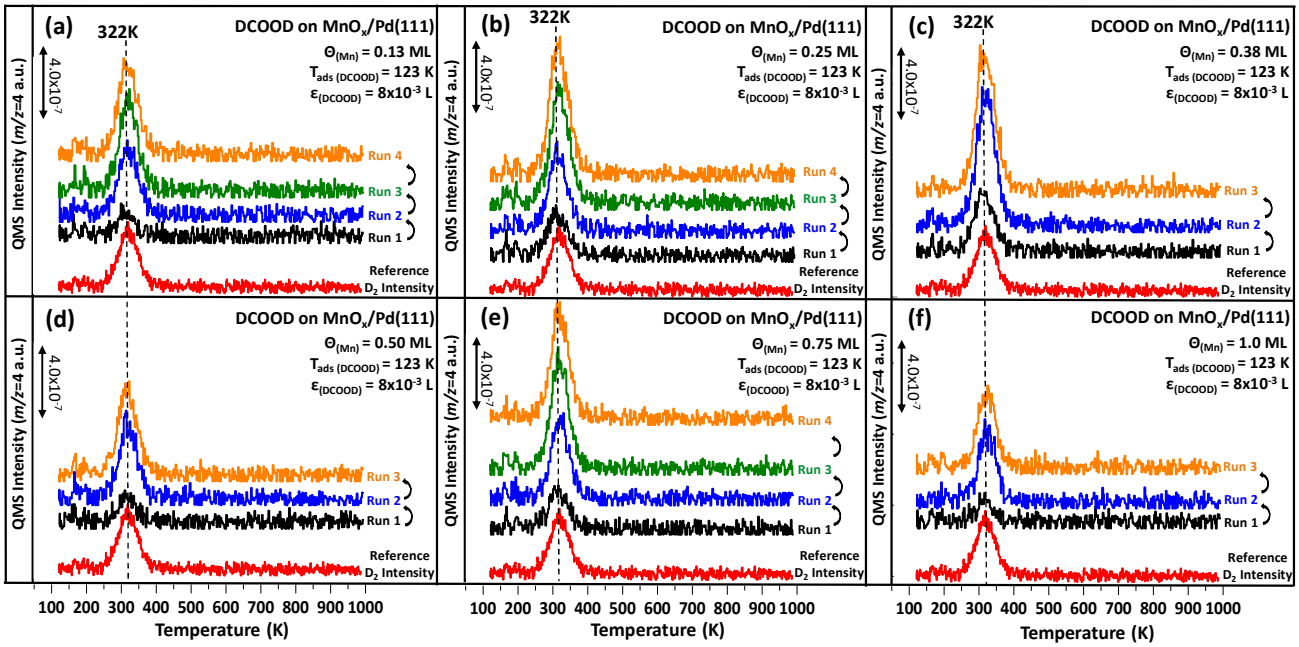

Figure 4.7. Change of m/z = 4 (D_2) desorption signals as a function of reaction runs at various MnO_x coverages.

As can be seen from Figure 4.9a, the reactivity boost is observed only for a single reaction run and it decays upon successive reactions. At the same time, XPS spectra in Figure 4.9c indicates that, before *Run 2* (*i.e.* after the first reaction), metallic character of MnO_x is increased. On the other hand, Figure 4.9d suggests that, within our detection limits, second reaction run caused a negligible change in the oxidation state composition of MnO_x. As a result, it can be argued that the trend observed for XPS spectra given in Figure 4.9 is complementary with the trend given in Figure 4.5. Therefore, this observation also supports the argument which

states that controlling the oxidic character of MnO_x is critical in terms of achieving a higher D_2 generation from FA.

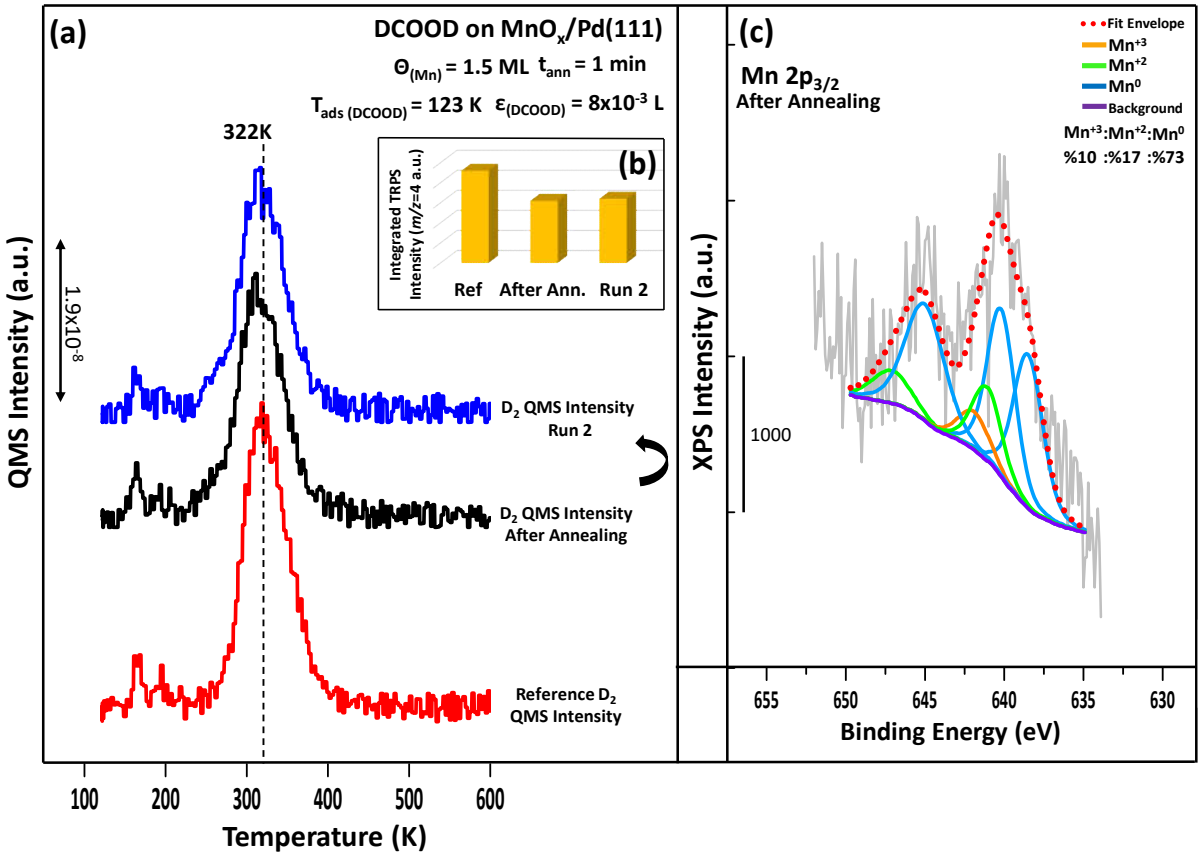

Figure 4.8. (a) Change of m/z = 4 (D_2) desorption signals as a function of reaction runs on pre-annealed MnO_x. Note that red curve belongs to the reference D_2 signal (b) Integrated QMS Intensities of m/z =4 (D_2) signals given in a. (c) Mn $2p_{3/2}$ XPS spectrum of MnO_x after annealing. Note that low binding energy 'shoulder' feature became more intense with increasing metallic character.

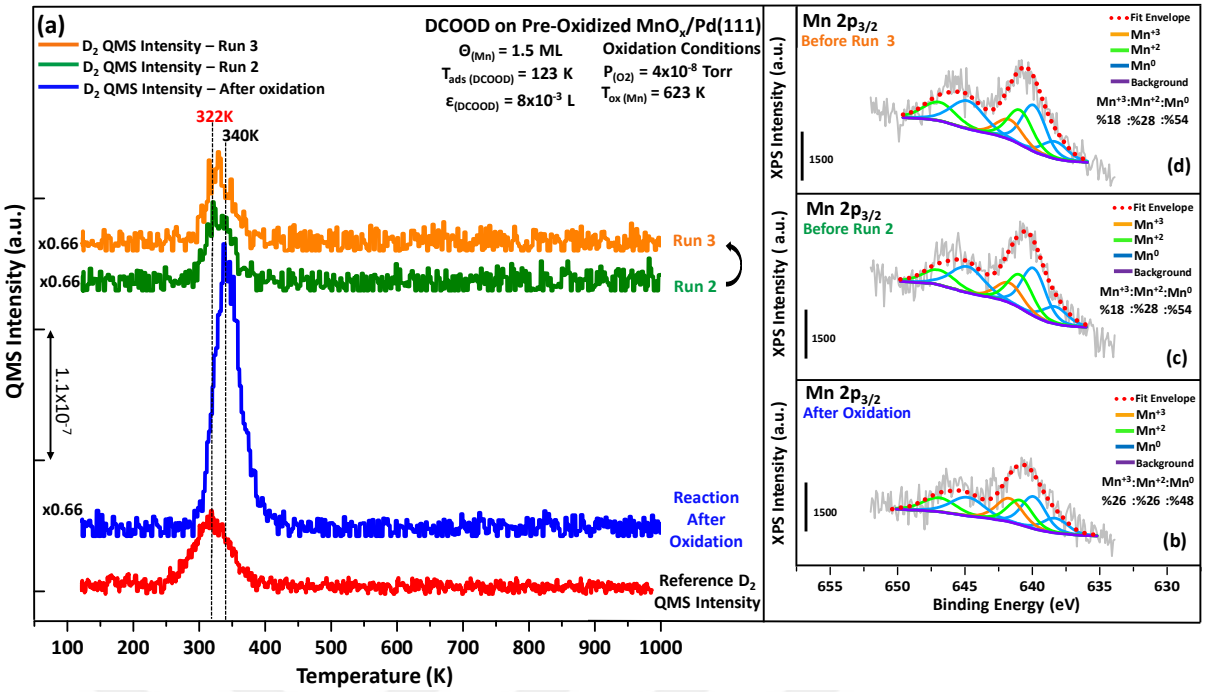

Figure 4.9. (a) Change of *m/z* = 4 (D_2) TPD profiles on pre-oxidized MnO_x/Pd(111) as a function of reaction runs. At each run a fresh DCOOD was adsorbed at 123K with a constant exposure of ε (DCOOD) = 8×10^{-3} L. Some TPRS signals are multiplied with the given factors for clarity. Mn $2p_{3/2}$ XPS spectrum obtained (b) before run 1, (c) after run 1, and (d) after run 2.

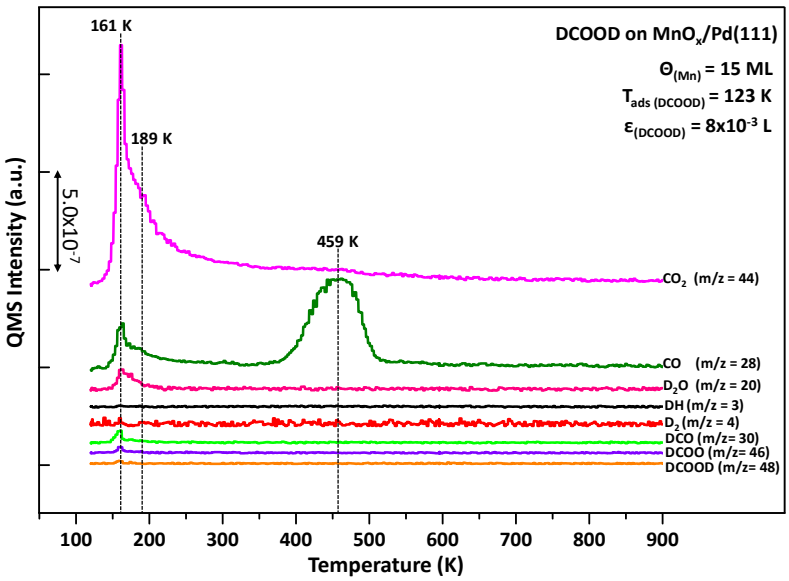

Figure 4.10. TPD Profiles obtained on multilayer MnO_x deposited Pd(111).

4.4 Effects of MnO_x deposition on Formic Acid Decomposition Chemistry

TPD profiles shown in Figures 4.11a and 4.11b give particular examples about how MnO_x/Pd(111) surfaces differ in terms of overall surface chemistry compared to clean Pd(111) surface. Figure 4.11a corresponds to the last of the three successive TPD runs that was obtained after FA adsorption on spent MnO_x (0.25 ML)/Pd(111) surface while TPD profiles in Figure 4.11b were recorded immediately after pre-oxidizing MnO_x (0.25 ML)/Pd(111).

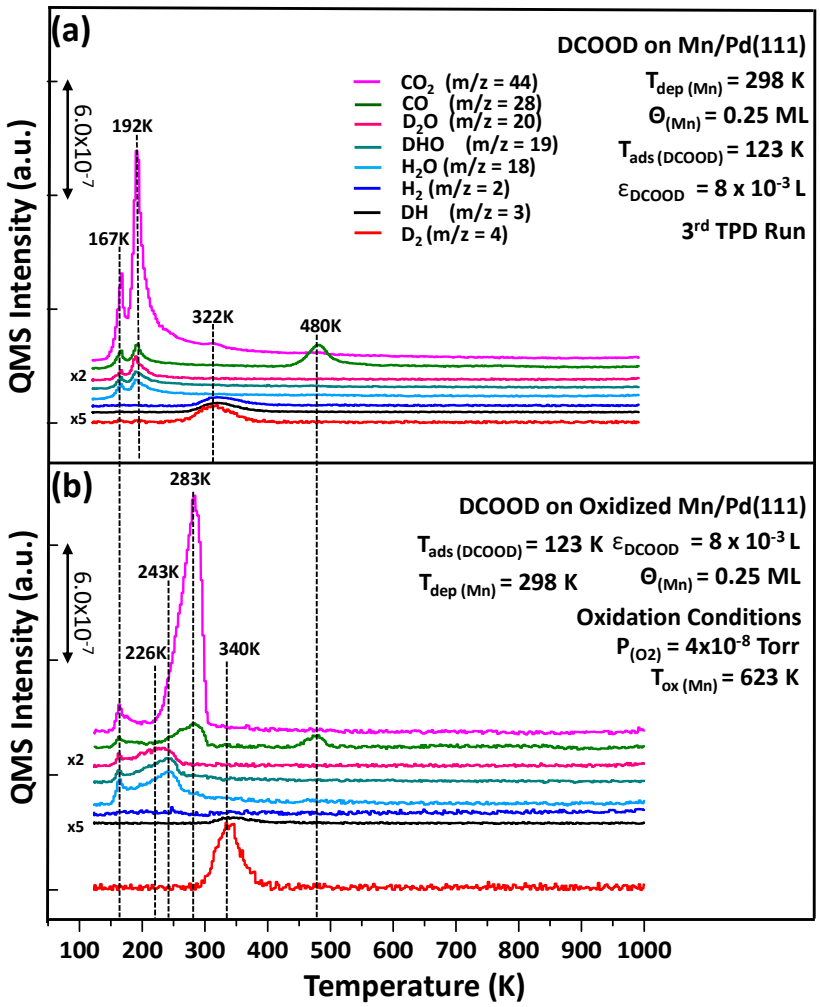

Figure 4.11. TPD profiles obtained upon a DCOOD exposure of 8 x 10^{-3} L at 123 K on (a) MnO_x (0.25 ML)/Pd(111) after three reaction runs, (b) pre-oxidized MnO_x(0.25 ML)/Pd(111). Some of the desorption signals are multiplied with the given factors for better visualization of the data.

Comparison of Figure 4.3 and Figures 4.11a-b reveals that oxidizing MnO_x increases TPD intensities of both dehydrogenation and dehydration products. Moreover, comparison of the CO_2 desorption signals of Pd(111) (Figure 4.3), MnO_x(0.25 ML)/Pd(111) (Figure 4.11a) and pre-oxidized MnO_x(0.25 ML)/Pd(111) (Figure 4.11b) reveal that, when the MnO_x overlayer is oxidized by FA (Figure 4.11a), a weak high-temperature CO_2 desorption shoulder is observed at 322 K, which is absent in clean Pd(111) (Figure 4.3). Similar high-temperature (283 K) CO_2 desorption features are observed in a much stronger manner in the case of pre-oxidized MnO_x overlayers on Pd(111) (Figure 4.11b). Former in-situ FTIR studies [59] reported the formation of carbonates on PdAg/MnO_x/SiO_2 mesoporous powder catalyst in catalytic FA decomposition. Therefore, these high temperature CO_2 desorption features observed in Figures 4.11a and 4.11b can be also partly attributed to the adsorbed carbonates generated upon CO/CO_2 capture/storage on the MnO_x domains.

The comparison between Figure 4.3 and Figure 4.11a-b also reveals that different MnO_x/Pd(111) systems yield significantly different changes in the surface chemistry. In Figure 4.11a, where MnO_x is oxidized upon its successive reactions with FA, it can be seen that the only change with respect to DCOOD/Pd(111) is the increase that is observed for both dehydration and dehydrogenation product desorption intensities, where nearly identical desorption temperatures observed for DCOOD-MnO_x (0.25 ML)/Pd(111) and DCOOD/Pd(111) reactions suggests the positive influence MnO_x is mainly non-catalytic. On the other hand, pre-oxidizing MnO_x with O_2 causes a separation between the desorption temperatures of water and CO_2 species suggesting that dehydrogenation and dehydration do not occur simultaneously. Moreover, a nearly 100 K increase in the CO_2 desorption maxima indicates a significant increase in the formate stability, where both experimental[8, 25, 32] and theoretical[55] studies correlate formate stability with the enhanced selectivity towards dehydrogenation. However, significant increase in the formation of water species along with

the positive temperature shift observed for these species suggests that pre-oxidizing MnO_x causes formation of new reaction paths (most likely condensation reactions of catemeric FA species), which significantly contributes to the water formation as well. Based on these observations it can be argued that *i)* there exists a particular oxidic MnO_x composition in which manganese oxide influences the D_2 formation mainly by promoting the FA adsorption/spillover without catalytically contributing the FA dehydrogenation reaction that is occurring on Pd active sites (Figure 11a) *ii)* there exists a particular oxidic MnO_x composition (which is more oxidic compared to MnO_x that can mainly act as a promoter) where manganese oxide catalytically contributes to the dehydrogenation reaction that is occurring on Pd active sites (Figure 11b). As a result, it can be argued that increasing oxidic character of MnO_x enhances D_2 formation by increasing the overall FA conversion ability of Pd(111) surface by different means (*i.e.* promoting effect and catalytic effect) depending on the oxidation state composition, but not specifically increasing the selectivity of Pd(111) towards FA dehydrogenation.

4.5 Effects of MnO_x Coverage on D_2 formation

Figure 4.12 illustrates how Mn (and directly related MnO_x) coverage affects the distribution of dehydrogenation and dehydration products (see Figure 4.13 for all integrated TPD profiles and Table 4.1 for integration temperature intervals of TPD profiles). One can see that both products follow a similar trend, having a maximum at MnO_x coverages of around 0.25 ML. Observation of a somewhat different trend for hydrogen is not clear currently but it is probably due to the effects of background H_2. Observation of catalytically the most active MnO_x/Pd(111) surface at a *sub-monolayer* MnO_x coverage, correlates with our earlier argument about the importance of co-presence of both MnO_x and Pd surface sites, while a specific coverage of 0.25 ML likely corresponds to a proper balance between MnO_x and exposed Pd(111) surface areas. It should be also noted that the positive influence of MnO_x pre-oxidation on D_2 formation is less sensitive to the MnO_x coverage (see Figures 4.9 and 4.14).

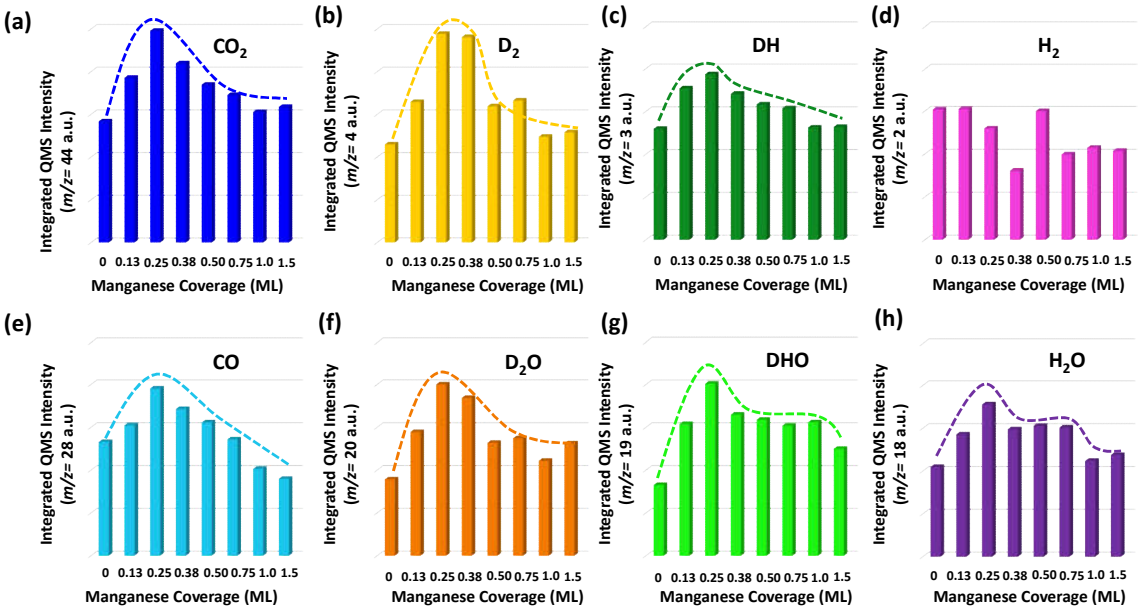

Figure 4.12 Integrated TPD intensities of various QMS channels as a function of manganese coverage.

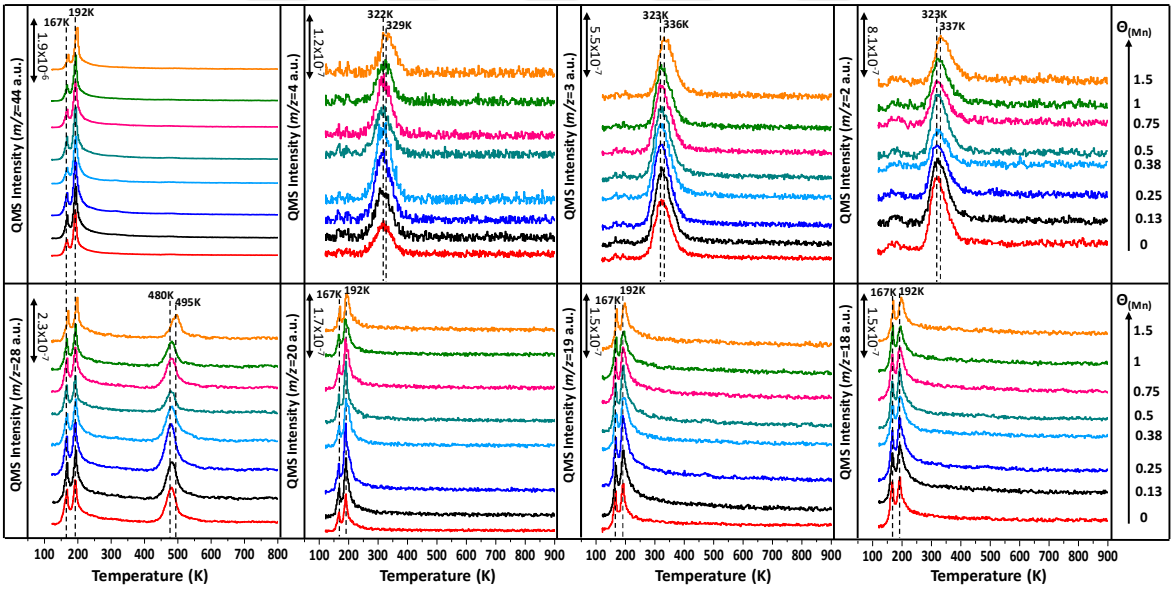

Figure 4.13. TPD profiles that are given in their integrated form in Figure 4.12.

		Integration Temperature Intervals of TPD Profiles							
		m/z =44 (CO_2)	*m/z* =28 (CO)	*m/z* =2 (H_2)	*m/z* =3 (DH)	*m/z* =4 (D_2)	*m/z* =18 (H_2O)	*m/z* =19 (DHO)	*m/z* =20 (D_2O)
$\Theta_{(Mn)}$	0	179K-249K	428K-583K	268K-419K	251K-425K	228K-422K	178K-226K	178K-223K	174K-240K
	0.13	178K-240K	420K-578K	263K-438K	233K-498K	224K-417K	181K-229K	177K-249K	175K-222K
	0.25	178K-256K/ 270K-335K	424K-578K	267K-455K	229K-463K	226K-415K	178K-241K	178K-263K	174K-238K
	0.38	177K-247K/ 290K-334K	424K-623K	262K-420K	251K-436K	244K-391K	179K-257K	177K-243K	174K-234K
	0.5	178-244K	430-602K	253K-445K	256K-428K	240K-403K	179K-235K	178K-238K	174K-229K
	0.75	180K-240K	429K-618K	265K-424K	253K-439K	254K-386K	180K-236K	177K-236K	176K-233K
	1	177K-243K	413K-575K	277K-427K	268K-446K	259K-395K	178K-234K	179K-234K	173K-240K
	1.5	179K-260K	440K-583K	278K-430K	275K-455K	262K-399K	180K-235K	182K-257K	177K-242K

Table 4.1 Integration Temperature Intervals of TPD Profiles that are given Figure 4.12**.**

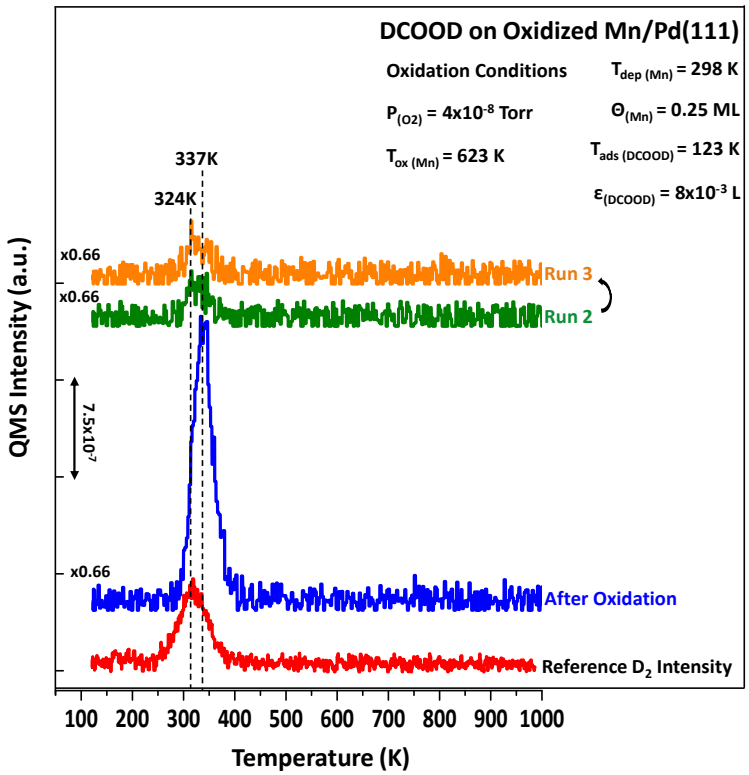

Figure 4.14. Change of *m/z* = 4 (D_2) channel as a function reaction runs on pre-oxidized MnO_x /Pd(111).

CHAPTER 5

Conclusion

In the current work, effects of Brønsted and Lewis bases on formic acid dehydrogenation selectivity of Pd(111) single crystal model catalyst were investigated under UHV conditions by using TPD/TPRS, LEED, and XPS techniques. Current results indicate that both NH_3 (a Brønsted Base) and MnO_x (a reducible metal oxide which contains Lewis basic sites) are capable of enhancing the hydrogen generation ability of Pd(111). It was found out that while NH_3 is capable of selectively enhancing hydrogen generation from formic acid by boosting FA dehydrogenation on the Pd(111) surface, presence of MnO_x -Pd(111) interfaces increase the hydrogen production from FA non-selectively by increasing the total FA conversion towards both dehydrogenation and dehydration.

Our results indicate that functionalizing the Pd(111) surface with ammonia suppressed the FA dehydration pathway, while enhancing the dehydrogenation pathway. Enhanced FA dehydrogenation activity and selectivity of the ammonia functionalized Pd(111) surface was attributed to the facilitation of the FA deprotonation and stabilization of the decomposition intermediate, *i.e.* formate, *via* formation of an ammonium counter ion on the surface. Furthermore, current findings also suggest that presence of a H-bonded ammonia network on the Pd(111) surface increases the hydrogen atom mobility and decreases the activation energy for molecular hydrogen desorption. In addition, it was found out that in the presence of NH_3, catalytic FA decomposition on Pd(111) also leads to amidation reactions resulting in the formation surface species such as formamide (NH_2CHO), which hinder CO liberation and prevent poisoning of the Pd(111) active sites by the strongly-bound CO species. It was also observed that enhancement of the FA dehydrogenation on Pd(111) with NH_3 is weakened at

extremely high coverages of ammonia (*e.g.* 1.4 MLE) due to the poisoning of the Pd(111) active sites with NH_3.

Both metallic (Mn^0) and oxidic (Mn^{2+} and Mn^{3+}) states of manganese in the MnO_x overlayer on Pd(111) were identified with X-ray photoelectron spectroscopy analysis. MnO_x/Pd(111) model catalyst enhanced D_2 formation by increasing the overall FA conversion, without specifically enhancing FA dehydrogenation selectivity. Maximum FA conversion was observed at a sub-monolayer MnO_x surface coverage of 0.25 ML (ML, monolayer) on Pd(111) which corresponds to a proper balance between exposed MnO_x and Pd active sites. It was suggested that particular oxidation state compositions of MnO_x domains mainly act as promoters for FA adsorption and spillover. On the other hand, it was also observed that increasing the oxidic character of MnO_x further also caused a catalytical improvement in the overall FA conversion.

Results presented in the current work indicates that both NH_3 and MnO_x increase the hydrogen formation from FA roughly by 15-20%. It should be emphasized that this improvement is quite important since increasing the catalytic efficiency of reactions even by 1-2% can save up to millions of dollars for chemical companies that are doing industrial scale production. Therefore, we believe that the work represented in this dissertation reveal valuable molecular-level insight regarding the fundamental understanding of the effectiveness of Brønsted and Lewis bases in the dehydrogenation processes of FA which can also be extended to the industrial applications.

Bibliography

1. Yoon, J., Y. Sun, and J.A. Rogers, *Flexible Solar Cells Made of Nanowires/Microwires*, in *Semiconductor Nanomaterials for Flexible Technologies*. 2010, Elsevier. p. 159-196.
2. Kordesch, K.V. and G.R. Simader, *Environmental impact of fuel cell technology.* Chemical Reviews, 1995. **95**(1): p. 191-207.
3. Mason, J.E., *World energy analysis: H2 now or later?* Energy Policy, 2007. **35**(2): p. 1315-1329.
4. Whitesides, G.M. and G.W. Crabtree, *Don't forget long-term fundamental research in energy.* science, 2007. **315**(5813): p. 796-798.
5. Lewis, N.S. and D.G. Nocera, *Powering the planet: Chemical challenges in solar energy utilization.* Proceedings of the National Academy of Sciences, 2006. **103**(43): p. 15729-15735.
6. Edwards, P.P., et al., *Hydrogen and fuel cells: towards a sustainable energy future.* Energy policy, 2008. **36**(12): p. 4356-4362.
7. Sharaf, O.Z. and M.F. Orhan, *An overview of fuel cell technology: Fundamentals and applications.* Renewable and Sustainable Energy Reviews, 2014. **32**: p. 810-853.
8. Karakurt, B., Y. Kocak, and E. Ozensoy, *Enhancement of Formic Acid Dehydrogenation Selectivity of Pd (111) Single Crystal Model Catalyst Surface via Brønsted Bases.* The Journal of Physical Chemistry C, 2019. **123**(47): p. 28777-28788.
9. Abe, J., E. Ajenifuja, and O. Popoola, *Hydrogen energy, economy and storage: review and recommendation.* International Journal of Hydrogen Energy, 2019.
10. Allsopp, M.W. and G. Vianello, *Poly (vinyl chloride).* Ullmann's Encyclopedia of Industrial Chemistry, 2000.
11. Eppinger, J.r. and K.-W. Huang, *Formic acid as a hydrogen energy carrier.* ACS Energy Letters, 2017. **2**(1): p. 188-195.
12. Moret, S., P.J. Dyson, and G. Laurenczy, *Direct synthesis of formic acid from carbon dioxide by hydrogenation in acidic media.* Nature communications, 2014. **5**: p. 4017.
13. Ikemiya, N., et al., *Long-term continuous conversion of CO2 to formic acid using boron-doped diamond electrodes.* ACS Sustainable Chemistry & Engineering, 2018. **6**(7): p. 8108-8112.
14. Valentini, F., et al., *Formic acid, a biomass-derived source of energy and hydrogen for biomass upgrading.* Energy & Environmental Science, 2019. **12**(9): p. 2646-2664.

15. Ozensoy, E. and D.W. Goodman, *Vibrational spectroscopic studies on CO adsorption, NO adsorption CO+ NO reaction on Pd model catalysts.* Physical Chemistry Chemical Physics, 2004. **6**(14): p. 3765-3778.
16. Ozensoy, E., D.C. Meier, and D.W. Goodman, *Polarization modulation infrared reflection absorption spectroscopy at elevated pressures: CO adsorption on Pd (111) at atmospheric pressures.* The Journal of Physical Chemistry B, 2002. **106**(36): p. 9367-9371.
17. Ozensoy, E., et al., *CO dissociation at elevated pressures on supported Pd nanoclusters.* The Journal of Physical Chemistry B, 2004. **108**(14): p. 4351-4357.
18. Ozensoy, E. and E.I. Vovk, *In-situ vibrational spectroscopic studies on model catalyst surfaces at elevated pressures.* Topics in Catalysis, 2013. **56**(15-17): p. 1569-1592.
19. Nielsen, M., et al., *Efficient hydrogen production from alcohols under mild reaction conditions.* Angewandte Chemie International Edition, 2011. **50**(41): p. 9593-9597.
20. Boddien, A., et al., *Efficient dehydrogenation of formic acid using an iron catalyst.* Science, 2011. **333**(6050): p. 1733-1736.
21. Puddephatt, R. and G.A. Yap, *An efficient binuclear catalyst for decomposition of formic acid.* Chemical Communications, 1998(21): p. 2365-2366.
22. Johnson, T.C., D.J. Morris, and M. Wills, *Hydrogen generation from formic acid and alcohols using homogeneous catalysts.* Chemical Society Reviews, 2010. **39**(1): p. 81-88.
23. Metin, Ö., X. Sun, and S. Sun, *Monodisperse gold–palladium alloy nanoparticles and their composition-controlled catalysis in formic acid dehydrogenation under mild conditions.* Nanoscale, 2013. **5**(3): p. 910-912.
24. Wang, Z.-L., et al., *Au@ Pd core–shell nanoclusters growing on nitrogen-doped mildly reduced graphene oxide with enhanced catalytic performance for hydrogen generation from formic acid.* Journal of Materials Chemistry A, 2013. **1**(41): p. 12721-12725.
25. Davis, J. and M. Barteau, *Reactions of carboxylic acids on the Pd (111)-(2× 2) O surface: multiple roles of surface oxygen atoms.* Surface science, 1991. **256**(1-2): p. 50-66.
26. Kovács, I., J. Kiss, and F. Solymosi, *On the role of adsorbed formate in the oxidation of C1 species on clean and modified Pd (100) surfaces.* Vacuum, 2017. **138**: p. 152-156.
27. Solymosi, F. and I. Kovács, *Adsorption and reaction of HCOOH on K-promoted Pd (100) surfaces.* Surface science, 1991. **259**(1-2): p. 95-108.

28. Egawa, C., et al., *Adsorption of methanol, formaldehyde and formic acid on Pd (100) surfaces modified by a sodium and sodium oxide overlayer.* Surface science, 1986. **176**(3): p. 491-504.
29. Jorgensen, S.W. and R.J. Madix, *Active oxygen on Group VIII metals: activation of formic acid and formaldehyde on Pd (100).* Journal of the American Chemical Society, 1988. **110**(2): p. 397-400.
30. Solymosi, F., J. Kiss, and I. Kovacs, *Adsorption and decomposition of formic acid on potassium-promoted rhodium (111) surfaces.* The Journal of Physical Chemistry, 1988. **92**(3): p. 796-803.
31. Solymosi, F., J. Kiss, and I. Kovács, *Adsorption of HCOOH on Rh (111) and its reaction with preadsorbed oxygen.* Surface science, 1987. **192**(1): p. 47-65.
32. Houtman, C. and M.A. Barteau, *Reactions of formic acid and formaldehyde on Rh (111) and Rh (111)-(2× 2) O surfaces.* Surface science, 1991. **248**(1-2): p. 57-76.
33. Avery, N., et al., *Decomposition of formic acid on Ru (001): An EELS search for a formic anhydride intermediate.* Surface Science, 1982. **122**(1): p. L574-L578.
34. Sun, Y.K. and W. Weinberg, *Catalytic decomposition of formic acid on Ru (001): Transient measurements.* The Journal of chemical physics, 1991. **94**(6): p. 4587-4599.
35. Avery, N.R., *Adsorption of formic acid on clean and oxygen covered Pt (111).* Applications of Surface Science, 1982. **11**: p. 774-783.
36. Silbaugh, T.L., E.M. Karp, and C.T. Campbell, *Energetics of formic acid conversion to adsorbed formates on Pt (111) by transient calorimetry.* Journal of the American Chemical Society, 2014. **136**(10): p. 3964-3971.
37. Columbia, M. and P. Thiel, *The reaction of formic acid with clean and water-covered Pt (111).* Surface Science, 1990. **235**(1): p. 53-59.
38. Ying, D.H. and J.M. Robert, *Thermal desorption study of formic acid decomposition on a clean cu (110) surface.* Journal of catalysis, 1980. **61**(1): p. 48-56.
39. Yao, Y. and F. Zaera, *Adsorption and thermal chemistry of formic acid on clean and oxygen-predosed Cu (110) single-crystal surfaces revisited.* Surface Science, 2016. **646**: p. 37-44.
40. Bowker, M., et al., *The adsorption and decomposition of formic acid on Cu {110}.* Surface science, 1996. **349**(2): p. 97-110.
41. Sims, J.J., et al., *Adsorption and decomposition of formic acid on cobalt (0001).* The Journal of Physical Chemistry C, 2018. **122**(35): p. 20279-20288.

42. Barteau, M., M. Bowker, and R. Madix, *Acid-base reactions on solid surfaces: the reactions of HCOOH, H2CO, and HCOOCH3 with oxygen on Ag (110).* Surface Science, 1980. **94**(2-3): p. 303-322.
43. Sim, W., P. Gardner, and D. King, *Multiple bonding configurations of adsorbed formate on Ag {111}.* The Journal of Physical Chemistry, 1996. **100**(30): p. 12509-12516.
44. Karatok, M., et al., *Tuning reactivity layer-by-layer: formic acid activation on Ag/Pd (111).* Chemical Science, 2020.
45. Yu, W.-Y., et al., *Selective hydrogen production from formic acid decomposition on Pd–Au bimetallic surfaces.* Journal of the American Chemical Society, 2014. **136**(31): p. 11070-11078.
46. Jin, M., et al., *Palladium nanocrystals enclosed by {100} and {111} facets in controlled proportions and their catalytic activities for formic acid oxidation.* Energy & Environmental Science, 2012. **5**(4): p. 6352-6357.
47. Yurderi, M., et al., *Carbon supported trimetallic PdNiAg nanoparticles as highly active, selective and reusable catalyst in the formic acid decomposition.* Applied Catalysis B: Environmental, 2014. **160**: p. 514-524.
48. Huang, Y., et al., *An effective low Pd-loading catalyst for hydrogen generation from formic acid.* International Journal of Hydrogen Energy, 2017. **42**(29): p. 18375-18382.
49. Zhou, X., et al., *High-quality hydrogen from the catalyzed decomposition of formic acid by Pd–Au/C and Pd–Ag/C.* Chemical Communications, 2008(30): p. 3540-3542.
50. Li, S.-j., et al., *Facile synthesis of AgAuPd/graphene with high performance for hydrogen generation from formic acid.* Journal of Materials Chemistry A, 2015. **3**(28): p. 14535-14538.
51. Ke, F., L. Wang, and J. Zhu, *An efficient room temperature core–shell AgPd@ MOF catalyst for hydrogen production from formic acid.* Nanoscale, 2015. **7**(18): p. 8321-8325.
52. Tedsree, K., et al., *Hydrogen production from formic acid decomposition at room temperature using a Ag–Pd core–shell nanocatalyst.* Nature nanotechnology, 2011. **6**(5): p. 302.
53. Choi, B.-S., et al., *Core–shell engineering of Pd–Ag bimetallic catalysts for efficient hydrogen production from formic acid decomposition.* ACS Catalysis, 2018. **9**(2): p. 819-826.

54. Wang, Y., et al., *New insight into the decomposition mechanism of formic acid on Pd (111): competing formation of CO2 and CO.* The Journal of Physical Chemistry C, 2014. **118**(4): p. 2067-2076.

55. Scaranto, J. and M. Mavrikakis, *Density functional theory studies of HCOOH decomposition on Pd (111).* Surface Science, 2016. **650**: p. 111-120.

56. Zheng, T., et al., *The structure of formate species on Pd (1 1 1) calculated by density functional theory and determined using low energy electron diffraction.* Surface science, 2005. **574**(2-3): p. 166-174.

57. Saxena, P. and N. Thirupathi, *Reactions of Cd (OAc) 2· 2H2O with variously substituted pyridines. Efforts to unravel the factors that determine structure/nuclearity of the products.* Polyhedron, 2015. **98**: p. 238-250.

58. Perşembe, E., *Trimetalic heterogeneous catalyst for dehydrogenation of formic acid with enhanced CO tolerance*. 2017, Bilkent University.

59. Bulut, A., et al., *Pd-MnOx nanoparticles dispersed on amine-grafted silica: highly efficient nanocatalyst for hydrogen production from additive-free dehydrogenation of formic acid under mild conditions.* Applied Catalysis B: Environmental, 2015. **164**: p. 324-333.

60. Bi, Q.Y., et al., *Dehydrogenation of Formic Acid at Room Temperature: Boosting Palladium Nanoparticle Efficiency by Coupling with Pyridinic-Nitrogen-Doped Carbon.* Angewandte Chemie International Edition, 2016. **55**(39): p. 11849-11853.

61. Silverman, R.B. and M.W. Holladay, *The organic chemistry of drug design and drug action*. 2014: Academic press.

62. Karatas, Y., et al., *PdAu-MnOx nanoparticles supported on amine-functionalized SiO2 for the room temperature dehydrogenation of formic acid in the absence of additives.* Applied Catalysis B: Environmental, 2016. **180**: p. 586-595.

63. Mori, K., M. Dojo, and H. Yamashita, *Pd and Pd–Ag nanoparticles within a macroreticular basic resin: an efficient catalyst for hydrogen production from formic acid decomposition.* Acs Catalysis, 2013. **3**(6): p. 1114-1119.

64. Yadav, M., et al., *Strong metal–molecular support interaction (SMMSI): amine-functionalized gold nanoparticles encapsulated in silica nanospheres highly active for catalytic decomposition of formic acid.* Journal of Materials Chemistry, 2012. **22**(25): p. 12582-12586.

65. Wang, Y., D. Widmann, and R.J. Behm, *Influence of TiO2 bulk defects on CO adsorption and CO oxidation on Au/TiO2: electronic metal–support interactions (EMSIs) in supported Au catalysts.* ACS Catalysis, 2017. **7**(4): p. 2339-2345.

66. Wang, Y., et al., *The role of electronic metal-support interactions and its temperature dependence: CO adsorption and CO oxidation on Au/TiO2 catalysts in the presence of TiO2 bulk defects.* Journal of catalysis, 2017. **354**: p. 46-60.

67. Bulutoglu, P.S., et al., *Dry reforming of glycerol over Rh-based ceria and zirconia catalysts: New insights on catalyst activity and stability.* Applied Catalysis A: General, 2018. **564**: p. 157-171.

68. Karatok, M., *Nature of oxygen species on Au (111) and Ag (111) model catalysts and their role in OH, CH, CC, NH bond activation*. 2017, Bilkent University.

69. Niemantsverdriet, J.W., *Spectroscopy in catalysis: an introduction*. 2007: John Wiley & Sons.

70. Aerts, D., et al., *Probing the Meaning of Quantum Mechanics: Information, Contextuality, Relationalism and EntanglementProceedings of the II International Workshop on Quantum Mechanics and Quantum Information. Physical, Philosophical and Logical Approaches*. 2018: World Scientific Publishing.

71. Chorkendorff, I. and J.W. Niemantsverdriet, *Concepts of modern catalysis and kinetics*. 2017: John Wiley & Sons.

72. Meng, L., et al., *Buckled silicene formation on Ir (111).* Nano letters, 2013. **13**(2): p. 685-690.

73. Chusuei, C.C. and D.W. Goodman, *X-ray photoelectron spectroscopy.* Encyclopedia of physical science and technology, 2002. **17**: p. 921-938.

74. Riber, *"X-Ray source model CX 700 and its power supply unit model ACX 700", Insturction Manual. vol. No: 608 362 02 P.*

75. Riber, *"MAC 2 - analysis module and EA - 150 analyzer", Instructions Manual, Vol No: 608 361 82 T.*

76. Sise, O. and T.J. Zouros, *Position, energy, and transit time distributions in a hemispherical deflector analyzer with position sensitive detector.* Journal of Spectroscopy, 2015. **2015**.

77. King, D.A., *Thermal desorption from metal surfaces: A review.* Surface Science, 1975. **47**(1): p. 384-402.

78. Schroeder, S.L. and M. Gottfried, *Temperature-programmed desorption (TPD) thermal desorption spectroscopy (TDS).* Advanced Physical Chemistry Laboratory, FU Berlin, 2002. **18**.
79. Redhead, P., *Thermal desorption of gases.* Vacuum, 1962. **12**(4): p. 203-211.
80. Habenschaden, E. and J. Küppers, *Evaluation of flash desorption spectra.* Surface Science, 1984. **138**(1): p. L147-L150.
81. Moulder, J.F., *Handbook of X-ray photoelectron spectroscopy.* Physical electronics, 1995: p. 230-232.
82. Wasa, K., I. Kanno, and H. Kotera, *Handbook of sputter deposition technology: fundamentals and applications for functional thin films, nano-materials and MEMS*. 2012: William Andrew.
83. Van Hardeveld, R., R. Van Santen, and J. Niemantsverdriet, *The adsorption of NH3 on Rh (111).* Surface science, 1996. **369**(1-3): p. 23-35.
84. Kay, B.D., et al., *The influence of adsorbate–absorbate hydrogen bonding in molecular chemisorption: NH3, HF, and H2O on Au (111).* The Journal of chemical physics, 1989. **91**(8): p. 5120-5121.
85. Fisher, G.B., *The electronic structure of two forms of molecular ammonia adsorbed on Pt (111).* Chemical Physics Letters, 1981. **79**(3): p. 452-458.
86. Karatok, M., et al., *Selective catalytic ammonia oxidation to nitrogen by atomic oxygen species on Ag (111).* The Journal of Physical Chemistry C, 2017. **121**(41): p. 22985-22994.
87. Netzer, F.P. and T.E. Madey, *Interaction of NH3 with oxygen-predosed Ni (111).* Surface Science, 1982. **119**(2-3): p. 422-432.
88. Rodriguez, J., et al., *A FT-IRAS study of ammonia adsorbed on Ru (0001).* Surface science, 1992. **271**(3): p. 333-339.
89. Sälli, E., S. Martiskainen, and L. Halonen, *Computational study of the vibrational structure of the ammonia molecule adsorbed on the fcc (111) transition metal surfaces.* The Journal of Physical Chemistry C, 2012. **116**(28): p. 14960-14969.
90. Bulushev, D.A. and J.R. Ross, *Vapour phase hydrogenation of olefins by formic acid over a Pd/C catalyst.* Catalysis Today, 2011. **163**(1): p. 42-46.
91. McBride, F., et al., *Strain relief and disorder in commensurate water layers formed on Pd (111).* Journal of Physics: Condensed Matter, 2012. **24**(12): p. 124102.
92. Herron, J.A., et al., *Trends in formic acid decomposition on model transition metal surfaces: A density functional theory study.* Acs Catalysis, 2014. **4**(12): p. 4434-4445.

93. Nilekar, A.U., J. Greeley, and M. Mavrikakis, *A Simple Rule of Thumb for Diffusion on Transition-Metal Surfaces.* Angewandte Chemie International Edition, 2006. **45**(42): p. 7046-7049.

94. Sridhar, M., J.A. Van Bokhoven, and O. Kröcher, *Effect of ammonia on the decomposition of ammonium formate over Au/TiO2 under oxidizing conditions relevant to SCR: Enhancement of formic acid decomposition rate and CO2 production.* Applied Catalysis A: General, 2014. **486**: p. 219-229.

95. Liu, G., et al., *Interactions of ultrathin Pb films with Ru (0001) and Pd (111).* Physical Review B, 2003. **68**(3): p. 035406.

96. Lagally, M.G., *Kinetics of ordering and growth at surfaces*. Vol. 239. 2012: Springer Science & Business Media.

97. Thompson, A.C. and D. Vaughan, *X-ray data booklet*. Vol. 8. 2001: Lawrence Berkeley National Laboratory, University of California Berkeley, CA.

98. Mandale, A. and S. Badrinarayanan, *X-ray photoelectron spectroscopic studies of the semimagnetic semiconductor system Pb1− xMnxTe.* Journal of electron spectroscopy and related phenomena, 1990. **53**(1-2): p. 87-95.

99. Hsin-Kuei, H. and J.W. Rabalais, *Chemisorption and the initial stage of oxidation on Mn.* Surface Science, 1981. **107**(2-3): p. 376-390.

100. Jenks, C.J., et al., *Photoelectron spectra of an Al 70 Pd 21 Mn 9 quasicrystal and the cubic alloy Al 60 Pd 25 Mn 15.* Physical Review B, 1996. **54**(9): p. 6301.

101. Sandell, A. and A.J. Jaworowski, *The Mn 2p core-level photoelectron spectrum of Pd–Mn bimetallic systems on Pd (1 0 0).* Journal of electron spectroscopy and related phenomena, 2004. **135**(1): p. 7-14.

102. Rader, O., et al., *Structure and electron correlation of Mn on Ni (110).* Physical Review B, 2001. **64**(16): p. 165414.

103. Rader, O., et al., *Correlation satellite driven by reduced dimensionality.* EPL (Europhysics Letters), 1997. **39**(4): p. 429.

104. Schieffer, P., et al., *Strong correlation satellites in core level photoemission from Mn in the monolayer range on Ag (001).* Journal of electron spectroscopy and related phenomena, 1999. **104**(1-3): p. 127-134.

105. Li, F., et al., *Two-dimensional manganese oxide nanolayers on Pd (100): the surface phase diagram.* Journal of Physics: Condensed Matter, 2009. **21**(13): p. 134008.

106. Strohmeier, B.R. and D.M. Hercules, *Surface spectroscopic characterization of manganese/aluminum oxide catalysts.* The Journal of Physical Chemistry, 1984. **88**(21): p. 4922-4929.

107. Aoki, A., *X-ray photoelectron spectroscopic studies on ZnS: MnF2 phosphors.* Japanese Journal of Applied Physics, 1976. **15**(2): p. 305.

108. Biesinger, M.C., et al., *Resolving surface chemical states in XPS analysis of first row transition metals, oxides and hydroxides: Cr, Mn, Fe, Co and Ni.* Applied Surface Science, 2011. **257**(7): p. 2717-2730.

109. Oku, M., K. Hirokawa, and S. Ikeda, *X-ray photoelectron spectroscopy of manganese—oxygen systems.* Journal of Electron Spectroscopy and Related Phenomena, 1975. **7**(5): p. 465-473.

110. Di Castro, V. and G. Polzonetti, *XPS study of MnO oxidation.* Journal of Electron Spectroscopy and Related Phenomena, 1989. **48**(1): p. 117-123.

111. Foord, J., R. Jackman, and G. Allen, *An X-ray photoelectron spectroscopic investigation of the oxidation of manganese.* Philosophical Magazine A, 1984. **49**(5): p. 657-663.

112. Lundgren, E., et al., *Two-dimensional oxide on Pd (111).* Physical Review Letters, 2002. **88**(24): p. 246103.

113. Klikovits, J., et al., *Surface oxides on Pd (111): STM and density functional calculations.* Physical Review B, 2007. **76**(4): p. 045405.

114. Kim, S.H., et al., *Enhanced reactivity of adsorbed oxygen on Pd (111) induced by compression of the oxygen layer.* Physical Review B, 2005. **72**(15): p. 155414.

115. Zeng, F., et al., *Facile construction of Mn3O4-MnO2 hetero-nanorods/graphene nanocomposite for highly sensitive electrochemical detection of hydrogen peroxide.* Electrochimica Acta, 2016. **196**: p. 587-596.

116. Raj, A.M.E., et al., *XRD and XPS characterization of mixed valence Mn3O4 hausmannite thin films prepared by chemical spray pyrolysis technique.* Applied Surface Science, 2010. **256**(9): p. 2920-2926.

Appendix A

Alternative Interpretation of Mn $2p_{3/2}$ XPS spectra given in Figures 4.5 and 4.9

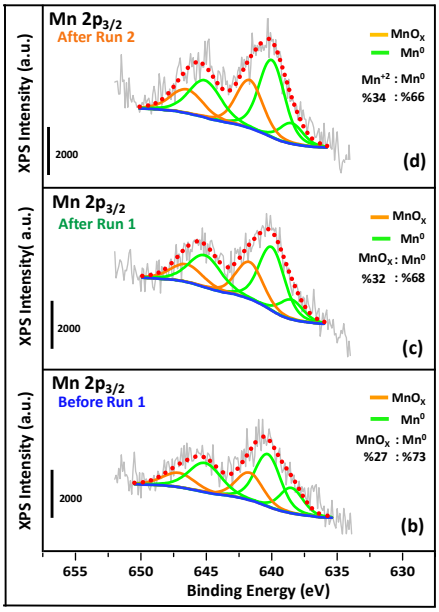

E.1. Alternative interpretation of Mn $2p_{3/2}$ spectra given in Figure 4.5.

Figure E.1 represents the alternative interpretation of Mn $2p_{3/2}$ XPS spectra given in Figure 4.5. In the case of ultra-thin (~1 ML) Mn films grown on d-metal surfaces (including Pd [101]) Mn $2p_{3/2}$ main peak centers around 640 eV and exhibits an intense satellite peak that is separated by ~5 eV [102-104]. Therefore, the peak located at 640.3 eV, along with the intense satellite feature at 645.3 eV, is attributed to Mn^0. Moreover, earlier studies have also showed that main Mn $2p_{3/2}$ XPS peak of ultra-thin Mn films grown on Pd(100)[101] and Ni(110)[102] exhibits an additional 'shoulder' feature located below 640 eV (where this 'shoulder' feature is much more intense in the XPS spectrum given in Figure 4.8 which is obtained from annealed MnO_x). Consequently, the lowest binding energy peak detected at 638.5 eV is also associated

with Mn^0. In the literature, Mn $2p_{3/2}$ peaks located *ca.* 642 eV are mainly associated with Mn +3 and +4 oxidation states [109-111]. Moreover, it is well-known that Mn^{+2} state has a distinct satellite feature around 647 eV. [106-108]. As a result of these findings, the presence of peak at 641.9, along with an additional satellite feature occurring *ca.* 647, strongly suggests the presence of a mix valence MnO_x that contains Mn^{+2} [115]. In general, MnO_x valence states are resolved by making use of the Mn*3s* region [116]. However, Mn *3s* region could not be detected because of the poor detection limit of the XPS analyzer. On the other hand, we believe that Mn^{+3} and Mn^{+2} species are present on the surface (see Figure 4.5) since we did not expect to have Mn^{+4} at RT, especially in the absence of oxygen. It should be noted that we did not expect to have Mn^{+4} in the case of pre-oxidized MnO_x as well (Figure E.2).

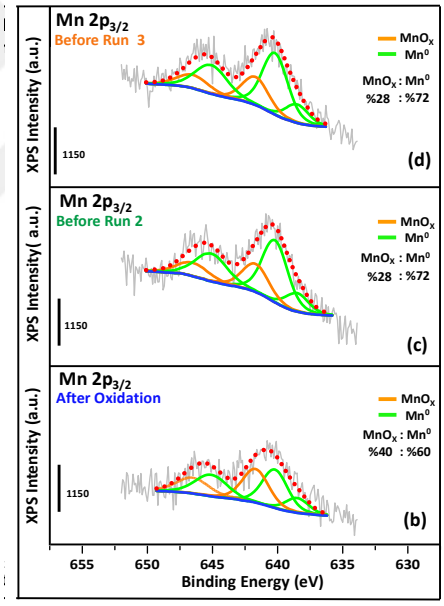

E.2. Alternative interpretation of Mn $2p_{3/2}$ spectra given in Figure 4.9.

This alternative interpretation does not affect and/or change findings that are discussed in chapter 5 since it also predicts that increasing the oxidic character of MnO_x increases the D_2 formation *via* increasing the overall FA conversion.

Appendix B

Difference (Δ) XPS spectra of Raw Mn $2p_{3/2}$ XPS spectra represented in Figures 4.5 and 4.9

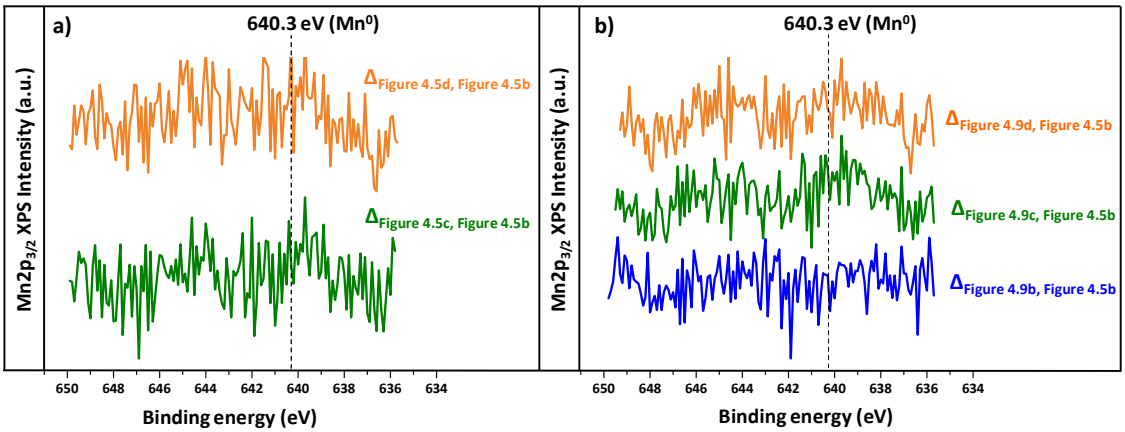

E.3. (a) Difference (Δ) XPS intensity spectra of raw Mn $2p_{3/2}$ XPS spectra represented in Figure 4.5. (b) Difference (Δ) XPS intensity spectra of raw Mn $2p_{3/2}$ XPS spectra represented in Figure 4.9.

Figure E.3 represents difference (Δ) XPS intensity spectra of raw Mn $2p_{3/2}$ XPS spectra represented in Figures 4.5 and 4.9, *i.e.* Mn $2p_{3/2}$ XPS spectra represented with gray color. It should be noted that all ΔXPS spectra are constructed by using raw XPS Mn $2p_{3/2}$ XPS data represented in Figure 4.5b as a reference and subtract this data from the raw Mn $2p_{3/2}$ XPS spectra given in Figures 4.5c-d (Figure E.3a) and Figures 4.9b-d (Figure E.3b) after properly scaling up all of the raw spectra. Despite the spectra given Figure E.3 reveal some differences, poor S/N significantly hinders achieving information about the change in oxidation as a function successive TPD runs.

Appendix C

List of Publications
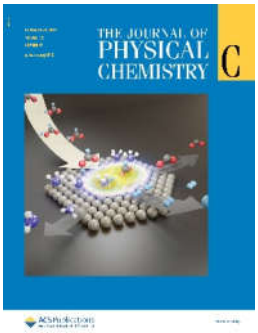
1. Bartu Karakurt[1].; Yusuf Koçak and Emrah Ozensoy. Enhancement of Formic Acid Dehydrogenation Selectivity of Pd(111) Single Crystal Model Catalyst Surface via Brønsted Bases (J. Phys. Chem. C, 2019, 123, 47, 28777-28788) Published as Supplementary Cover Article.